



# Investigation of the structure-property relationships of hierarchical Y zeolites for the co-processing of bio-oil with vacuum gas oil

Yann Chapelliere

## ► To cite this version:

Yann Chapelliere. Investigation of the structure-property relationships of hierarchical Y zeolites for the co-processing of bio-oil with vacuum gas oil. Catalysis. Université de Lyon, 2020. English. NNT : 2020LYSE1046 . tel-02887223

**HAL Id: tel-02887223**

**<https://theses.hal.science/tel-02887223>**

Submitted on 2 Jul 2020

**HAL** is a multi-disciplinary open access archive for the deposit and dissemination of scientific research documents, whether they are published or not. The documents may come from teaching and research institutions in France or abroad, or from public or private research centers.

L'archive ouverte pluridisciplinaire **HAL**, est destinée au dépôt et à la diffusion de documents scientifiques de niveau recherche, publiés ou non, émanant des établissements d'enseignement et de recherche français ou étrangers, des laboratoires publics ou privés.



N° d'ordre NNT : 2020LYSE1046

## **THESE de DOCTORAT DE L'UNIVERSITE DE LYON**

opérée au sein de  
**l'Université Claude Bernard Lyon 1**

**Ecole Doctorale N° 206**  
**Ecole Doctorale de Chimie de Lyon**

**Spécialité de doctorat** : Matériaux et Catalyse  
**Discipline** : Chimie

Soutenue publiquement le 09/03/2020, par :  
**Yann CHAPELLIÈRE**

---

# **Investigation of the structure-property relationships of hierarchical Y zeolites for the co-processing of bio-oil with vacuum gas oil**

---

Devant le jury composé de :

Giroir-Fendler, Anne	Professeure, Université de Lyon, IRCELYON	Présidente
Mintova, Svetlana	Directrice de Recherche CNRS, Université de Caen, LCS	Rapporteure
Pinard, Ludovic	Maître de Conférences, Université de Poitiers, IC2MP	Rapporteur
Martens, Luc	Responsable Industriel, ExxonMobil	Examineur
Schuurman, Yves	Directeur de Recherche CNRS, Université de Lyon, IRCELYON	Directeur de thèse
Farrusseng, David	Directeur de Recherche CNRS, Université de Lyon, IRCELYON	Co-directeur de thèse

## **Université Claude Bernard – LYON 1**

Président de l'Université	M. Frédéric FLEURY
Président du Conseil Académique	M. Hamda BEN HADID
Vice-Président du Conseil d'Administration	M. Didier REVEL
Vice-Président du Conseil des Etudes et de la Vie Universitaire	M. Philippe CHEVALLIER
Vice-Président de la Commission de Recherche	M. Jean-François MORNEX
Directeur Général des Services	M. Damien VERHAEGHE

### **COMPOSANTES SANTE**

Faculté de Médecine Lyon-Est – Claude Bernard	Doyen : M. Gilles RODE
Faculté de Médecine et Maïeutique Lyon Sud Charles. Mérieux	Doyenne : Mme Carole BURILLON
UFR d'Odontologie	Doyenne : Mme Dominique SEUX
Institut des Sciences Pharmaceutiques et Biologiques	Directrice : Mme Christine VINCIGUERRA
Institut des Sciences et Techniques de la Réadaptation	Directeur : M. Xavier PERROT
Département de Formation et Centre de Recherche en Biologie Humaine	Directrice : Mme Anne-Marie SCHOTT

### **COMPOSANTES & DEPARTEMENTS DE SCIENCES & TECHNOLOGIE**

UFR Biosciences	Directrice : Mme Kathrin GIESELER
Département Génie Electrique et des Procédés (GEP)	Directrice : Mme Rosaria FERRIGNO
Département Informatique	Directeur : M. Behzad SHARIAT
Département Mécanique	Directeur M. Marc BUFFAT
UFR - Faculté des Sciences	Administrateur provisoire : M. Bruno ANDRIOLETTI
UFR (STAPS)	Directeur : M. Yannick VANPOULLE
Observatoire de Lyon	Directrice : Mme Isabelle DANIEL
Ecole Polytechnique Universitaire Lyon 1	Directeur : Emmanuel PERRIN
Ecole Supérieure de Chimie, Physique, Electronique (CPE Lyon)	Directeur : Gérard PIGNAULT
Institut Universitaire de Technologie de Lyon 1	Directeur : M. Christophe VITON
Institut de Science Financière et d'Assurances	Directeur : M. Nicolas LEBOISNE
ESPE	Administrateur Provisoire : M. Pierre CHAREYRON

# Acknowledgements

---

Cette thèse a été une aventure de trois ans en demi, qui m'a permis de mobiliser des ressources insoupçonnées auparavant. Ce cheminement, qui m'aura alternativement procuré espoir, déception et satisfaction, parfois en l'espace de quelques jours, permet un apprentissage ô combien formateur ! Cette expérience a été rendue possible grâce à la contribution de nombreuses personnes. Je souhaiterais ici les en remercier.

Les travaux présentés dans ce manuscrit ont été menés à l'Institut de Recherche sur la Catalyse et l'Environnement de Lyon (IRCELYON). A ce titre, je tiens à remercier Catherine Pinel, directrice de l'IRCELYON, de m'avoir accueilli dans ce laboratoire.

Cette thèse a été dirigée par Yves Schuurman et David Farrusseng, tous deux directeurs de recherche à l'IRCELYON. Tout d'abord, merci de m'avoir choisi pour mener ces travaux de thèse sur le co-FCC et l'utilisation de zéolithes hiérarchisées. Également, je souhaiterais vous remercier pour le soutien que vous m'avez communiqué durant ces trois années. Le sujet n'était pas simple, mais vous avez su conjointement m'orienter et me guider lors de mes remises en question, me permettant d'aboutir au travail présenté ici. Merci beaucoup.

Je souhaiterais également remercier chaleureusement Alain Tuel et Claude Mirodatos, respectivement directeur de recherche et directeur de recherche émérite à l'IRCELYON. Merci Alain pour ton expertise et ton apport fondamental sur les zéolithes. Merci Claude d'avoir mis à disposition ton inexhaustible savoir et expérience au service de ce projet. Tu étais toujours disponible pour me proposer de nouvelles idées, ou échanger sur notre passion commune qu'est la course à pied. C'était à chaque fois rafraichissant et mobilisateur.

Je tiens également à exprimer ma gratitude à Pascale Mascunan, Françoise Bosselet, Yoann Aizac, Laurence Burel et Chantal Lorentz pour leurs assistances scientifiques et techniques liées à la caractérisation de mes matériaux et échantillons. Merci Cécile Daniel, Emmanuel Landrison et Mehdi Bessaa pour votre contribution au développement des nouveaux bancs de tests.

Ces trois années ont été effectuées au sein de l'équipe Ingénierie (ING). A ce titre, je souhaiterais remercier l'ensemble de ses membres, merveilleux collègues avec lesquels j'ai apprécié les partages scientifiques, ainsi que ceux plus personnels lors de nos déjeuners communs au quotidien.

Ce travail de thèse n'aurait pu aboutir sans le soutien infaillible de ma famille, ma femme et mes amis. Vous êtes les premiers à croire en moi, souvent bien plus que moi-même. Sans vous je n'en serais pas là. Enfin, Annika, je souhaiterais te remercier particulièrement d'avoir tenu à mes côtés



## Acknowledgements

---

durant ces trois années. Ton quotidien a été rythmé et chamboulé par cette thèse, mais tu es restée un merveilleux pilier.

## Abstract

Fluid Catalytic Cracking (FCC) gasoline represents one third of the global gasoline pool. In order to meet objectives regarding increased renewable share in transportation fuels, the production of a hybrid bio/fossil fuel by co-refining biomass pyrolysis liquids with crude oil fractions in an oil refinery is an achievable approach. Oxygenated molecules, typical of the bio-feedstock, are present in liquids produced from biomass pyrolysis. Because large lignocellulosic fragments could strongly adsorb on the FCC zeolite surface, they may not access catalytic sites or could diffuse very slowly in the microporous network. Hence, for high oxygenated molecule content, co-refining may lead to severe changes in product quality, such as a higher aromaticity, coke and residual oxygenates in the hybrid fuels that are produced. To adjust the reactivity of FCC catalysts towards bio-oil, four Y zeolites with well controlled hierarchical mesoporous – microporous network have been investigated. They mainly vary by the characteristics of the secondary mesoporous network (pore size, mesoporous volume) while their globally similar acidity displays some changes in nature (Lewis/Brønsted). The impact of hierarchical porous structures combined with changes in acidity is studied on catalytic activity and selectivity (e.g., coke formation). The issue of diffusion limitation in line with acidity changes are discussed based on Zero Length Column (ZLC) measurements, pyridine adsorption measurements, catalytic cracking of n-hexane and co-processing of vacuum gas oil and bio-oil in micro-activity test unit.

## Résumé

Le monde fait face à des enjeux climatiques et énergétiques qui impliquent l'utilisation de biomasse, au même titre que d'autres énergies renouvelables, comme des moyens de production d'énergie. Parmi les voies envisagées, l'addition d'huile de pyrolyse au sein de procédés de raffinage déjà existants présenterait l'avantage d'une mise en place rapide et d'une modification structurelle limitée. L'unité de craquage catalytique en lit fluidisé (FCC), valorisant les fractions pétrolières les plus lourdes, est l'unité la plus à même de valoriser des charges biosourcées. Cependant, les premiers tests ont pu révéler la présence de certains freins, tels que l'immiscibilité des charges fossiles et biosourcées, impliquant la mise en place de deux systèmes d'injection indépendants, ou encore une plus forte désactivation des catalyseurs de craquage. Sur ce dernier point, la présence de larges fragments lignocellulosiques, volumineux et riches en oxygène, perturbe le fonctionnement des catalyseurs de FCC. Leur encombrement étant suspecté de limiter leur accès aux sites acides, responsables du craquage catalytique, l'addition de mésopores aux cristaux de zéolites microporeux

## Abstract

---

est une voie de recherche intéressante. Parallèlement à cela, la préparation de matériaux à porosité hiérarchisée, c'est-à-dire alliant l'agencement de plusieurs niveaux de porosité, se développe depuis quelques années. Ces matériaux rentrent parfaitement dans le cadre de l'amélioration de l'accessibilité aux sites acides. Ces travaux de thèse visent ainsi à définir l'impact que peut avoir un processus de hiérarchisation de la porosité sur le craquage catalytique d'un mélange de charges pétrolières fossiles avec une huile de pyrolyse de biomasse. Dans cette optique, une zéolite Y - couramment utilisée pour le craquage catalytique - a été hiérarchisée conformément aux protocoles déjà disponibles dans la littérature. Les caractéristiques structurales de quatre matériaux ont ensuite été définies, aidant ainsi à la compréhension d'études du transfert diffusionnel, du craquage de molécules modèles et du craquage de charges réelles réalisées par la suite et présentées dans ce manuscrit de thèse.

# Content

---

ABSTRACT .....	3
RESUME .....	3
CHAPTER I: STATE OF THE ART .....	10
1. CONTEXT OF THIS WORK .....	10
2. FLUID CATALYTIC CRACKING (FCC).....	11
2.1 DESCRIPTION OF THE UNIT .....	12
2.2 LABORATORY PROCEDURE FOR FCC TESTING .....	13
2.3 FCC CATALYST .....	14
2.4 INDUSTRIAL FOSSIL FEEDSTOCKS .....	15
2.5 BIO-OIL FEEDSTOCKS .....	16
2.6 IMPACT OF UPGRADED BIO-OIL ON FCC CO-PROCESSING .....	18
2.7 CATALYTIC CRACKING MECHANISM .....	21
2.7.1 Main mechanistic routes for hydrocarbons .....	21
2.7.2 Main mechanistic routes for bio-oil molecules .....	23
3. ZEOLITES .....	25
3.1 INTRODUCTION TO ZEOLITES .....	25
3.2 Y ZEOLITE .....	27
3.3 HIERARCHICAL ZEOLITES .....	28
3.3.1 Definition of hierarchical zeolite .....	28
3.3.2 Hierarchical faujasite .....	29
4 AIM OF THIS PHD RESEARCHES .....	31
REFERENCES FOR CHAPTER I .....	33
CHAPTER II: EXPERIMENTAL METHODS.....	37
1. CHARACTERIZATION TECHNIQUES.....	37
1.1 ELEMENTARY ANALYSIS: ICP-OES TECHNIQUE .....	37
1.2 X-RAY DIFFRACTION (XRD).....	38

---

## Content

---

1.2.1	Description of the technique.....	38
1.2.2	Theory .....	38
1.3	NITROGEN ADSORPTION-DESORPTION ISOTHERMS.....	40
1.4	TRANSMISSION ELECTRONIC MICROSCOPY (TEM) .....	42
1.5	SOLID-STATE <sup>27</sup> Al AND <sup>29</sup> Si NUCLEAR MAGNETIC RESONANCE (NMR).....	42
1.5.1	Experimental parameters.....	42
1.5.2	Solid-state <sup>29</sup> Si NMR.....	42
1.5.3	Solid-state <sup>27</sup> Al NMR.....	43
<b>2.</b>	<b>CATALYTIC MICROACTIVITY TEST UNIT (MAT) .....</b>	<b>44</b>
2.1	DESCRIPTION OF THE UNIT.....	44
2.2	DESCRIPTION OF THE ANALYTICAL SETUP .....	45
2.2.1	Compact GC.....	45
2.2.2	Simulated distillation SIMDIS.....	45
2.2.3	Mass balance.....	46
2.2.4	<sup>31</sup> P NMR.....	46
2.2.5	2D-GC analysis.....	47
2.3	EXPERIMENTAL PARAMETERS .....	47
<b>3.</b>	<b>CRACKING OF MODEL MOLECULES.....</b>	<b>48</b>
3.1	DESCRIPTION OF THE TEST BENCH.....	48
3.2	DESCRIPTION OF THE ANALYTICAL SETUP .....	49
3.3	SELECTED MODEL MOLECULES .....	49
<b>4.</b>	<b>FT-IR SPECTROSCOPY OF PYRIDINE ADSORPTION ON ACID MATERIAL .....</b>	<b>50</b>
4.1	DESCRIPTION OF THE TEST BENCH.....	50
4.2	EXPERIMENTAL PROTOCOL .....	51
4.3	ANALYSIS OF IR SPECTRA.....	52
4.4	CALCULATION OF THE NUMBER OF ACID SITES.....	54
<b>5.</b>	<b>ZERO LENGTH COLUMN .....</b>	<b>55</b>
5.1	PRINCIPLE OF THE TECHNIQUE .....	55
5.2	EXPERIMENTAL SYSTEM .....	55
5.3	THEORY.....	56
5.4	TYPICAL STEPS OF ZLC MEASUREMENTS.....	57
	<b>REFERENCES FOR CHAPTER II .....</b>	<b>60</b>

<b>CHAPTER III: PREPARATION AND CHARACTERIZATION OF THE HIERARCHICAL Y ZEOLITES .....</b>	<b>63</b>
<b>1. SYNTHESIS OF THE MATERIALS .....</b>	<b>63</b>
1.1 ZEOLITE Y FROM ZEOLYST .....	63
1.2 HIERARCHICAL Y ZEOLITE WITH Si/Al=15 .....	64
<b>2. CHARACTERIZATION RESULTS.....</b>	<b>65</b>
2.1 TRANSMISSION ELECTRONIC MICROSCOPY .....	65
2.2 NITROGEN ADSORPTION-DESORPTION ISOTHERMS.....	66
2.3 X-RAY DIFFRACTION .....	69
2.4 ELEMENTARY ANALYSIS (ICP-OES) .....	70
2.5 <sup>27</sup> Al AND <sup>29</sup> Si NMR.....	71
<b>3. ZERO LENGTH COLUMN .....</b>	<b>72</b>
3.1 ION EXCHANGE .....	72
3.1.1 <i>Experimental conditions</i> .....	72
3.1.2 <i>Characterization of the Na samples</i> .....	73
3.2 DIFFUSION OF MESITYLENE .....	74
3.2.1 <i>Preliminary checks</i> .....	75
3.2.2 <i>ZLC results</i> .....	76
3.2.3 <i>Variation of D and R coefficients</i> .....	79
<b>4 CONCLUSION .....</b>	<b>81</b>
<b>REFERENCES FOR CHAPTER III .....</b>	<b>82</b>
 <b>CHAPTER IV: CATALYTIC CRACKING OF N-HEXANE OVER HIERARCHICAL Y ZEOLITES .....</b>	 <b>85</b>
<b>1. ACIDITY MEASUREMENTS USING INFRARED STUDY OF PYRIDINE ADSORBED .....</b>	<b>85</b>
1.1 QUANTIFICATION OF THE ACID SITES .....	85
1.1.1 <i>Pyridine adsorption</i> .....	85
1.1.2 <i>Hydroxyl groups</i> .....	86
1.2 STRENGTH OF THE ACID SITES .....	87
<b>2. CATALYTIC CRACKING OF N-HEXANE .....</b>	<b>88</b>
2.1 PRELIMINARY CHECK: THE DEACTIVATION OF THE CATALYST.....	88
2.2 CONVERSION .....	89
2.3 CRACKING PERFORMANCE AS A FUNCTION OF THE ACID SITE CONCENTRATION .....	91
2.4 SELECTIVITY .....	92

## Content

---

2.4.1	Selectivity as a function of the temperature.....	93
2.4.2	Reaction mechanism for the cracking of n-hexane .....	94
2.4.3	Selectivity as a function of the conversion.....	95
<b>3.</b>	<b>CATALYTIC CRACKING OF N-HEXANE AND BUTANOL .....</b>	<b>97</b>
3.1	PRELIMINARY CHECK: THE DEACTIVATION OF THE CATALYST.....	97
3.2	CONVERSION .....	98
3.3	SELECTIVITY .....	100
<b>4.</b>	<b>CONCLUSION .....</b>	<b>102</b>
	<b>REFERENCES FOR CHAPTER IV .....</b>	<b>103</b>
 <b>CHAPTER V: CO-PROCESSING OF VGO AND PDO OVER HIERARCHICAL Y ZEOLITES IN MAT UNIT ..105</b>		
<b>1.</b>	<b>INTRODUCTION .....</b>	<b>105</b>
<b>2.</b>	<b>FEEDSTOCK CHARACTERISATION.....</b>	<b>106</b>
2.1	VACUUM GAS OIL.....	106
2.2	PARTIALLY DEOXYGENATED OIL (PDO) .....	107
<b>3.</b>	<b>CATALYTIC CRACKING IN MAT UNIT .....</b>	<b>108</b>
3.1	GENERALITIES .....	108
3.2	CATALYTIC CRACKING OF PURE VGO.....	109
3.2.1	Conversion.....	109
3.2.2	Product yields .....	110
3.3	CO-PROCESSING OF VGO AND PDO.....	111
3.3.1	Conversion.....	111
3.3.2	Product yields .....	112
3.3.3	Comparison at constant coke production.....	113
3.3.4	GC x GC.....	114
3.3.5	<sup>31</sup> P NMR.....	116
3.4	COMPARISON OF THE PURE VGO AND VGO/PDO PROCESSING .....	118
3.5	COMPARISON WITH COMMERCIAL FCC CATALYST.....	118
<b>4.</b>	<b>EFFECT OF THE CATALYST ACIDITY AND POROSITY ON THE CATALYTIC CRACKING .....</b>	<b>119</b>
<b>5.</b>	<b>CONCLUSION .....</b>	<b>122</b>
	<b>REFERENCES FOR CHAPTER V .....</b>	<b>124</b>

## Content

---

CONCLUSION AND PERSPECTIVES .....	127
APPENDIX I – DETERMINATION OF THE APPARENT SURFACE AREA .....	129
APPENDIX II – DETERMINATION OF THE MICROPOROUS VOLUME .....	131
APPENDIX III – HR-TEM IMAGE OF H-USY-2 .....	132
APPENDIX IV – SMALL ANGLE OF SPEND CATALYST AFTER CRACKING OF N-HEXANE AND 2-BUTANOL .....	133
APPENDIX V – SEM IMAGES OF THE USY MATERIALS.....	134
APPENDIX VI – ESTIMATION OF THE DIFFUSION COEFFICIENT IN MAT UNIT .....	135



# Chapter I: State of the art

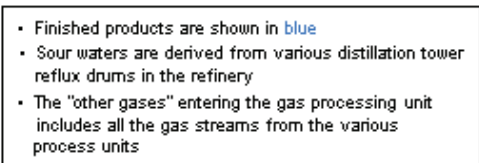
---

## 1. Context of this work

This research has been initiated as part of the European project FASTCARD (for fast industrialization by catalyst research and development) aiming to contribute to the fulfillment of the European 20-20-20 objectives [1] and the European Energy Roadmap 2050 [2] – 20% improvement in energy efficiency, 20% reduction of CO<sub>2</sub> emissions, and 20% share of renewable energy in final energy consumption by 2020; reduction in greenhouse gas emission by 80-95% below 1990 levels, respectively. To achieve these goals, the EU project promoted the bio-feedstocks conversion into advanced biofuels by developing novel catalysts and catalytic processes.

Biomass can be converted into useful fuel products via different ways, which are for example gasification, fermentation, solvent liquefaction or pyrolysis. A part of the project focuses on the valorization of the bio-oil that is obtained after pyrolysis of lignocellulosic biomass. The bio-oil obtained from this thermochemical process is a mixture of water and organic compounds that can be upgraded into transportation fuels via an extensive treatment. The co-processing of the bio-oil with conventional crude oil is a way of valorizing the production of hybrid bio-fossil fuels. In order to reach the European objectives as quickly as possible, the production process of this hybrid bio-fossil transportation fuel must already be a part of the typical oil refinery. Moreover, a process producing a considerable number of transportation fuel in proportion to worldwide massive consumption is required.

Gasoline is mainly produced from fluid catalytic cracking (FCC) units, whereas the diesel production comes from hydrotreating (HDT) units (Figure 1). The FCC units are known for their flexibility regarding the feedstock composition and answering market demands. They convert high molecular weight hydrocarbons obtained from crude oil distillation into gasoline and other valuable products. These elements make the FCC process a good candidate for the co-processing of bio-oil and fossil oil.



from the first thermal cracking process – patented by the Russian Vadimir Shukhov in 1891 – to the first FCC unit started in Standard Oil New Jersey's refinery in Baton Rouge, Louisiana in 1942 [4].

### 2.1 Description of the unit

During the 1980s, several companies developed their FCC design to be competitive in this expanding market. In Figure 2, a generic side-by-side FCC unit is schematized. In such a process, regenerated catalyst flows out of the regenerator to meet the feed at the bottom of the riser. The feed, initially at liquid state, is vaporized by the hot catalyst (650-700°C). The vapour lifts the catalyst in the riser pipe. During this time the catalyst promotes cracking reactions. At the end of the riser the temperature drops to 500-550°C because of the endothermicity of the cracking reactions. At this point, the catalyst and the reaction products are separated by a cyclone separator system. The reaction products pass to the following unit aiming to fractionate them, whereas the spent catalyst falls to a stripper. In the stripping part, the hydrocarbons entrained with the falling spent catalyst are removed with a counter-current flow of steam. Then, this spent catalyst flows to the regenerator. Its regeneration is done by injecting air with purpose to burn off the coke from the catalyst. When the catalyst is regenerated, catalyst's temperature reaches 650-700°C once again, because of the heat of combustion.

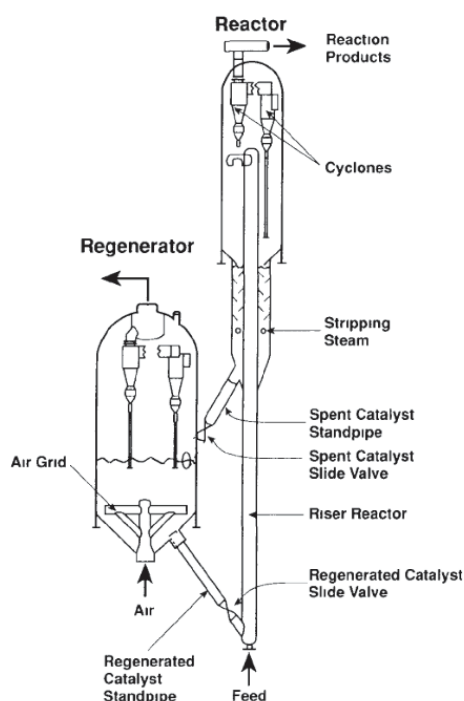


**Figure 2.** Side-by-side FCC unit. Reproduced from [5].

To give an idea of the volumes handled by such a process, the typical catalyst flux within the standpipe is  $750\text{--}1250 \text{ kg.m}^{-2}.\text{s}^{-1}$ . The typical velocity of the feed exiting the riser is  $15\text{--}20 \text{ m.s}^{-1}$ , for a

residence time between 1.8 to 2.4 s [5]. The total inventory of catalyst in an average FCC unit is 300 t, with a daily makeup rate of 4 t. Worldwide, the 350 FCC units have a capacity of over 2.4 million tonnes VGO per day (16 million barrels per day) [6].

### 2.2 Laboratory procedure for FCC testing

As depicted previously with the numbers regarding the working conditions of the FCC unit, such a process is difficult to apply at lab scale. Studies are generally carried out in a fixed-bed micro activity test (MAT) unit, according to ASTM D-3907 method. To mimic the FCC process, a four-step reaction cycle is performed, including purge, cracking, stripping and regeneration (Figure 3).

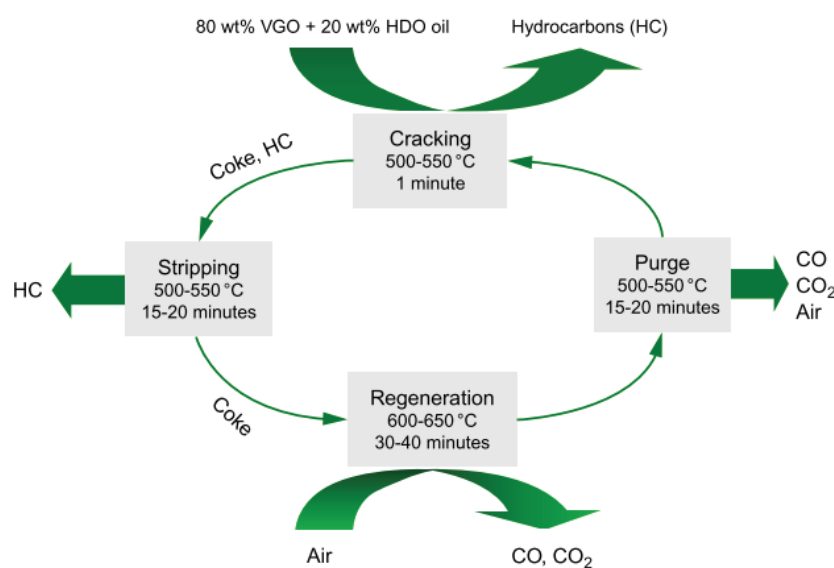


**Figure 3.** Catalytic cracking cycle simulated in a fixed-bed reactor (reproduced from [7])

Corma et al. [8] underlined some drawbacks at this process:

- Continuous catalyst deactivation during the test could induce variation of conversion and selectivity between the beginning and the end of the test.
- Coke and temperature profile can appear through the catalyst bed, which changes activity and selectivity during the test.
- The contact time between the catalyst and the feed can be an order of magnitude longer than in the industrial unit, which increases the coke-on-catalyst values.
- Gas residence time is different than in industrial FCC unit, which can affect prediction on dry gas yield.

These effects may give inaccurate predictions when extrapolating to a commercial unit. Nevertheless, the fixed-bed provides useful insights on the activity and selectivity of catalysts and

therefore is widely used in research centre for its ability to process different feedstocks and catalysts [9]–[11].

### 2.3 FCC Catalyst

The FCC catalyst is composed of microspheres, typically produced by spray drying. The average particle size is 70  $\mu\text{m}$ . The formulation of these particles depends on the manufacturer, but the same families of components are always present [4]:

- Zeolite, usually ultra-stable Y-zeolite, which contains active sites where the cracking reactions take place. It corresponds to 10-30 wt. % of the FCC catalyst.
- An active matrix, made of alumina, which is acidic and displays large pores. It promotes the pre-cracking of the heaviest molecules.
- An inert matrix, which is clay, like kaolin, used for its physical properties.
- A binder that keeps bounded all the components.

A scheme of these elements is displayed in Figure 4. Various formulations, aiming to change the coke formation, to promote the formation of particular product families or to get poisoning resistance are continuously developed and delivered to the FCC market.

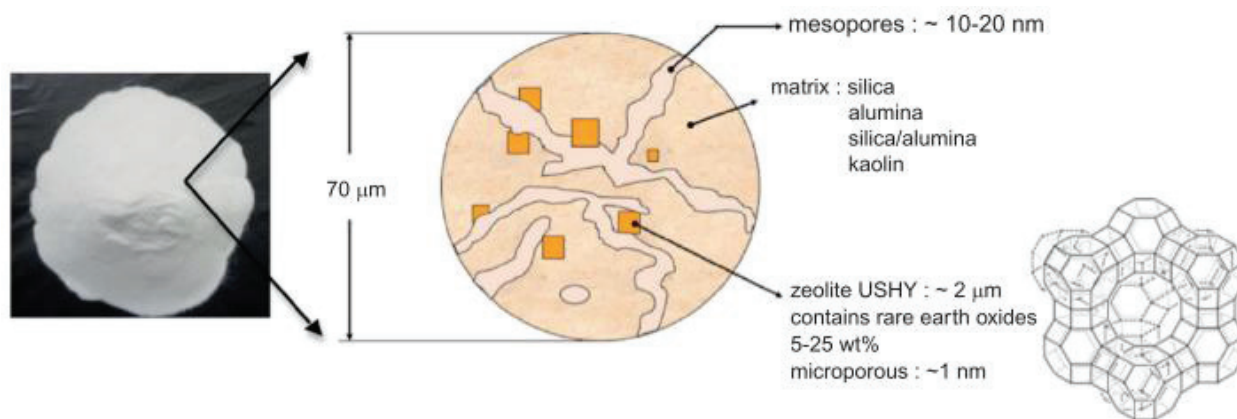


**Figure 4.** Equilibrated FCC catalyst. Reproduced from [7].

To be useful as a FCC catalyst the zeolite must be able to withstand high temperature and steam environment. Stabilization of the Y zeolite can be achieved with addition of rare earth ions and tuning of Si/Al ratio using steam and/or acid treatments. Zeolite Y with a framework Si/Al ratio of 6 and higher are considered as “ultra-stable” (USY) due to their improved catalytic and hydrothermal stability [12].

## 2.4 Industrial fossil feedstocks

The typical FCC feedstock is a very complex mixture of hydrocarbons. Typically, it contains heavy atmospheric and vacuum gas oil with an average boiling point of 344-550°C and molecules having from 10 to 45 carbon atoms (Table 1 and Figure 5). All kind of paraffins, olefins, naphthenes and multi-aromatic ring structures are found in such mixture. Moreover, heteroatoms or metal particles, like sulphur, nitrogen, nickel and vanadium, may be present within the feedstock. They come from either the interactions of the crude oil with rock formation, or because of the organic form of the crude oil millions of years ago. The accumulation of metals on the catalyst surface can result in promotion of dehydrogenation reactions, degradation of zeolite activity or decrease of the products quality. The reduction in usual crude oil availability increases the need to process different types of feedstock, uprising process issues that need to be solved.

**Table 1.** Carbon number, boiling point and number of paraffin isomers for the different petroleum cuts. Reproduced from [13].

Carbon no.	Boiling point <sup>a</sup>			Examples of petrol. distill. cuts
	(°C)	(°F)	Isomers	
5	36	97	3	Gasoline
8	126	258	18	
10	174	345	75	
12	216	421	355	Diesel and jet fuels, middle distillates
15	271	519	4347	
20	344	651	$3.66 \cdot 10^5$	Vacuum gas oil
25	402	755	$3.67 \cdot 10^7$	
30	449	840	$4.11 \cdot 10^9$	Atmospheric residue
35	489	912	$4.93 \cdot 10^{11}$	
40	522	972	$6.24 \cdot 10^{13}$	
45	550	1022	$8.22 \cdot 10^{15}$	Vacuum residue, asphalt
60	615	1139	$2.21 \cdot 10^{22}$	
80	672	1242	$1.06 \cdot 10^{31}$	Nondistillable residue
100	708	1306	$5.92 \cdot 10^{39}$	

<sup>a</sup>Atmospheric equivalent boiling point (AEBP) of *n*-alkanes.

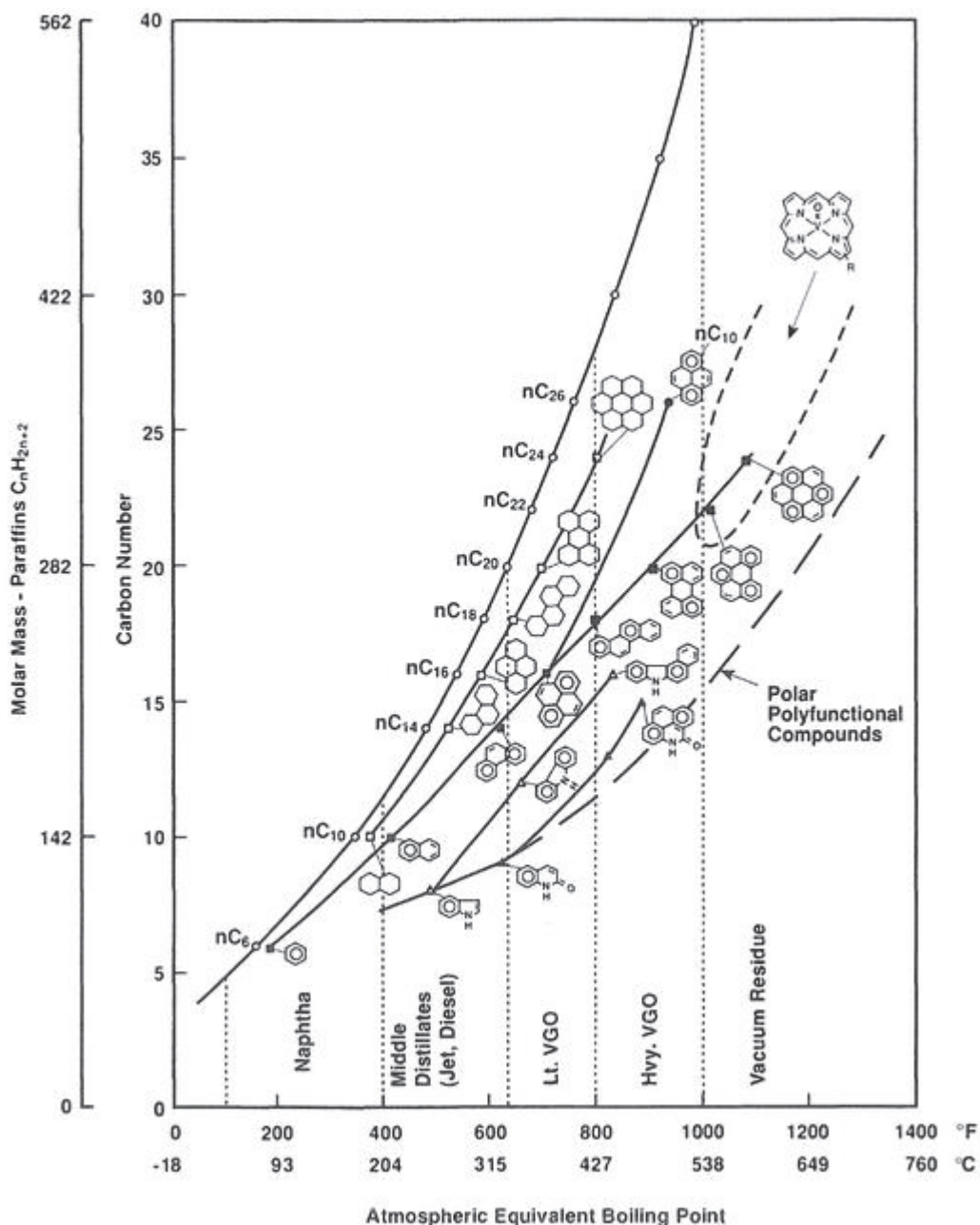


**Figure 5.** Effect of molecular structure on boiling point. Reproduced from [13].

## 2.5 Bio-oil feedstocks

Various sources are available for the production of liquid fuels (Figure 6):

- Food crops such as corn, wheat, barley, sugar crops or vegetable oils. It corresponds to edible biomass.
- Waste materials such as agricultural residues, urban wastes, crop residues or wood, which correspond to lignocellulosic biomass.
- Aquatic biomass such as algae.



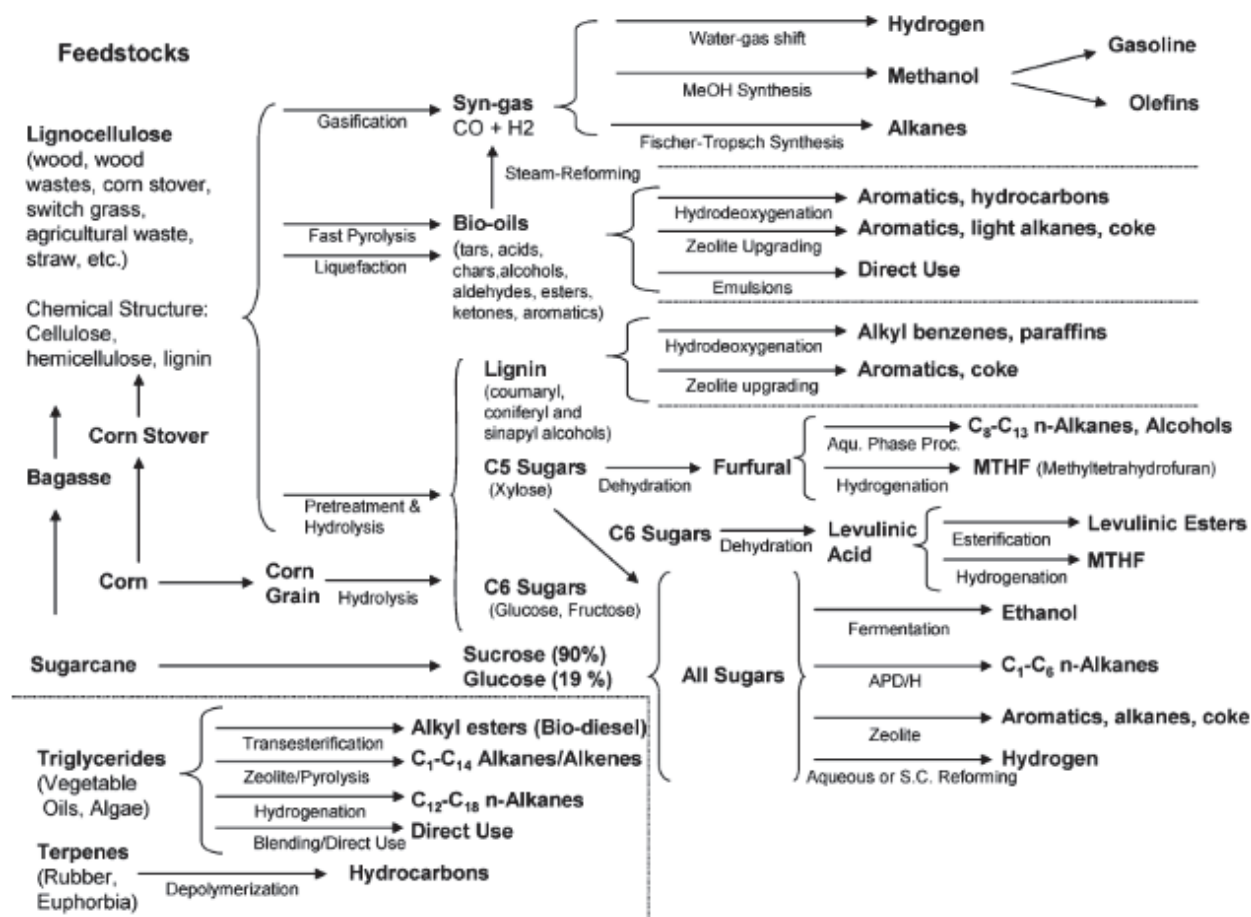


Figure 6. Routes for biomass valorization. Reproduced from [14].

The bio-feedstock that suits for refinery needs to be available in large scale to provide biofuel in large quantity. Moreover, the costs of the raw-biomass and of its conversion must be limited to be competitive. Among the different feedstocks, the lignocellulosic ones are particularly interesting for the co-processing of bio-sourced feedstock with fossil oil. A transformation of lignocellulose via fast pyrolysis results in liquid bio-oil, containing a large range of products, as illustrated in Figure 7.

Fast pyrolysis consists of a thermal decomposition of biomass in the absence of oxygen and atmospheric pressure, resulting in the production of char, non-condensable gas and condensable vapours. A maximum quantity of liquids (bio-oil) is obtained due to the high rate of particle heating to temperatures round 500°C and a rapid cooling of the produced vapours to condense the liquids [15]. This process is exploited on a commercial scale [16].

Looking at the compounds obtained after lignocellulose decomposition (Figure 7), some differences with typical crude oil are obvious: (i) high oxygen content; (ii) higher boiling of oxygenated compounds than hydrocarbon with same carbon number; (iii) presence of water, which is considered



as a contaminant in refineries; (iv) higher acidity than crude oil; (v) the oxygen-related functionalities might lead to thermal polymerization of this feedstock. The comparison between fossil and bio-oil can be made by considering hydrogen-to-carbon (H/C) and oxygen-to-carbon (O/C) ratios. Typically, the H/C and O/C ratios of the fossil oil are between 1.6-2.1 and 0-0.03, respectively. For wood-based bio-oil, the H/C and O/C ratios are higher than 1.4 and 0.61, respectively [17]. Hence, the upgrading and removal of the oxygen from liquid bio-oil are necessary to make it an operable feedstock, which is done by hydrodeoxygenation process. However, this H<sub>2</sub> consuming treatment results in an increase of the overall cost. Solutions to process mildly hydrodeoxygenated bio-oil would greatly favour its industrial interest.

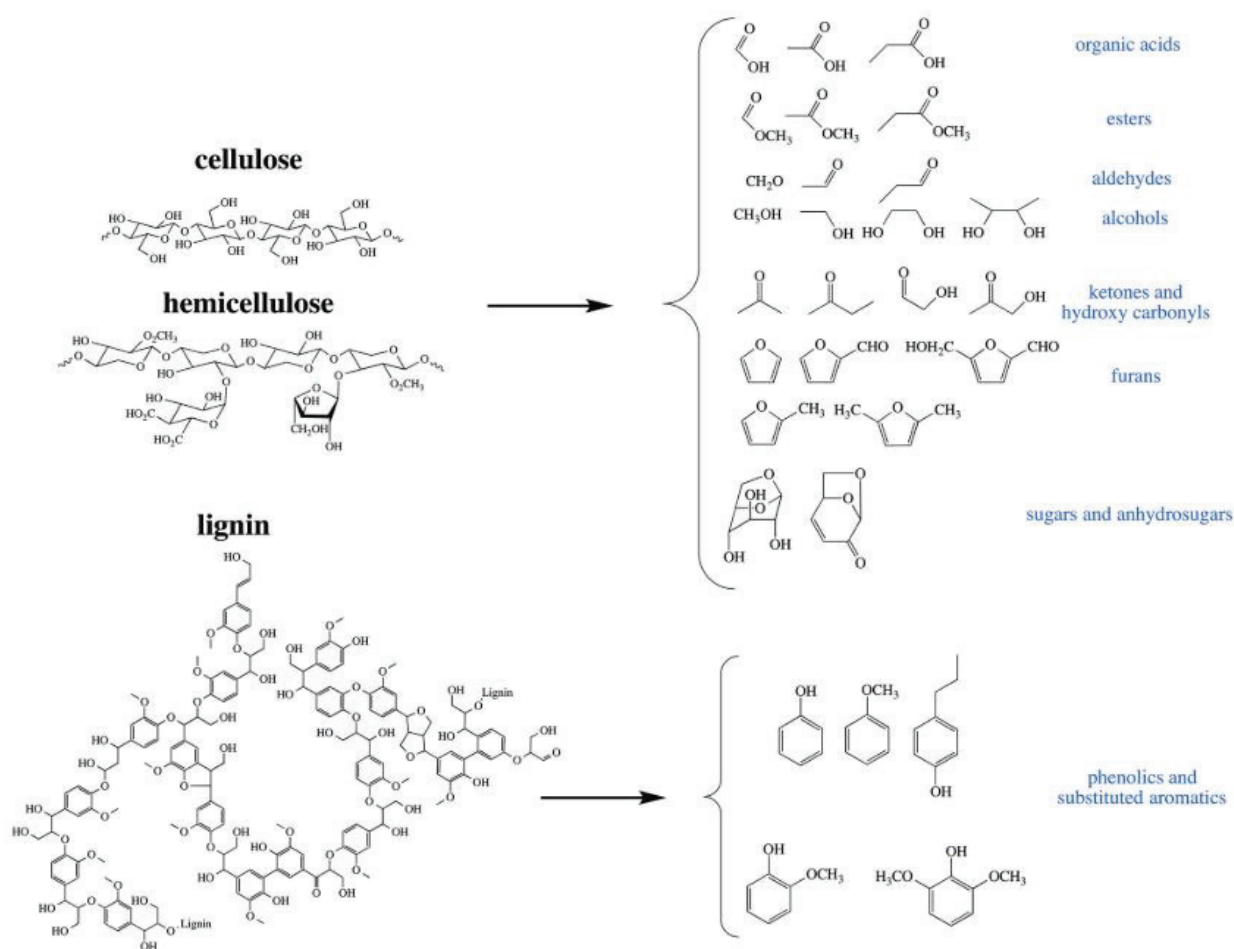


**Figure 7.** Typical products formed from pyrolysis of biomass. Reproduced from [18].

### 2.6 Impact of upgraded bio-oil on FCC co-processing

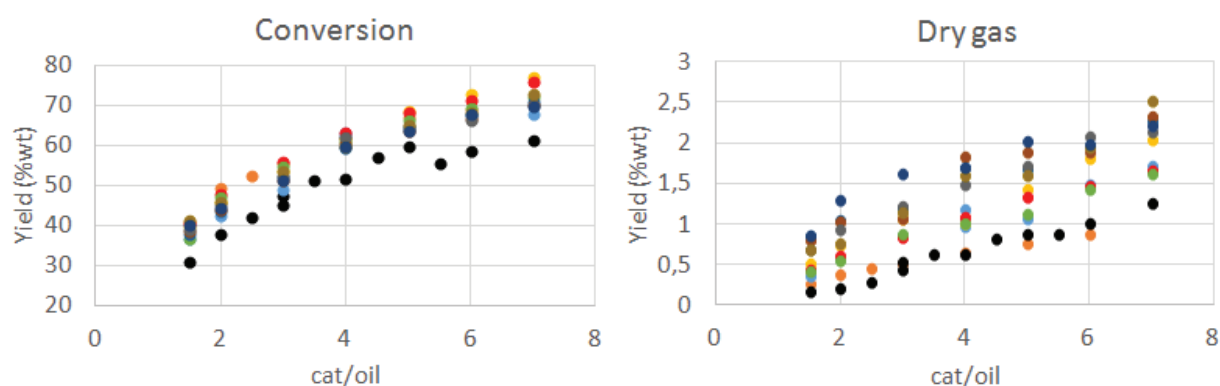
To evaluate the impact of the co-processing of bio-oil in a conventional FCC unit, it is interesting to look at some case studies already performed with either model molecules or hydrodeoxygenated bio-oil.

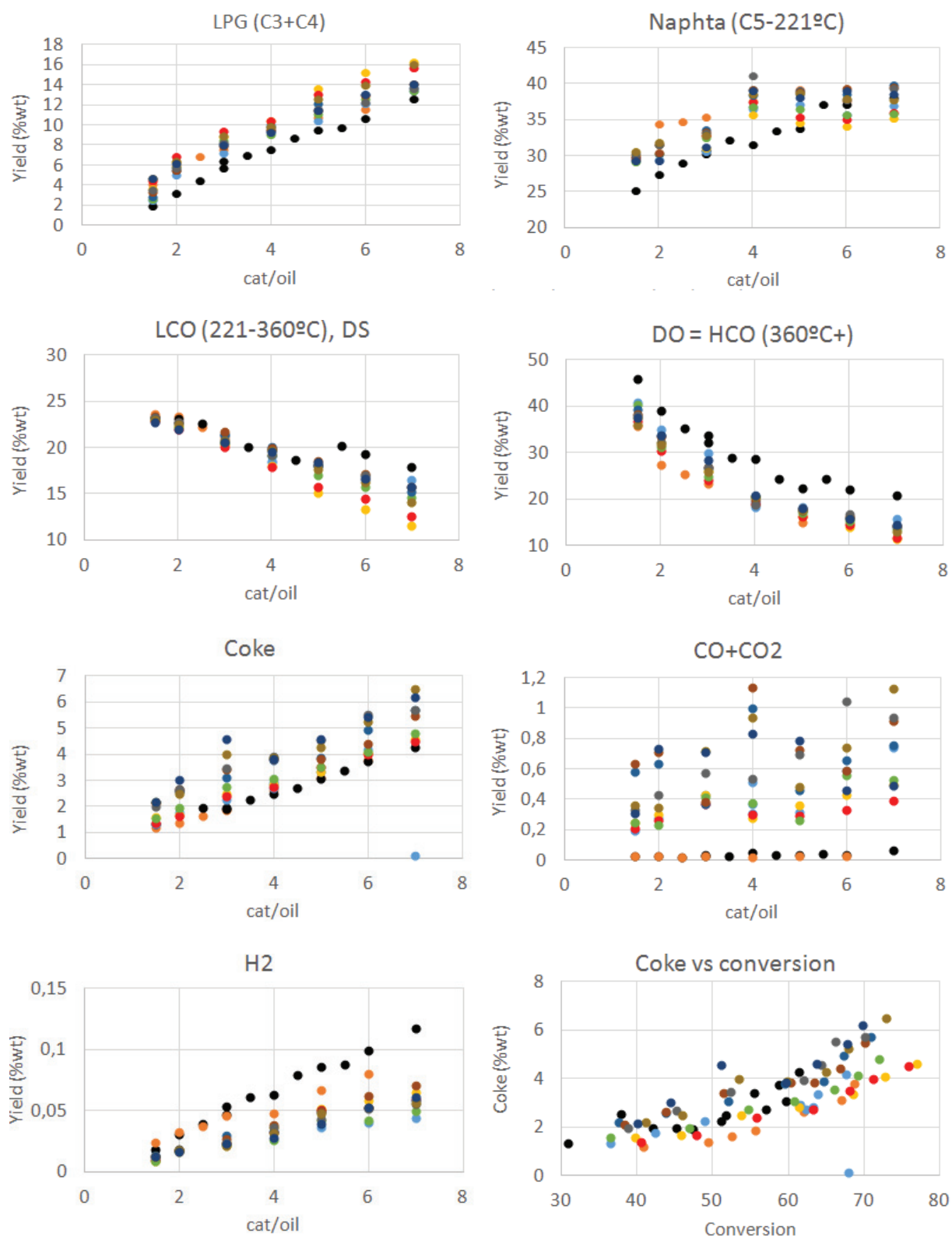
Corma et al. [19] used glycerol and sorbitol as representative of biomass-derived oxygenates to conduct catalytic cracking over various catalysts (FCC catalyst, mesoporous  $\text{Al}_2\text{O}_3$ , USY zeolite, ZSM-5, inert silicon carbide) in MAT unit. From the product selectivity, they found that the oxygen was removed as  $\text{H}_2\text{O}$ ,  $\text{CO}$  and  $\text{CO}_2$ . The repeated dehydrations and hydrogen transfers allow the production of olefins, paraffins, and coke. When co-processing of glycerol together with a vacuum gasoil was carried out, interactions between the hydrocarbon components and the glycerol reaction intermediates resulted in better final selectivities than those calculated by considering a simple additive effect.

The co-feeding of guaiacol with gas-oil over FCC catalyst was studied by Graça et al. [20]. A negative effect of guaiacol on gasoil conversion was observed: it increased the coke retained on the catalyst. Aromatic products were obtained in gasoline fraction products because of the dehydration of guaiacol.

De Rezende Pinho et al. [21], from Petrobras, have co-processed raw bio-oil and gasoil over equilibrated FCC catalyst, at pilot scale. When 10% of bio-oil was co-processed, similar product yields for LPG, gasoline and LCO fractions were obtained in comparison with pure VGO processing. Product deterioration appeared for co-processing carried-out with 20% of bio-oil. These results showed the feasibility of the co-processing in a demonstration-scale unit. Interestingly, fewer coke deposits than it was suggested from lab-scale unit prediction were formed.

At IRCELYON, Gueudré performed experiments on a micro activity test unit with a commercial FCC catalyst and a mixture of VGO and various upgraded bio-oils (Figure 8). Conversion was slightly improved with these blends and a larger proportion of light compounds were produced (dry gas, LPG, naphtha). However, the coke proportion was also higher for the VGO/bio-oil mixtures than the pure VGO.





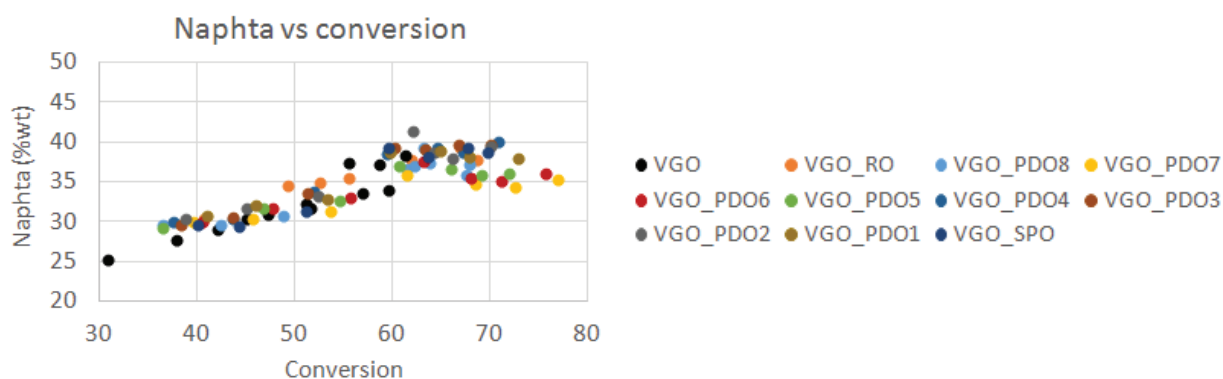


**Figure 8.** Co-processing of 90% VGO and 10% bio-oil in MAT unit at 560°C [22].

## 2.7 Catalytic cracking mechanism

### 2.7.1 Main mechanistic routes for hydrocarbons

Reactional mechanisms have been proposed to contribute to the understanding of what happens during catalytic cracking of the various feedstocks. Regarding catalytic cracking of hydrocarbons, mechanisms have been for a long time discussed and it is now well accepted that carbocations are reaction intermediates. Figure 9 illustrates the description given by Vogt et Weckhuysen [23] for the role of the carbocation intermediates and hydrogen transfer via both Lewis and Brønsted acid sites. Alkane can either receive a proton from BAS or give a hydride to LAS to form carbonium or carbenium ions, respectively. By giving a proton to an alkene, the carbenium ion can also be formed by BAS. The carbonium ions formed from step 1 crack through protolytic cracking. The protolytic cracking can either form same-sized carbenium ion and dihydrogen, or smaller carbenium ion and alkane. This carbenium ion, as well as the ones formed as described previously crack through  $\beta$ -scission, forming smaller carbenium ions and small alkene. Finally, the smaller carbenium ions desorb from acid site via one of the following pathways: (i) hydride transfer from a larger alkane, which leaves a new larger carbenium ion on the acid sites; (ii) proton transfer back to the zeolite BAS to form an alkene; (iii) hydride transfer back from zeolite LAS to form an alkane.

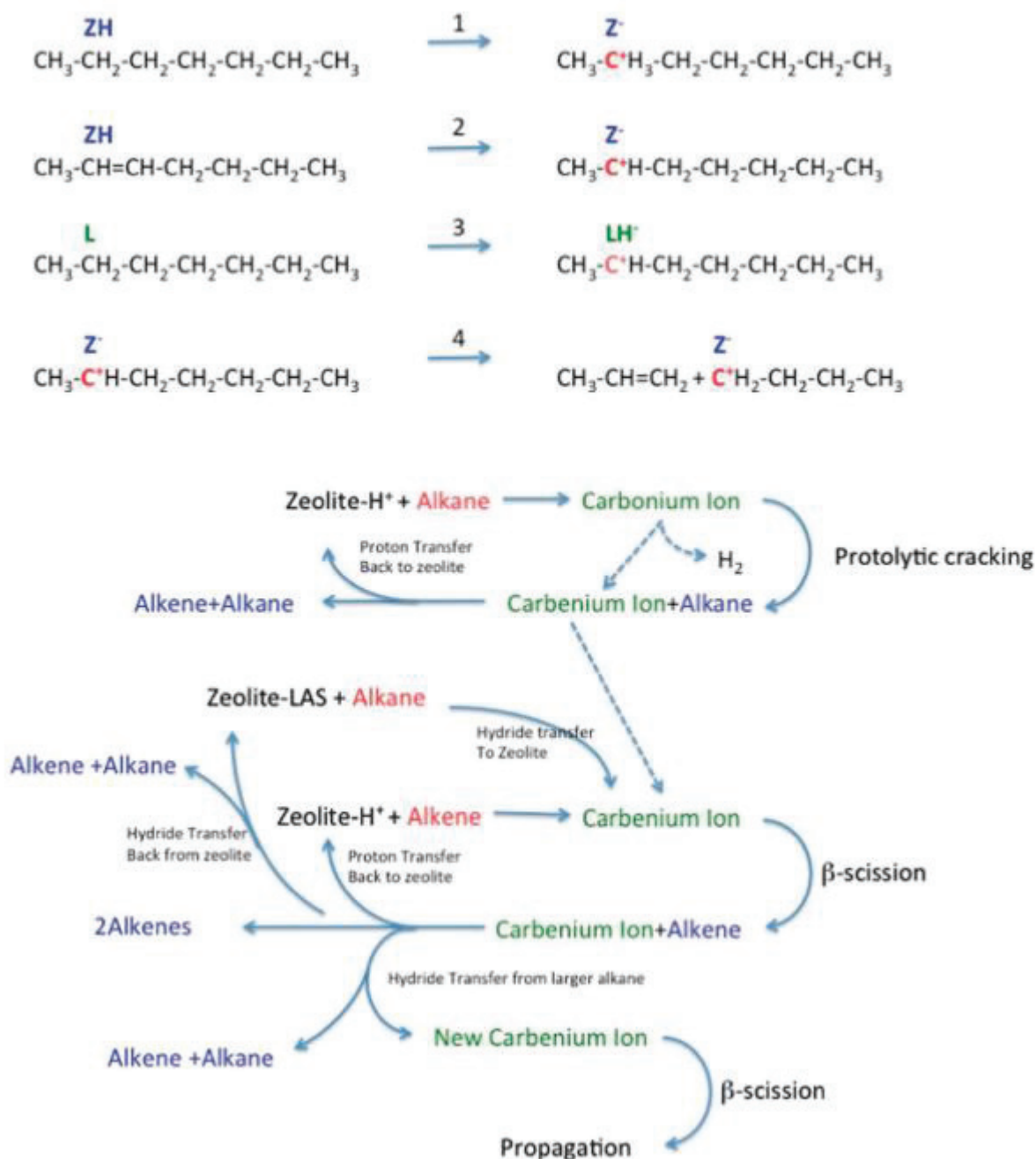


**Figure 9.** Reaction network in zeolite-assisted cracking of hydrocarbon molecules. (1): proton transfer from the zeolite Brønsted acid site to an alkane to form a carbonium ion. (2): proton transfer from the zeolite to an alkene to form a carbenium ion. (3): hydride transfer from an alkane to the zeolite to form a carbenium ion. (4): β-scission of a carbenium ion to form a new carbenium ion and an alkene. Reproduced from [23].

To complete this cracking mechanism of alkane and alkene, Figure 10 summarizes the various reactions happening during the cracking process. This work published by Vermeiren and Gilson [24] lists the reactions for paraffins, olefins, naphthenes and aromatics. Other secondary reactions happen during the catalytic cracking: isomerization, dehydrogenation, trans alkylation, side-chain

cracking, and polycondensation. They also underlined the key role of hydrogen transfer between olefin and naphthenes. This is particularly favoured by a confined environment around zeolite acid sites. Hence, the reaction  $3 \text{ Olefins} + 1 \text{ Naphthene} \leftrightarrow 3 \text{ Paraffins} + 1 \text{ Aromatic}$  is displaced to the right hand due to lower reactivity.

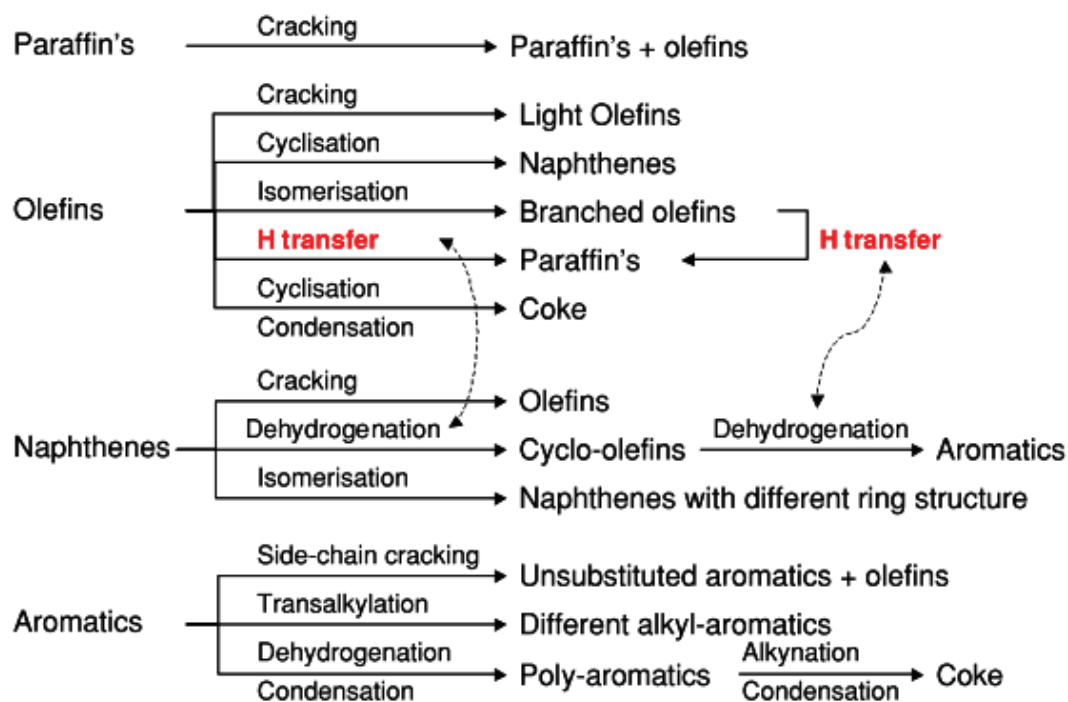


**Figure 10.** Main reactions observed during the cracking of hydrocarbons molecules. Reproduced from [24].

### 2.7.2 Main mechanistic routes for bio-oil molecules

In their study on the cracking of glycerol and sorbitol, Corma et al. [19] proposed a reaction network for the removal of oxygen from biomass-derived oxygenates in FCC process. A first route, producing hydrogen through various reactions is displayed in Figure 11: (i) decarbonylation of the feedstock or the partially dehydrated species; (ii) steam-reforming reactions; (iii) water gas shift reaction with carbon monoxide obtained from (i) and (ii); (iv) dehydrogenation of the carbohydrates and hydrocarbons. These reactions agree with the CO, CO<sub>2</sub>, coke and H<sub>2</sub> they observed experimentally.

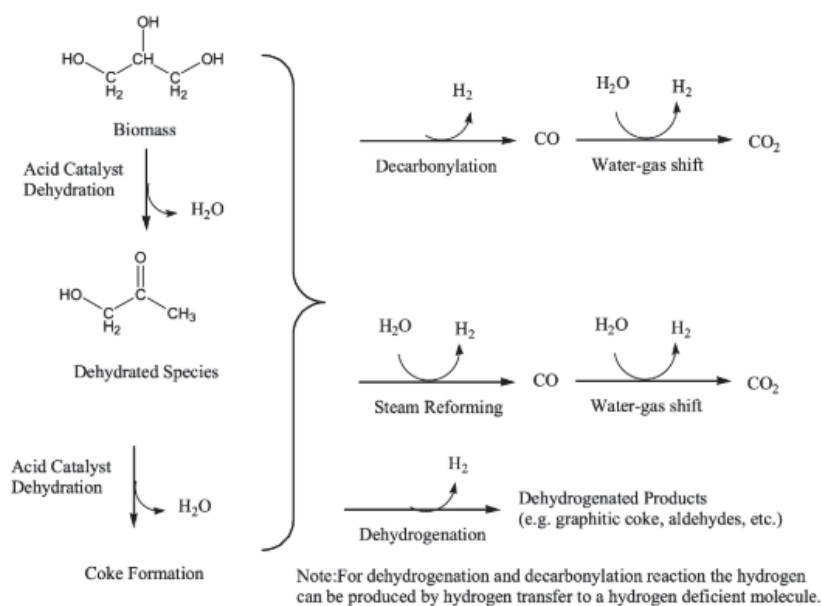


**Figure 11.** Hydrogen producing reactions for catalytic cracking of biomass. Reproduced from [19].

A second group of reactions, consuming the hydrogen produced, is also believed to happen in parallel (Figure 12). Hydrogenation and/or hydrogen transfer on dehydrated product lead to the formation of olefins and alkanes. Hydrogenation reactions are promoted by metal and metal oxide impurities that might be present on the zeolite surface. Aromatics and larger products can be obtained by condensation of hydrogenated intermediates and Diels-Alder reaction of olefins.

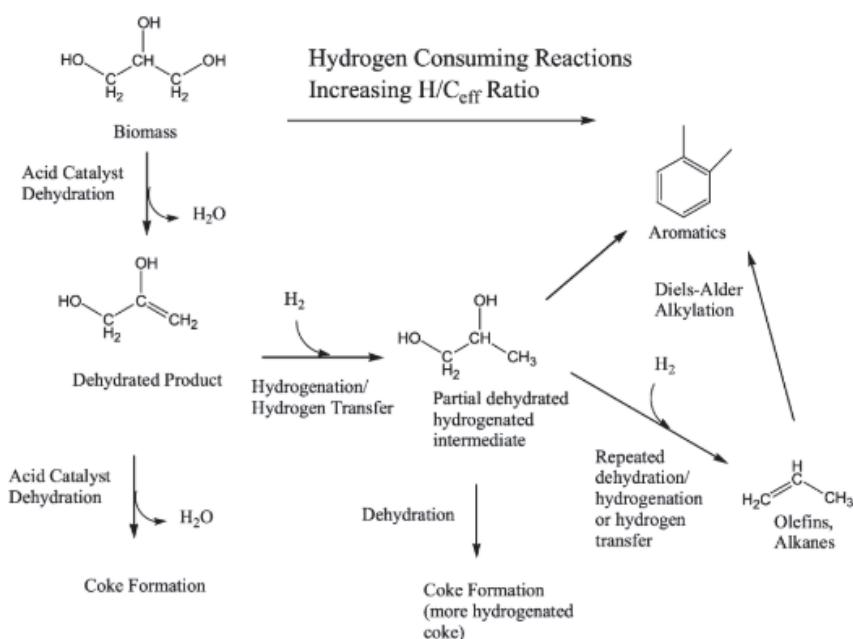


**Figure 12.** Hydrogen consuming reactions for catalytic cracking of biomass. Reproduced from [19].



Fogassy et al. [25] considered the molecular access in FCC catalyst. They showed that the lignin polymer fragments that are contained in pyrolysis oil cannot enter the zeolite micropores. The pre-cracking and deoxygenation must occur on extra framework structure – either the matrix or extra framework aluminium. A tentative mechanistic scheme, illustrated in Figure 13, has been proposed for this cracking of lignin fragments in the extra-framework space. During these cracking steps, a proton is transferred to the phenolic fragment, before regeneration via formation of olefins. It illustrates the competition between the degradation of oxygenates and the cracking of VGO hydrocarbons. Following this primary cracking, molecules having a kinetic diameter below 0.74 nm – in the case of catalytic cracking with Y zeolite – may enter into zeolite framework. Considering these kinetic size considerations, it would be interesting to investigate the effect of zeolite structure on lignin fragment conversion and coke deposition.

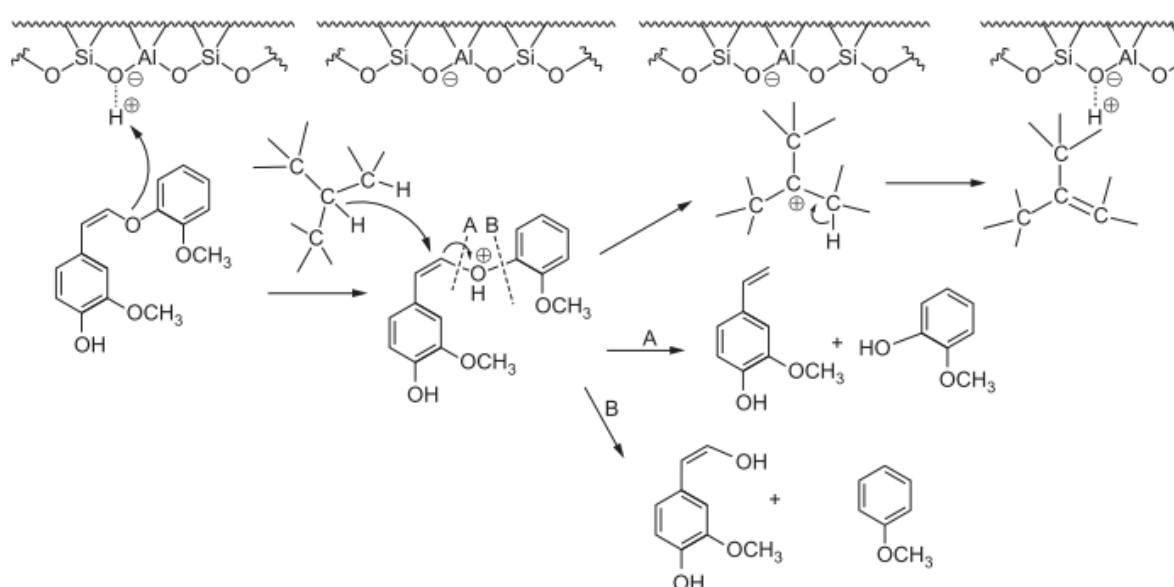


**Figure 13.** Lignin fragments degradation mechanism on the outer zeolite surface. Reproduced from [25].

## 3. Zeolites

### 3.1 Introduction to zeolites

Zeolites are crystalline microporous aluminosilicates. It consists of  $[\text{SiO}_4]^{4-}$  and  $[\text{AlO}_4]^{5-}$  tetrahedrons assembly, linked together via common oxygen atoms, resulting in a three-dimensional framework. Depending on tetrahedrons structural arrangements, the zeolite framework contains channels, channel intersections and cages of various dimensions (Figure 14).



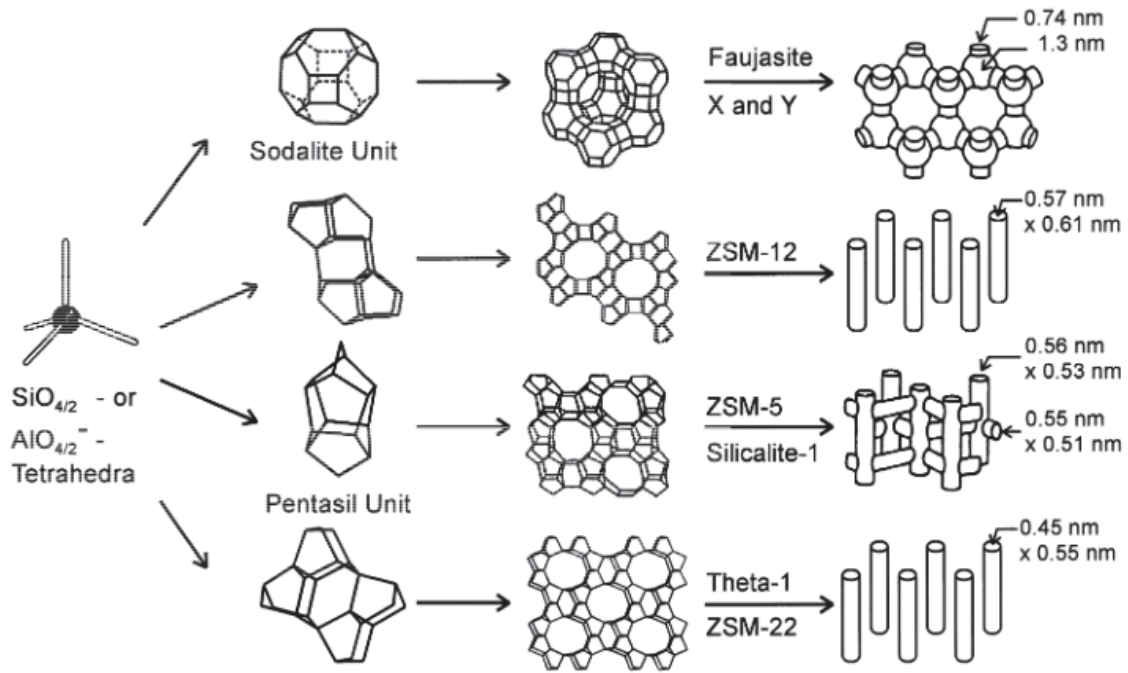


**Figure 14.** Structures of four zeolites and their micropores dimensions. Reproduced from [26].

Because of the shared atoms, the net formulae of the tetrahedrons are  $\text{SiO}_2$  and  $\text{AlO}_2^-$ . Hence, one negative charge needs to be compensated for each tetrahedron having an aluminium atom in its centre. This is done by cations, which are loosely associated with the framework oxygens, and the remaining pore volume is filled with water molecules. The non-framework cations are generally exchangeable and the water molecules removable. When this negative charge is balanced by a proton, it generates Brønsted acid sites (Figure 15a). Default in zeolite lattice, or loss of water molecules at high temperatures, create Lewis acid sites (Figure 15b). These acid properties may be influenced by other parameters like framework density, type of cation or local strain [27].

The chemical composition of a zeolite is represented by the following formula:

$$A_{y/m}^{m+}[(\text{SiO}_2)_x \cdot (\text{AlO}_2^-)_y] \cdot z\text{H}_2\text{O}$$

Where:

- A is a cation with the charge m
- (x+y) is the number of tetrahedral per crystallographic unit cell
- x/y is the framework silicon to aluminium ratio (Si/Al)
- z depends on the degree of hydration

According to Lowenstein's rule, two contiguous tetrahedrons cannot contain aluminium centre, i.e Al-O-Al linkages. Hence, the Si/Al ratio ranges from 1 to infinite.

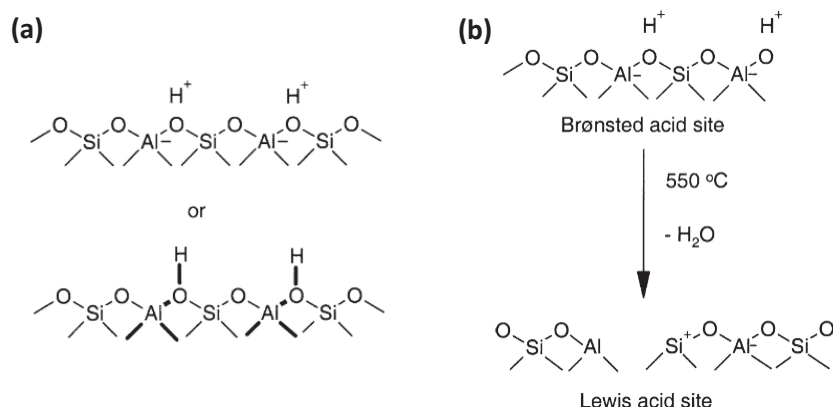


**Figure 15.** (a) Brønsted acid site and (b) formation of Lewis acid sites in zeolites. Reproduced from [27].

More than 230 different zeolite framework types are referenced by the International Zeolite Association (IZA) [28], and around forty of them can be found at the natural stage. However, the homogeneity in composition and properties that are sometimes required by some industrial processes limited the development of these latter. Synthetic zeolites did not face the same issue and their industrial use became increasingly important since their first synthesis in the 1950s by Milton and Breck [29]–[31].

In 2014, the global zeolite market size valued at US\$ 29 Billion, with synthetic zeolites accounted for 71% share [32]. Their main applications are catalysis, gas separation and ion exchange. The Y-zeolite, which has a faujasite type structure (FAU), is widely used in the oil industry for the catalytic cracking because of its acidic properties and hydrothermal stability [33].

### 3.2 Y zeolite

X-zeolite and Y-zeolite are the two materials belonging to the FAU structure. Zeolite X differs from zeolite Y by its Si/Al ratio, which is typically in the range from 1 to 1.5 for the X and higher for the Y-type zeolite. The composite building units of Y zeolite, the sodalite cages, contain 24  $TO_4$  tetrahedrons, with  $T = \text{Si or Al}$ . They are linked via double six-ring (Figure 16). Due to this arrangement, cavities – named supercages – with a pore diameter of 1.3nm are formed. The diameter of the pore entrance is 0.74nm [33]. This material combines high surface area, high pore volume, solid acidity (both Brønsted and Lewis) with sufficient room to allow bimolecular cracking.

The stability of the zeolite towards hydrothermal conditions can be improved by controlled steaming and washing/leaching cycles to make the so-called ultra-stable Y zeolite (USY) [23].

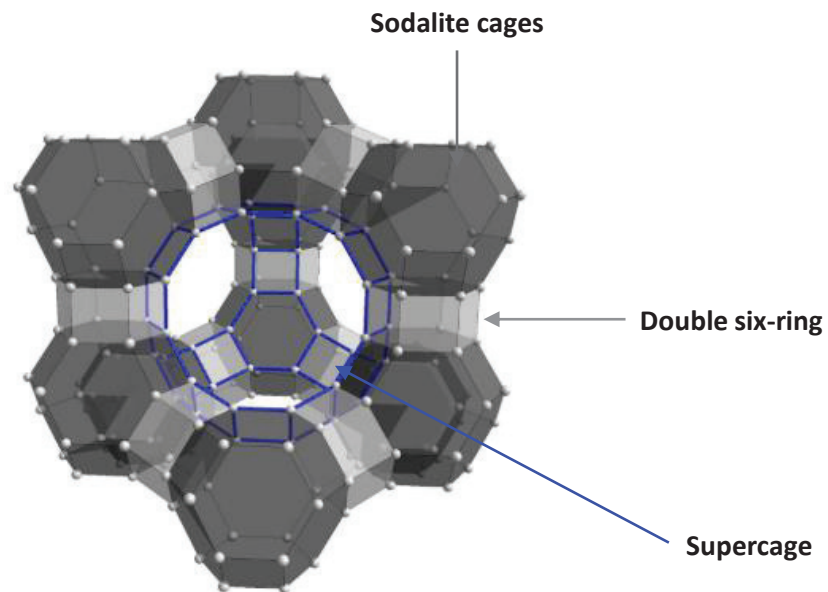


**Figure 16.** Faujasite framework showing only the tetrahedral central atoms (Si or Al). Adapted from [34].

### 3.3 Hierarchical zeolites

#### 3.3.1 Definition of hierarchical zeolite

According to Schwieger et al. [35], to be called “hierarchical”, a material has to fulfil two criteria:

- Its structural elements have to be characterised by more than one length scale
- Each of these structural elements has to have a very distinct but complementary function

Hence, we are surrounded by various types of hierarchical systems like electricity, water and gas supply in the cities, roots of the trees or lungs and blood circuit in the human body for example.

In respect to porous materials, “hierarchy” is often used in a broad sense for systems that contain a certain number of different pore types, independently of their interconnections. However, in the narrow sense of “hierarchical”, an interplay between the different pore levels is necessary. Based on these considerations, Schwieger et al. defined two types of pore systems (Figure 17). Hierarchy-type I that subdivides into several species at each level. Hierarchy-type II that corresponds to interconnected pore systems of different pore size where the larger pores intersect the smaller pore system.

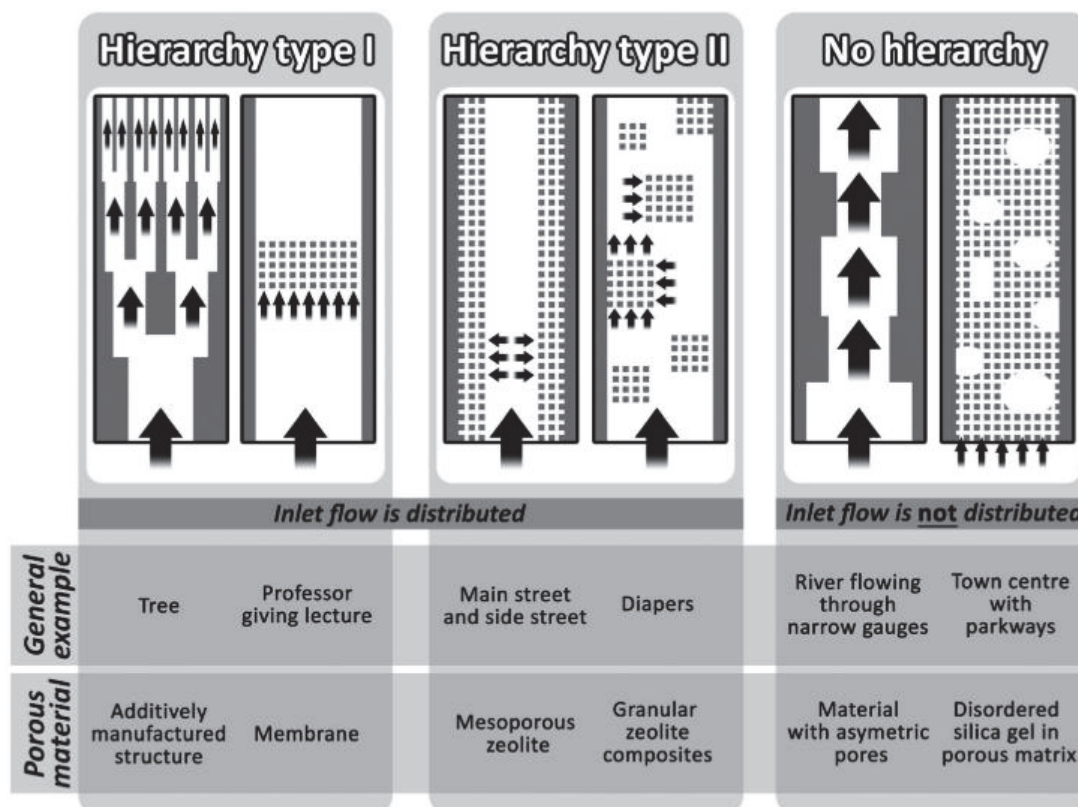


**Figure 17.** Schematic representation of the proposed classification by Schwieger et al. for hierarchical pore systems and related examples. Reproduced from [35]

### 3.3.2 Hierarchical faujasite

Verboekend et al. [12] published a very complete review on the synthesis of hierarchical faujasite zeolites. They underlined the fact that the secondary porosity should enhance the task of the active sites located in the micropores of the zeolite. Therefore, the mesoporosity should be accessible from the outside of the zeolite crystals. It means that the steaming of zeolites, which is used for stabilizing Y zeolite and form mesoporous isolated cavities in the crystals, does not lead to “hierarchical” materials. Figure 18 summarizes the strategies developed in the literature for bottom-up (i.e. primary syntheses) and top-down (i.e. post-synthetic modification) preparation treatments.

Bottom-up syntheses often use addition of templates in hydrothermal synthesis of zeolite. The crystal growth around the template leads, after removal of the template, to the formation of crystals with intracrystalline cavities. This template is called “hard” for carbon black, carbon nanotube or ordered mesoporous carbon and “soft” for cationic surfactant or organic compound. For example, Inayat et al. [36] prepared hierarchical X zeolite by including 3-(trimethoxysilyl)propyl hexadecyl dimethyl ammonium chloride (TPHAC) as template in the hydrothermal synthesis (Figure 18a). On their side Awala et al. [37] succeed to prepared template-free nanosized faujasite-type zeolite (Figure

18e). The small crystallites (10-15nm), with narrow particle size, gives rise to intracrystalline voids. The resulting bi-modal porosity confers hierarchical properties to the obtained material. However, these materials are actually limited to low Si/Al ratio because of stability complications.

The top-down approach refers to post-synthetic modifications of zeolite crystals. It includes:

- Dealumination by acid treatment (Figure 18b, d and j). For example, mesoporosity was formed in Y faujasite by treatment with H<sub>4</sub>EDTA [38].
- Desilication by alkaline solution. However, an initial dealumination of the zeolites seems to be necessary to obtain efficient desilication treatment (Figure 18f) [39]. This prior dealumination can be done by steaming or acid treatment and followed by a leaching with NaOH alkaline solution (Figure 18c and k) [40], [41].
- Pseudomorphic synthesis (also referred as mesostructuring [42], recrystallization [43] or riving [44]), which corresponds to the transformation of a parent zeolite crystal by recrystallization in the presence of surfactant [45]. For example, this has been done by Garcia-Martinez et al. [44] on USY zeolite by contacting the zeolite in an aqueous solution of NH<sub>4</sub>OH with cetyltrimethylammonium bromine (CTAB), leading to the formation of an ordered mesoporous phase.

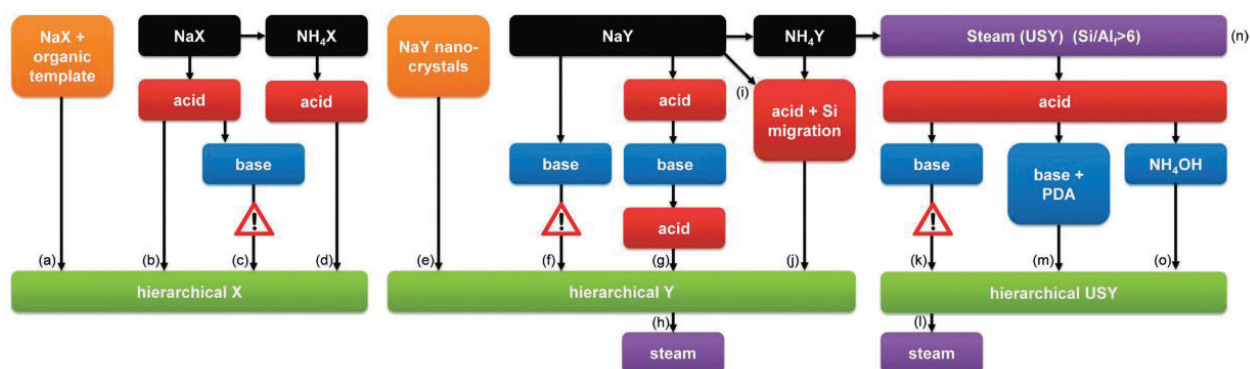


**Figure 18.** The synthesis of hierarchical faujasite using bottom-up (orange) and top-down strategies. Reproduced from [12]. The exclamation mark in: (c) indicates that this strategy has not proven more beneficial than (b); (f) indicates that base treatment on parent Y zeolites is inefficient; (k) highlights the severe amorphization that USY zeolites undergo in inorganic bases.

The different preparation routes usually yield in materials with short diffusion path lengths, resulting in improved mass transfer properties. This improvement enables higher activities and/or kinetics of catalytic and sorption processes. Garcia-Martinez et al [44] published the testing of mesostructured zeolite Y carried out in Advanced Cracking Evaluation (ACE) unit. The catalyst showed improved

selectivity in product yields (more gasoline and light cycle oils (LCO); less coke and un-converted bottoms) in comparison with the parent USY zeolite (Figure 19). However, the application of hierarchical zeolites in biomass conversion has not yet been very well studied. Some study regarding bio-oil upgrading exhibit the good performances of hierarchical materials, but catalytic cracking of bio-oil with such materials as not been reported [46], [47].

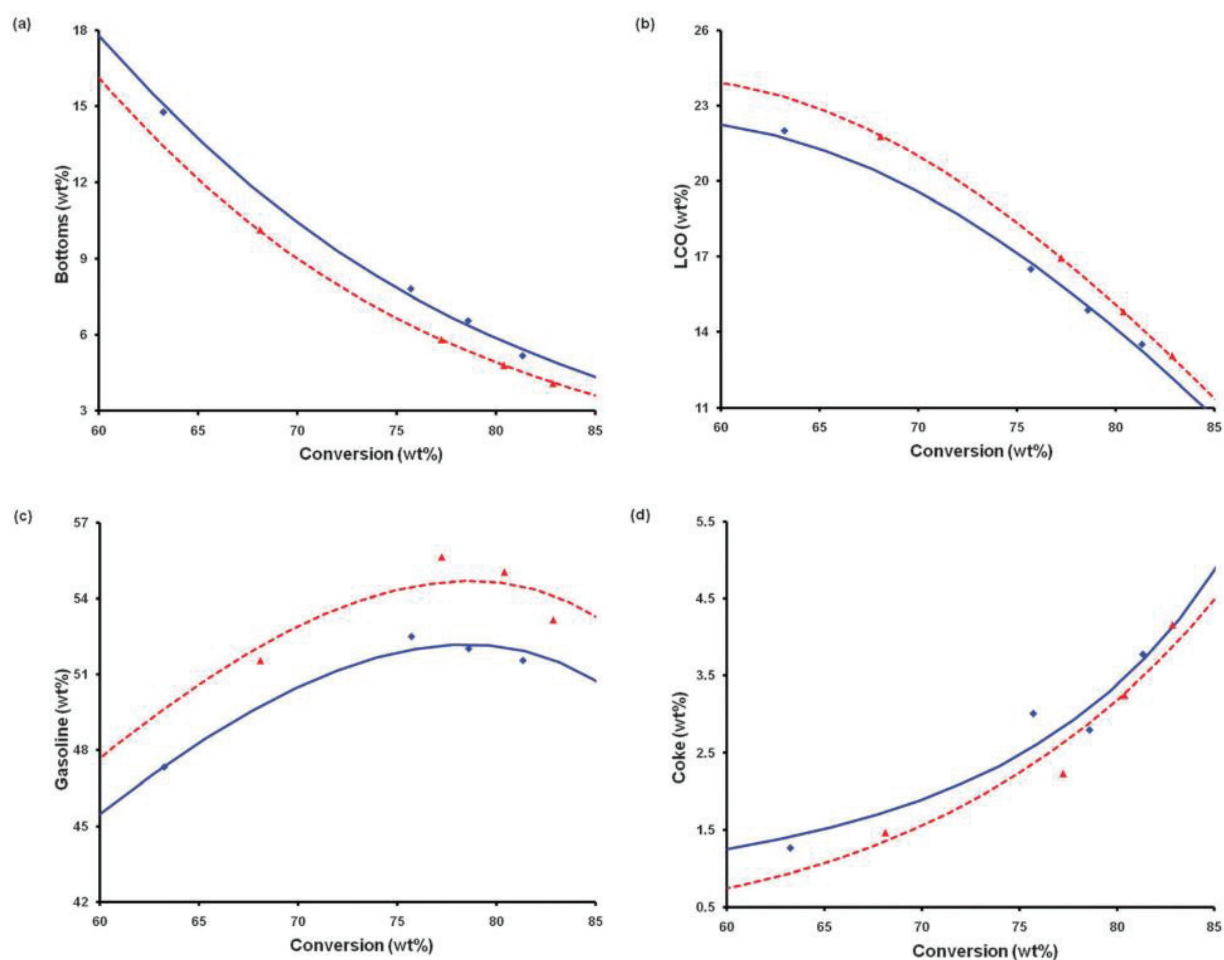


**Figure 19.** VGO cracking in ACE unit at 527°C with conventional zeolite USY (blue diamond) and mesostructured zeolite USY (red triangle). Reproduced from [44].

## 4 Aim of this PhD researches

From the literature, it has been identified that hierarchical zeolites are expected to facilitate the diffusion of large molecules through the catalyst, which should increase the reaction conversion and decrease the coke pore blocking.

Inspired by the work previously reported by Chal et al. [45] and Garcia-Martinez et al. [44], this PhD work deals with the investigation of the effect of hierarchical Y zeolites for the co-processing of bio-oil and vacuum gas oil. The aim of this work is to identify key parameters, such as the proportion of micro/mesopores, the variation of number or type of acid sites, characterizing hierarchical zeolites and their subsequent effect on the Co-FCC.

To achieve this goal, starting from the same Y parent zeolite, we have synthesized a series of hierarchical porous Y zeolite with various contents of mesopores. The porous structure, surface properties, acidity and diffusion were characterized and discussed with results in cracking of a model reaction and real feedstock. More precisely, pseudomorphic treatments published by Chal et al. [45] and Garcia-Martinez et al. [44] have been considered because of the ultra-stabilized Y zeolite they allowed to prepared.

This PhD is composed of five chapters:

- Chapter 1: State of art, which focuses on challenges that co-processing of bio-oil with vacuum gas oil are facing, and the answer that could be given by hierarchical materials.
- Chapter 2: Experiment methods section, which includes the description of the characterization techniques and test benches used during this study.
- Chapter 3: Characterization results of the hierarchical Y zeolites used during the research.
- Chapter 4: Catalytic evaluation of the hierarchical zeolites using model cracking reactions. The catalytic activity of the zeolites is investigated with the n-hexane cracking reaction, with and without addition of butanol in the mixture.
- Chapter 5: Catalytic evaluation of the hierarchical zeolites for the processing of bio-oil and vacuum gas oil in MAT unit.



### References for Chapter I

- [1] European Commission, “2020 climate & energy package.”
- [2] European Climate Foundation, “Roadmap 2050.” [Online]. Available: <https://www.roadmap2050.eu/>.
- [3] “Refinery Flow.” [Online]. Available: <https://en.wikipedia.org/wiki/File:RefineryFlow.png>.
- [4] E. F. Sousa-Aguiar, *Y Zeolites as a Major Component of FCC Catalysts: Main Challenges in the Modification Thereof*. Elsevier B.V., 2016.
- [5] A. De Lasa, H. I.; Dogu, G.; Ravella, *Chemical Reactor Technology for Environmentally Safe Reactors and Products*. 1991.
- [6] J. R. Grace, A. A. Avidan, and T. M. Knowlton, *Circulating Fluidized Beds*. 1997.
- [7] Y. Schuurman, G. Fogassy, and C. Mirodatos, “Tomorrow’s Biofuels: Hybrid Biogasoline by Co-processing in FCC Units,” in *The Role of Catalysis for the Sustainable Production of Bio-Fuels and Bio-Chemicals*, 2013.
- [8] A. Corma and L. Sauvanaud, “FCC testing at bench scale: New units, new processes, new feeds,” *Catal. Today*, vol. 218–219, pp. 107–114, 2013, doi: 10.1016/j.cattod.2013.03.038.
- [9] A. Brait, K. Seshan, H. Weinstabl, A. Ecker, and J. A. Lercher, “Evaluation of commercial FCC catalysts for hydrocarbon conversion II. Time-on-stream behavior of n-hexane conversion and comparison of n-hexane conversion to MAT.”
- [10] F. de Miguel Mercader, M. J. Groeneveld, S. R. A. Kersten, N. W. J. Way, C. J. Schaverien, and J. A. Hogendoorn, “Production of advanced biofuels: Co-processing of upgraded pyrolysis oil in standard refinery units,” *Appl. Catal. B Environ.*, 2010, doi: 10.1016/j.apcatb.2010.01.033.
- [11] C. Lindfors, V. Paasikallio, E. Kuoppala, M. Reinikainen, A. Oasmaa, and Y. Solantausta, “Co-processing of dry bio-oil, catalytic pyrolysis oil, and hydrotreated bio-oil in a micro activity test unit,” *Energy and Fuels*, 2015, doi: 10.1021/acs.energyfuels.5b00339.
- [12] D. Verboekend *et al.*, “Synthesis, characterisation, and catalytic evaluation of hierarchical faujasite zeolites: milestones, challenges, and future directions,” *Chem. Soc. Rev.*, vol. 45, no. 12, pp. 3331–3352, 2016, doi: 10.1039/C5CS00520E.
- [13] K. H. Altgelt, *Composition and Analysis of Heavy Petroleum Fractions*. 1993.
- [14] G. W. Huber, S. Iborra, and A. Corma, “Synthesis of transportation fuels from biomass:



- Chemistry, catalysts, and engineering,” *Chem. Rev.*, vol. 106, no. 9, pp. 4044–4098, 2006, doi: 10.1021/cr068360d.
- [15] R. Venderbosch and W. Prins, “Fast pyrolysis technology development,” *Biofuels, Bioprod. Biorefining*, vol. 4, pp. 178–208, 2010, doi: 10.1002/bbb.
- [16] J. Lehto, A. Oasmaa, Y. Solantausta, M. Kytö, and D. Chiaramonti, “Fuel oil quality and combustion of fast pyrolysis bio-oils,” *VTT Technol.* 87.
- [17] T. M. Huynh, U. Armbruster, and A. Martin, “Perspective on Co-feeding of Phenolic Compounds into Existing Refinery Units,” in *Intech*, 2017.
- [18] M. S. Talmadge *et al.*, “A perspective on oxygenated species in the refinery integration of pyrolysis oil,” *Green Chem.*, vol. 16, no. 2, pp. 407–453, 2014, doi: 10.1039/c3gc41951g.
- [19] A. Corma, G. W. Huber, L. Sauvanaud, and P. O’Connor, “Processing biomass-derived oxygenates in the oil refinery: Catalytic cracking (FCC) reaction pathways and role of catalyst,” *J. Catal.*, vol. 247, no. 2, pp. 307–327, 2007, doi: 10.1016/j.jcat.2007.01.023.
- [20] I. Graça, J. M. Lopes, M. F. Ribeiro, F. Ramôa Ribeiro, H. S. Cerqueira, and M. B. B. de Almeida, “Catalytic cracking in the presence of guaiacol,” *Appl. Catal. B Environ.*, vol. 101, no. 3–4, pp. 613–621, 2011, doi: 10.1016/j.apcatb.2010.11.002.
- [21] A. D. R. Pinho, M. B. B. De Almeida, F. L. Mendes, V. L. Ximenes, and L. C. Casavechia, “Co-processing raw bio-oil and gasoil in an FCC Unit,” *Fuel Process. Technol.*, 2015, doi: 10.1016/j.fuproc.2014.11.008.
- [22] L. Gueudré, “Internal report CNRS.”
- [23] E. T. C. Vogt and B. M. Weckhuysen, “Fluid catalytic cracking: recent developments on the grand old lady of zeolite catalysis,” *Chem. Soc. Rev. Chem. Soc. Rev.*, vol. 7342, no. 44, pp. 7342–7370, 2015, doi: 10.1039/c5cs00376h.
- [24] W. Vermeiren and J. P. Gilson, “Impact of zeolites on the petroleum and petrochemical industry,” *Top. Catal.*, vol. 52, no. 9, pp. 1131–1161, 2009, doi: 10.1007/s11244-009-9271-8.
- [25] G. Fogassy, N. Thegarid, Y. Schuurman, and C. Mirodatos, “From biomass to bio-gasoline by FCC co-processing: Effect of feed composition and catalyst structure on product quality,” *Energy Environ. Sci.*, vol. 4, no. 12, pp. 5068–5076, 2011, doi: 10.1039/c1ee02012a.
- [26] J. Weitkamp, “Zeolites and catalysis,” *Solid State Ionics*, vol. 131, no. 1, pp. 175–188, 2000, doi: 10.1016/S0167-2738(00)00632-9.

- [27] M. Stöcker, "Gas phase catalysis by zeolites," *Microporous Mesoporous Mater.*, vol. 82, no. 3, pp. 257–292, 2005, doi: 10.1016/j.micromeso.2005.01.039.
- [28] The International Zeolite Association (IZA), "Zeolite Database." [Online]. Available: <http://www.iza-structure.org/databases/>.
- [29] Robert M. Milton, "Molecular Sieve Adsorbents, US Patent 2882243," 1959.
- [30] R. M. Milton, "Molecular Sieve Adsorbents, US Patent 2882244," 1959.
- [31] D. W. Breck, W. G. Eversole, R. M. Milton, T. B. Reed, and T. L. Thomas, "Crystalline Zeolites. I. The Properties of a New Synthetic Zeolite, Type A," *J. Am. Chem. Soc.*, vol. 78, no. 23, pp. 5963–5972, 1956, doi: 10.1021/ja01604a001.
- [32] G. V. Research, "Zeolite Market Size, Share & Trends Analysis Report," 2014.
- [33] W. Lutz, "Zeolite Y: Synthesis, modification, and properties - A case revisited," *Adv. Mater. Sci. Eng.*, vol. 2014, 2014, doi: 10.1155/2014/724248.
- [34] A. M. S. Ojuva, "Processing and performance of zeolites for efficient carbon dioxide separation," 2015.
- [35] W. Schwieger *et al.*, "Hierarchy concepts: classification and preparation strategies for zeolite containing materials with hierarchical porosity," *Chem. Soc. Rev.*, vol. 45, no. 12, pp. 3305–3566, 2016, doi: 10.1039/C5CS00599J.
- [36] A. Inayat, I. Knoke, E. Spiecker, and W. Schwieger, "Assemblies of mesoporous FAU-type zeolite nanosheets," *Angew. Chemie - Int. Ed.*, vol. 51, no. 8, pp. 1962–1965, 2012, doi: 10.1002/anie.201105738.
- [37] H. Awala *et al.*, "Template-free nanosized faujasite-type zeolites," *Nat. Mater.*, vol. 14, no. 4, pp. 447–451, 2015, doi: 10.1038/nmat4173.
- [38] D. Verboekend, T. C. Keller, S. Mitchell, and J. Pérez-Ramírez, "Hierarchical FAU- and LTA-Type Zeolites by Post-Synthetic Design: A New Generation of Highly Efficient Base Catalysts," *Adv. Funct. Mater.*, vol. 23, no. 15, pp. 1923–1934, Apr. 2013, doi: 10.1002/adfm.201202320.
- [39] Z. Qin, B. Shen, X. Gao, F. Lin, B. Wang, and C. Xu, "Mesoporous y zeolite with homogeneous aluminum distribution obtained by sequential desilication-dealumination and its performance in the catalytic cracking of cumene and 1,3,5-triisopropylbenzene," *J. Catal.*, vol. 278, no. 2, pp. 266–275, 2011, doi: 10.1016/j.jcat.2010.12.013.

- [40] K. Li, J. Garcia-Martinez, and M. G. Beaver, "Introduction Of Mesoporosity Into Low Silicazeolites," 2013.
- [41] K. P. De Jong *et al.*, "Zeolite  $\gamma$  crystals with trimodal porosity as ideal hydrocracking catalysts," *Angew. Chemie - Int. Ed.*, vol. 49, no. 52, pp. 10074–10078, 2010, doi: 10.1002/anie.201004360.
- [42] J. Y. Ying and J. Garcia-Martinez, "Mesostructured Zeolitic Materials, And Methods Of Making And Using The Same," 2009.
- [43] I. I. Ivanova and E. E. Knyazeva, "Micro-mesoporous materials obtained by zeolite recrystallization: Synthesis, characterization and catalytic applications," *Chem. Soc. Rev.*, vol. 42, no. 9, pp. 3671–3688, 2013, doi: 10.1039/c2cs35341e.
- [44] J. Garcia-Martinez, M. Johnson, J. Valla, K. Li, and J. Y. Ying, "Mesostructured zeolite Y—high hydrothermal stability and superior FCC catalytic performance," *Catal. Sci. Technol. Catal. Sci. Technol.*, vol. 2, no. 2, pp. 987–994, 2012, doi: 10.1039/c2cy00309k.
- [45] R. Chal, T. Cacciaguerra, S. van Donk, and C. Gérardin, "Pseudomorphic synthesis of mesoporous zeolite Y crystals," *Chem. Commun.*, vol. 46, no. 41, p. 7840, 2010, doi: 10.1039/c0cc02073g.
- [46] M. Milina, S. Mitchell, and J. Pérez-Ramírez, "Prospectives for bio-oil upgrading via esterification over zeolite catalysts," *Catal. Today*, vol. 235, pp. 176–183, 2014, doi: 10.1016/j.cattod.2014.02.047.
- [47] A. Osatiashtiani *et al.*, "On the influence of Si:Al ratio and hierarchical porosity of FAU zeolites in solid acid catalysed esterification pretreatment of bio-oil," *Biomass Convers. Biorefinery*, vol. 7, no. 3, pp. 331–342, 2017, doi: 10.1007/s13399-017-0254-x.

# Chapter II: Experimental methods

---

## 1. Characterization techniques

### 1.1 Elementary analysis: ICP-OES technique

Elementary composition of the zeolite is determined by Inductively Coupled Plasma - Optical Emission Spectrometry (ICP-OES). The apparatus available at the IRCELYON is a Horiba Jobin Yvon ICP-OES. This analytical tool is based on the detection of emitted radiation from atoms and ions that have been excited. Each radiation corresponds to a specific chemical element, with proportional relationship between the intensity of the radiation and the concentration of the chemical element [1]. This technique is particularly useful to quantify Si, Al and Na proportion within the zeolites.

Prior to the measurements, solid samples, as zeolites, require to be solubilized:

- For the Al and Na detections, the samples are prepared by acid digestion. The powder is mixed with  $\text{H}_2\text{SO}_4$ ,  $\text{HNO}_3$ , HF into a Becher, then evaporated and mixed with  $\text{HNO}_3$ .
- For Si detection, fusion with lithium borate is used: the samples are heated with  $\text{Li}_2\text{B}_4\text{O}_7$  in Pt-Au crucible up to  $1100^\circ\text{C}$ , then mixed with HCl.

During the analysis, the sample solutions are converted to an aerosol with a nebulizer and directed to the plasma created by the ICP torch. The temperature reached at this point can be up to  $8000^\circ\text{C}$ , leading to efficient atomization, ionization and excitation. At this excited state, the species may relax to ground state via emission of a photon. For each photon, which has a characteristic energy, a wavelength corresponds. The wavelengths are characteristic of the elements from which the photons come from. This correspondence is resumed in Table 1 for the chemical element considered for our researches.

**Table 1.** Wavelengths used for the silica, aluminum and sodium quantification

Elements	Si	Al	Na
Wavelength (nm)	212.41	309.3	589.6
	251.61	396.15	
	252.85		

### 1.2 X-Ray Diffraction (XRD)

#### 1.2.1 Description of the technique

X-Ray Diffraction (XRD) is a non-destructive technique to study crystalline materials. It provides information about phase composition, crystallinity and cell parameters of our materials. X-Ray Diffraction patterns are recorded on a Bruker D8 advance diffractometer using  $\text{CuK}_{\alpha 1}$  radiation at  $\lambda=1.5406 \text{ \AA}$ . Samples are prepared by grinding, then are top loaded on a plastic sample holder. X-ray diffractograms are recorded over the  $2\theta$  angle range of  $4\text{-}80^\circ$ , with steps of  $0.02^\circ$ . When necessary, such as for hierarchical materials, characterization in low  $2\theta$  angle range of  $0.45\text{-}7^\circ$  with steps of  $0.01^\circ$ , is also performed.

#### 1.2.2 Theory

For our purpose, XRD is used to confirm the faujasite Y structure of our materials. This zeolite crystallizes according to the face-centred cubic system. The axial lengths and interaxial angles of this unit cell are  $a=b=c$  – also referred as  $a_0$  – and  $\alpha=\beta=\gamma=90^\circ$ , respectively. The interplanar spacing  $d$  between the two closest parallel planes follow the equation:

$$d = \frac{a_0}{\sqrt{h^2 + k^2 + l^2}} \quad (1)$$

Where  $h, k, l$  are the Miller indices. For face-centred cubic lattice, the reflexion is allowed when these indices are either all even or all odd.

During X-ray diffraction measurements, a beam of X-ray strikes the sample, which diffracts the X-ray beam. When the reflected wave patterns coming from two atoms belonging to two parallel planes are in phase, a resultant wave with a higher amplitude is detected by the detector. It is called constructive interference [Figure 1.].

This occurs when:

- The radiation is scattered with an angle equal to the angle of incidence
- And the difference of the path lengths is equal to an integer number of the wavelength.

This is known as Bragg's law:

$$2d \sin \theta = n\lambda \quad (2)$$

Where  $\theta$  is the scattering angle,  $n$  is an integer number.

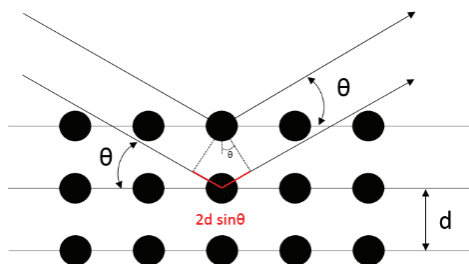


**Figure 1.** Difference of path lengths for two beams that are scattered by two different atoms.

The intensity of the wave patterns recorded by the detector as a function of the angle  $2\theta$  is characteristic of the investigated material. Each peak present on the pattern is due to the diffraction of a (hkl) plan. The patterns from materials characterized by this technique, as well as some theoretically calculated patterns, are compiled in a database by International Centre for Diffraction Data [2].

In this thesis, the XRD analysis is used for the following cases:

- Phase composition

The XRD patterns of the studied samples are compared to XRD patterns of Y zeolite compiled in ICDD database. Based on PDF 01-073-2312, no other phase than faujasite zeolite has been detected.

- Crystallinity

Once the crystalline structure is confirmed, the relative crystallinity of the synthesized materials is calculated by comparing the peak intensity to the parent material. Following the ASTM D3906 standard method, the eight peaks considered for the calculation of the peak intensity were (331), (511), (440), (533), (642), (822), (555) and (664) [3].

- Si/Al ratio and unit cell size

The silica to aluminium ratio within zeolite structure affects the unit cell size  $a_0$  in the crystal. A slight difference of  $a_0$  modifies the d-spacing value [equation (1)]. Thus, the  $\theta$  angle fulfilling Bragg's law and the XRD pattern are changed. Two zeolites, which crystallize according to the same structure with different Si/Al ratios, exhibit a small shift between their diffraction peaks. Relation between the framework Si/Al ratio of the zeolite and its unit cell size have led to correlation studies.

Fichtner-Schmittler et al. have reported an empirical equation between the unit cell constant  $a_0$  and the number of aluminium atoms  $N_{Al}$  [4]:

$$N_{Al} = 112.4 (a_0 - 24.233) \quad (3)$$

This empirical equation is based on 17 synthetic  $NH_4Y$  zeolites having  $N_{Al} < 52$ . The Si/Al ratios of these materials were determined by NMR, IR and chemical analysis [2][3], and then correlated to the  $a_0$  values obtained by XRD.

Since there is a total of 192 silica and aluminium atoms in faujasite zeolite:

$$N_{Si} + N_{Al} = 192 \quad (4)$$

Where  $N_{Si}$  is the number of silica atoms.

Hence, Fichtner-Schmittler equation is valid for zeolite with Si/Al  $> 2.7$  and the following equation was obtained:

$$\frac{Si}{Al} = \frac{192 \times 0,00890}{a_0 - 24,233} - 1 \quad (5)$$

Other research groups, like Breck & Flanigan [7], Kerr et al., Dempsey et al. or Sohn et al. [8], have also published similar equation for Si/Al calculation. However, considering the range of validity, the equation obtained by Fichtner-Schmittler have been chosen for Si/Al calculation by XRD.

### 1.3 Nitrogen adsorption-desorption isotherms

Gas adsorption is a powerful technique for the characterisation of porous materials. At the institute, the measurements are performed on a BELSORP-mini apparatus from BEL Japan, Inc. On this apparatus, the determination of physisorption isotherm is performed via a manometric method:

- A known amount of pure gas is admitted into a calibrated volume containing the sample, which is maintained at 77K by liquid nitrogen.
- As adsorption takes place, the pressure in the confined sample cell decreases until it reaches an equilibrium. The amount of gas adsorbed is calculated by difference of the amount of gas initially admitted and the amount of gas required to fill the dead volume at the equilibrium pressure.
- Admission of successive charges of gas to the sample cell allows the point-by-point construction of the adsorption isotherm.

- Following the complete adsorption isotherm measurement, desorption isotherm is similarly constructed by successive removal of known amount of gas.

Prior to the measurement, around 50mg of the samples are degassed for one night at 250°C in order to remove any adsorbate – like water – from the adsorbent. Adsorption-desorption isotherms are displayed in graphical form with the amount adsorbed (in moles per gram of outgassed adsorbent) as a function of the equilibrium relative pressure  $p/p^0$ , where  $p^0$  is the saturation pressure of nitrogen at 77K [9].

From these N<sub>2</sub> adsorption-desorption isotherms, the following characterisations are obtained:

- Apparent surface area

The BET method, introduced in 1938 by Brunauer-Emmett-Teller [10], is used to determine the surface area of our samples. The equation that they developed enable the determination of the monolayer volume of adsorbed nitrogen, from which the apparent surface area of the adsorbent is calculated. Because of deviation from the linear line at high pressure range, the BET plot was applied in relative pressure range  $p/p^0 < 0.1$ . A detailed description of calculation is available in Appendix I.

- Microporous volume

Considering the lack of validity of t-plot method for the estimation of microporous volume in hierarchical materials [11], this volume is determined from the volume of adsorbed nitrogen when the slope of the adsorption branch becomes lower than 1000cm<sup>3</sup>.g<sup>-1</sup>. The N<sub>2</sub> isotherm graph displays the adsorbed volume of gaseous N<sub>2</sub> ( $V_{ads}$  in cm<sup>3</sup>(STP).g<sup>-1</sup>) as a function of the relative pressure  $p/p_0$ . To obtain the microporous volume of the catalyst ( $V_{micropores}$ ), the volume of gaseous nitrogen  $V_{ads}$  is converted into the corresponding volume of nitrogen at liquid state:

$$V_{micropores} = V_{ads} \times D \quad (6)$$

$$D = \frac{\rho_{N_2(gas)}}{\rho_{N_2(liq)}} = \frac{M_{N_2}}{V_m(STP) \times \rho_{N_2(liq)}} \quad (7)$$

Where: D is the ratio of the density of N<sub>2</sub> at gas state ( $\rho_{N_2,gas}$ ) over the density of N<sub>2</sub> at liquid state ( $\rho_{N_2,liq}$ ).

$M_{N_2}$  is the molecular weight of nitrogen [g.mol<sup>-1</sup>]

$V_m$  (STP) is the molar volume of gaseous N<sub>2</sub> at standard temperature and pressure conditions [cm<sup>3</sup>.mol<sup>-1</sup>]



After calculation, the value of the coefficient  $D$  is  $1.55\text{E-}03$ . The calculation for the microporous volume of H-USY-0 sample is displayed in Appendix II.

- Total pore volume:

The total pore volume is estimated from the nitrogen desorption branch at  $p/p^0=0.9$ . At this relative pressure, we consider that nitrogen fills exclusively the intra-particle porosity. At higher relative pressure, the nitrogen could be adsorbed into inter-particle mesoporosity. The total pore volume is calculated from the adsorbed volume of gaseous nitrogen  $V_{\text{ads}}$  with equation 6 and 7.

### 1.4 Transmission Electronic Microscopy (TEM)

TEM images of the zeolites are obtained on a JEOL 2010 microscope. A  $\text{LaB}_6$  single crystal is used as an electron source and the apparatus is operating at 200kV. To prepare the sample for the analysis, the zeolites is ground, mixed to anhydride ethanol, dropped onto a carbon coated copper grid, and then put under a heating lamp in order to evaporate the ethanol. In this way, a thin layer of sample, without stacking of crystals, is obtained.

The zeolite samples have crystals diameters in the order of a micrometre. With low magnification ( $\times 6\text{--}8\text{k}$ ) it is possible to observe an entire crystal of the zeolite. At higher magnification ( $< \times 25\text{k}$ ) more details about lattice fringes and the presence of mesopores are obtained.

### 1.5 Solid-state $^{27}\text{Al}$ and $^{29}\text{Si}$ Nuclear Magnetic Resonance (NMR)

#### 1.5.1 Experimental parameters

Solid-state NMR are useful analysis for understanding the close surroundings of the atoms. The results are obtained using a Bruker Avance III 500WB spectrometer at 11.7T. The samples are packed into a 4mm-diameter zirconia rotor.  $\text{Al}(\text{NO}_3)_3$  and Q8M8 are the standard references for the measurements carried out. Pulse lengths of 0.5 and 4  $\mu\text{s}$  and recycle delay of 1 and 100 s, respectively, are used for  $^{27}\text{Al}$  and  $^{29}\text{Si}$  signals.

#### 1.5.2 Solid-state $^{29}\text{Si}$ NMR

Zeolites are built from  $\text{SiO}_4$  and  $\text{AlO}_4$  tetrahedral. The  $^{29}\text{Si}$  NMR spectrum of such materials displays a series of peaks which correspond to the number of  $\text{AlO}_4$  connected to the silicon via an oxygen atom. The position of these peaks is shown on [Figure 2].

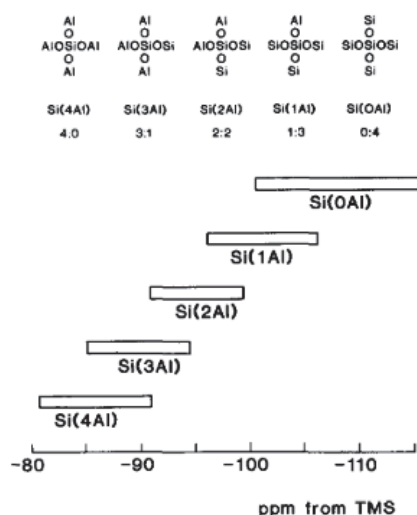


**Figure 2.** Ranges of  $^{29}\text{Si}$  chemical shift for  $\text{Si}(n\text{Al})$  building blocks in framework aluminosilicates [12].

In the case of spectrum containing more than one signal, it is possible to determine the composition of the aluminosilicate framework. The surface areas of the peaks are proportional to the quantity of  $\text{Si}(n\text{Al})$  building blocks present within the framework. Thus, the framework Si/Al ratio is calculated from:

$$\frac{\text{Si}}{\text{Al}} = \frac{\sum_{n=0}^4 I_{\text{Si}(n\text{Al})}}{\sum_{n=0}^4 \frac{n}{4} I_{\text{Si}(n\text{Al})}}$$

Where  $I_{\text{Si}(n\text{Al})}$  is the surface area of the NMR signal corresponding to the  $\text{Si}(n\text{Al})$  peak. This calculation is valid if there is not Al-O-Al bonds in the framework.

### 1.5.3 Solid-state $^{27}\text{Al}$ NMR

The solid-state  $^{27}\text{Al}$  NMR gives further information about coordination of aluminium atoms in the zeolites. Aluminium can either contribute to the framework or be considered as extra framework species. Framework aluminium (FAL) are tetracoordinated ( $\text{Al}^{\text{IV}}$ ) whereas extra framework aluminium (EFAL) can be penta- ( $\text{Al}^{\text{V}}$ ) or hexacoordinated ( $\text{Al}^{\text{VI}}$ ). These three peaks are observable at 60ppm, 30ppm and 0ppm, respectively [12].

## 2. Catalytic microactivity test unit (MAT)

### 2.1 Description of the unit

The catalytic microactivity test unit (MAT) is a laboratory test bench that is used to analyse the catalytic activity of fluid catalytic cracking (FCC) catalysts. It has been designed for executing up to four consecutive FCC tests. The operator can set independent experimental parameters for each experiment.

This lab-scale test bench works with a fixed-bed quartz reactor, containing powder catalyst on a porous plate. A pre-defined mass of feedstock is injected at the top of the reactor and the reaction products are retrieved at the bottom [Figure 3.]. The tests are performed for several catalyst-to-oil ratios (Cat/Oil). Each FCC test is divided into 4 stages:

- “Preparation”: the furnace temperatures reach the set points and the reactor is flushed with nitrogen flow.
- “Reaction”: introduction of the feedstock within the reactor.
- “Stripping”: a nitrogen flow carries the reaction products from the reactor bed through the process lines.
- “Regeneration”: an air flow is used to regenerate the catalyst through oxidation of the coke to CO<sub>2</sub>.

The gas flows are regulated by the mass flow controllers with a top-capacity of 100 mL.min<sup>-1</sup>.

Two feedstocks, controlled by their own pump system, can be injected simultaneously into the reactor. In fact, the initial injection system composed of a HPLC pump (for VGO), has been completed by a syringe pump dedicated to the injection of an additional feedstock (for bio-oil). The process lines of the two feedstocks converge to a “T” union fitting, upstream of the 4-way valve that controls the choice of the reactor inlet. Heating cables are placed around the two feedstock containers, the 1/8” and 1/16” pipes to reduce the viscosity of the feedstock, allowing a smooth flow.

Downstream of the reactor, a 6-way valve sends the reaction products into the collection and sampling system. Condensable products are collected in glass tubes and gases are diverted into a burette. The glass tubes are kept cold by a chiller system. Four glass tubes are assigned to the four independent and consecutive FCC tests. The gases displace the water initially contained and four level sensors control the drop of liquid, into the burette. During the regeneration step, the 6-way valve sends the gas flow to the CO<sub>2</sub> quantification part of the unit. Upstream the CO<sub>2</sub> infrared detector, a second reactor converts potential CO from coke combustion into CO<sub>2</sub>.

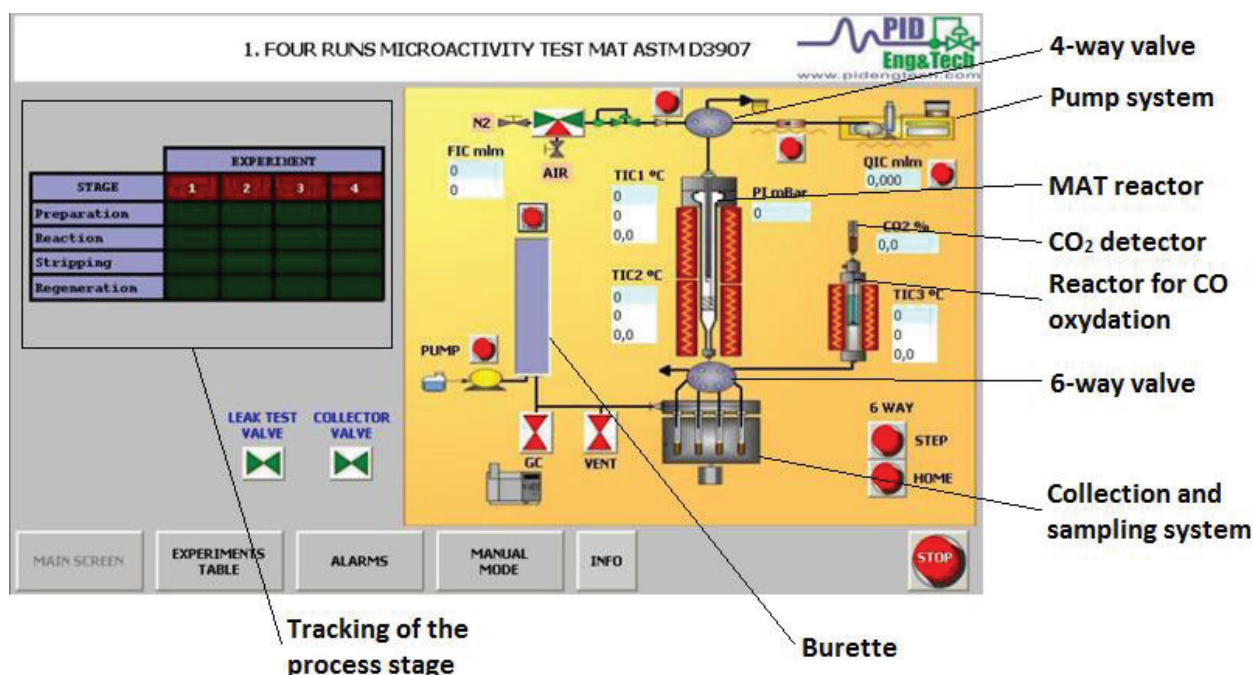


Figure 3. Control screen of the micro activity test unit representing the different part of the process.

## 2.2 Description of the analytical setup

### 2.2.1 Compact GC

Chromatography of the gases collected in the burette is carried out after each experiment. A compact gas chromatographer (GC) with three columns is connected to the test bench. A molsieve 5A and an Rt-U-BOND columns with a thermal conductivity detector enable the quantification of H<sub>2</sub>, O<sub>2</sub>, N<sub>2</sub>, CH<sub>4</sub>, CO and CO<sub>2</sub>, C<sub>2</sub> hydrocarbons, respectively. An Rt-Alumina PLOT column deactivated by Na<sub>2</sub>SO<sub>4</sub> is associated to a flame ionization detector for the analysis of hydrocarbons up to C<sub>6</sub>.

### 2.2.2 Simulated distillation SIMDIS

Simulated distillation (SIMDIS) of the liquid products condensed in the collection and sampling system completes the analytical setup associated to the MAT unit. The liquid samples are injected into a gas chromatographer that separates the components according to their boiling points. Hence, the following cracking fractions are identified:

- Light cracked naphtha (LCN): C<sub>5</sub>-90°C
- Medium cracked naphtha (MCN): 90-140°C
- Heavy cracked naphtha (HCN): 140-221°C
- Light cycle oil (LCO): 221-360°C
- Decanted oil (DO): > 360°C

### 2.2.3 Mass balance

To establish the mass balance it is necessary to compare the mass of reactant and the mass of products obtained from the cracking reactions. The mass of feedstock initially injected in the reactor ( $m_{\text{injected feedstock}}$ ) is known from the setup of the inlet pump system. Regarding the cracking products, three distinct families are considered: the gas fraction, the liquid fraction and the coke. The mass of gas products is available from a calculation involving the molar proportion of each gas product ( $\%molar_{\text{gas},i}$  obtained from GC), the number of moles within the gas fraction ( $n_{\text{gas,tot}}$  obtained from the burette volume) and the molecular weight of the considered compounds ( $M_{\text{gas},i}$ ):

$$m_{\text{gas products}} = \sum_i \frac{\%molar_{\text{gas},i} \times n_{\text{gas,tot}} \times M_{\text{gas},i}}{100} \quad (8)$$

Regarding the liquid products, the weighting of the sampling system before and after the experiment gives the amount of liquid produced. The mass of coke formed on the catalyst is calculated from the moles of  $\text{CO}_2$  formed during its combustion and the molecular weight of the coke, which is mainly composed of carbon atoms.

The mass balance calculated from the comparison between the mass of feedstock injected and the mass of cracking products is often far lower than 100% (between 60 and 80%). The main reason of this deviation from a 100% mass balance is the quantity of liquid products that gets stuck to the pipe of the collection and sampling system (see Figure 3). Since the proportion of products that is not recovered from the collection and sampling system is higher for the experiments performed at high cat/oil ratio than the ones performed at lower, the mass balance is fluctuating. Hence, a correction is applied for all the MAT results, where the mass of liquid is determined as:

$$m_{\text{liquid products, corrected}} = m_{\text{injected feedstock}} - m_{\text{gas products}} - m_{\text{coke}} \quad (9)$$

This consideration gives a fictive mass balance of 100% for all experiments and allows to compare the results obtained at different cat/oil ratios or with various catalysts.

### 2.2.4 $^{31}\text{P}$ NMR

$^{31}\text{P}$  NMR technique is used for the characterization and quantification of the OH groups within the liquid cracking products. A method based on the functionalisation of the hydroxyl functional groups by a phosphorous reagent, followed by their quantification via  $^{31}\text{P}$  NMR, provides quantitative information on the content of this OH groups. To perform the measurements, approximately 30mg of sample was mixed with 100  $\mu\text{L}$  of  $\text{CDCl}_3$ /pyridine (1:1, v/v) to which 100  $\mu\text{L}$  of an internal standard solution, consisting of cyclohexanol in pyridine at  $0.16 \text{ mol.L}^{-1}$ , is added. The sample solution is mixed with a solution of 100  $\mu\text{L}$  of phosphorylation reagent (2-chloro-4,4,5,5-tetramethyl-1,3,2-

dioxaphospholane, TMDP, Aldrich) in 200  $\mu\text{L}$  of  $\text{CDCl}_3$ , then the mixture is analyzed in a Bruker Avance III 400 MHz spectrometer.

The phosphitylation of the various hydroxyl group by TMDP lead to different chemical shifts that are summarized in Figure 4. Quantitative information about the alkylphenol derivatives (ArOH), alcohols (ROH) and acids (RCOOH) content are obtained by integration of the peak signals within the 137.3-144.7 ppm, 145.5-150.0 ppm and 133.6-136.6 ppm domains, respectively. For the water content, the Karl-Fisher titration method is recommended.

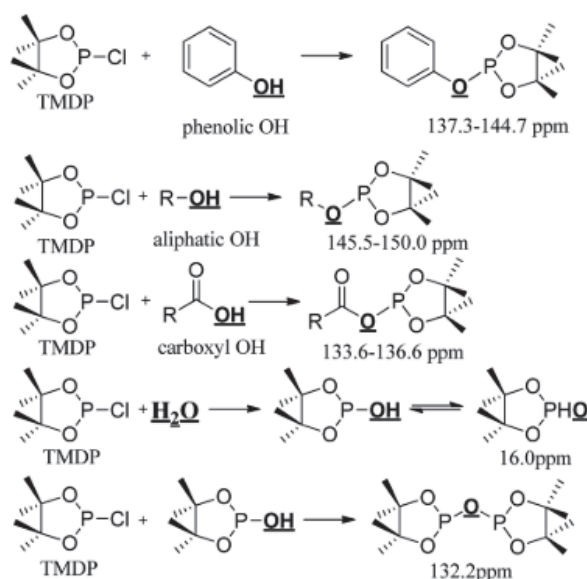


**Figure 4.** Reactions of the phosphorous reagent (TMDP) with various hydroxyl functional groups and the  $^{31}\text{P}$  NMR assignment of phosphitylated compounds. Reproduced from [13].

### 2.2.5 2D-GC analysis

In order to complete the routine analyses previously presented, some of the liquid products are analysed in the GCxGC setup. This setup is built from an Agilent GC 6890N with a cryogenic modulator from Zoex Corporation. The set of columns installed is a reverse mode proposed for the analysis of phenol and oxygenates in coal derived liquids [14]. This installation is equipped with two detectors in parallel, an FID and a quadrupole MS detector. The raw signal is a time-ordered series of second dimension chromatograms and it is transferred to GC Image™ software with the value of the modulation period, which constructs a two dimensional chromatogram by placing the two chromatograms side by side. Identification is accomplished by cross referencing the measured mass spectra to the spectra in the available MS libraries. Semi-quantitative analysis are carried out with FID detector by integration of the various families of identified compounds [15].

### 2.3 Experimental parameters

The feedstocks used for the microactivity test are:

- Vacuum gas oil (VGO) provided by Repsol, as a feedstock from a fossil source.
- Partially deoxygenated bio-oil (PDO) prepared by BTG, as a feedstock from a renewable source.

The densities of the VGO and PDO are used for the settings of the pump systems. Catalyst-to-oil ratios in the range of 0.5-2 are set up for the investigation of the catalytic performances of the zeolites.

The microactivity tests are carried out at 560°C with a reaction time of 30 sec. The stripping is performed for 15 min with a nitrogen flow of 100 ml.min<sup>-1</sup>. The regeneration step is performed at 550°C for 90 min.

### 3. Cracking of model molecules

A specific test bench has been built in order to evaluate the catalytic performances of the catalysts. The construction of this new test bench was necessary in order to:

- Perform catalytic tests with either one or two molecules as reactant.
- Obtain a limited range of cracking products in order to make the interpretation of the results easier.

#### 3.1 Description of the test bench

Since we are dealing with liquid state reactants at ambient temperature, a Coriolis mass flow meter (MFM) is used to regulate the reactant flow into the cracking unit. Upstream the Coriolis MFM, the reactant is stored under 2-bar nitrogen pressure in a 150mL-stainless tank. An additional syringe-pump system with a capacity of 7mL is installed in order to inject simultaneously a second reactant into the unit.

An evaporator, contained inside a hot box, vaporizes the reactant. Then, the gas-state reactant is diluted with a nitrogen flow. Downstream the evaporator, a 6-way valve directs the reactant flow either through the reactor or the microGC.

The catalytic reactions are performed in a 24cm-length U shaped quartz reactor (6mm OD and 4mm ID) heated by a furnace. The short length between the hot box and the furnace avoids condensation of the reactant and the products. The outlet of the reactor, which is also connected to the 6-way valve, is directed either to the microGC or the vent. When the reactant is by-passing the reactor to reach the analytical tool, the design of the unit enables injection of pure nitrogen and air flows through the reactor. This is used to inert the inside of the reactor before a test or regenerate the catalyst afterwards. Heating cables keep the 1/8" pipes going from the hotbox to the microGC and

the vent at 100°C. Two pressure sensors, one upstream and one downstream the reactor, control the pressure drop due to the catalytic bed. The mass flow controllers, the 6-way valves position, the hot box and the furnace temperatures are controlled with a home-made software.

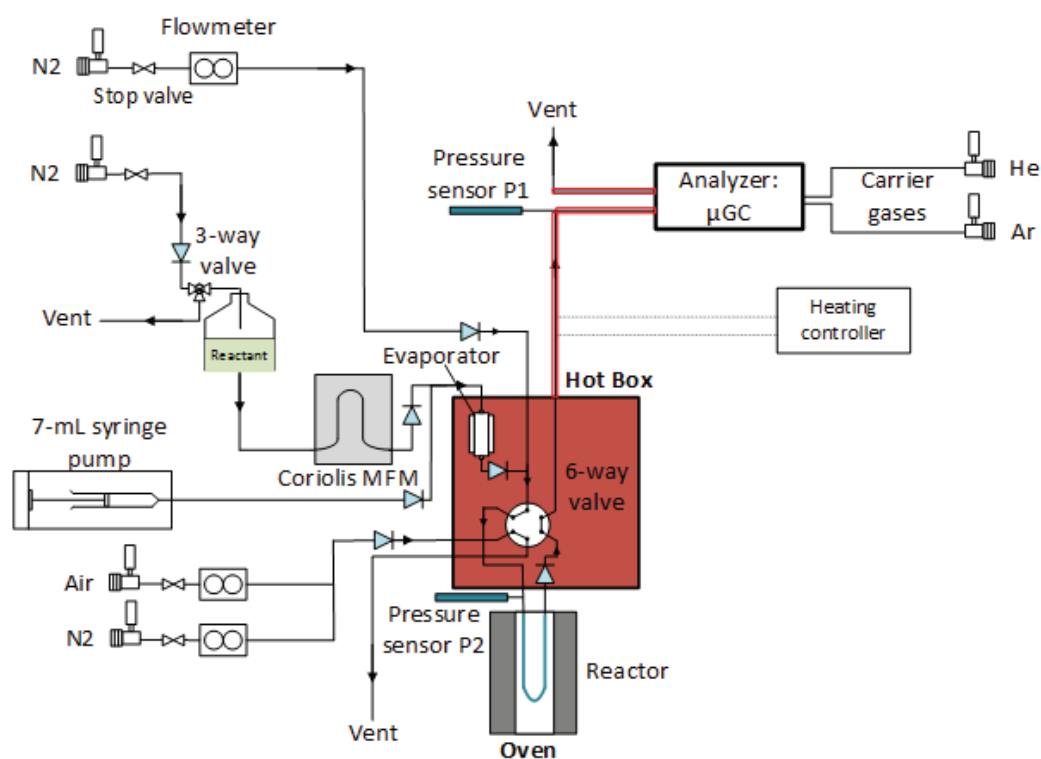


**Figure 5.** Schematic layout of the experimental test bench

### 3.2 Description of the analytical setup

The cracking products are analysed on a microGC from SRA Instrument containing 3 columns:

- A Molsieve 5A column with TCD and Ar carrier gas for He, H<sub>2</sub>, O<sub>2</sub>, N<sub>2</sub>, CH<sub>4</sub> and CO detection.
- A PoraPLOT Q column with TCD and He carrier gas for CO<sub>2</sub>, C<sub>2</sub> and C<sub>3</sub> detection.
- A OV-1 column with TCP and He carrier gas for C<sub>4</sub>, C<sub>5</sub> and C<sub>6</sub> detection.

### 3.3 Selected model molecules

For our purpose catalytic cracking of n-hexane and 2-butanol are carried out. The cracking of n-hexane, commonly referred to as the alpha test, was developed at Mobil laboratories to study the catalytic acidity of zeolites [16]. The limited scale of cracking products, which are in the range of detection of the microGC, makes possible the study of this reaction. The cracking of n-hexane with 2-butanol is carried out in order to investigate the effect of the reaction products from an oxygenated



molecule, like water, on the catalytic performance and selectivity of the catalyst by comparison with pure hydrocarbon.

### 4. FT-IR spectroscopy of pyridine adsorption on acid material

Infrared study of pyridine adsorbed on acidic solids is a powerful tool for the characterisation of the acidity. Spectrum of pyridine coordinately bonded to the surface of the materials differs from the one of pyridinium ion. Thus, it is possible to discriminate and quantify the type of acid sites for the studied solids [17], [18].

#### 4.1 Description of the test bench

Adsorption and desorption of pyridine are performed under vacuum. Since pyridine easily disperses and stick to the grease, it required a construction of a specific vacuum ramp exclusively dedicated to this purpose. For this project, the design and the manufacture of the ramp have been established in collaboration with Verre Equipement and the institute's workshop.

A vacuum pumping group composed of one rotatory pump (①, Figure 5) and one oil diffusion pump (②) creates a high vacuum up to  $2.0\text{E-}06$  mbar into the system. Three Rotulex™ connections (③) enable to connect the liquid-probe reservoir and IR sample cell (④) to the system. All valves, except the one on the IR sample cell, are grease-free in order to limit pyridine adsorption on the glassware. The Edwards Pirani (⑤) and active inverted magnetron (⑥) gauges monitor the residual gas pressure in the range of  $10^3\text{-}10^{-4}$  mbar and  $10^{-2}\text{-}10^{-9}$  mbar, respectively. The IR sample cell has two distinct parts, connected together by conical ground joint. The first part has a Rotulex™ connection for the junction with the vacuum ramp and  $\text{CaF}_2$  windows for the IR measurements. The other part is a glass tube that is placed in the furnace (⑦) for the desorption steps. A Pyrex sample holder is used to move the sample inside the IR cell. The furnace, controlled by a WEST temperature controller, enables to heat of the end part of the IR sample cell up to  $450^\circ\text{C}$ .

The IR spectra are collected using a Nicolet Magna-550 FTIR instrument controlled by the Nicolet OMNIC software. The IR sample cell is disconnected from the vacuum ramp for each IR measurement.



**Figure 6.** Picture of the vacuum ramp built for the characterization of acidity by use of pyridine as a probe molecule. Legend: ① Rotatory pump; ② Oil diffusion pump; ③ Rotulex™ connections; ④ IR sample cell; ⑤ Pirani gauges; ⑥ Active inverted magnetron gauge; ⑦ Furnace; ⑧ Liquid nitrogen trap; ⑨ Electrovalves security system.

### 4.2 Experimental protocol

- Sample preparation

Zeolites are crushed, and then pressed into a self-supported wafer under 2-tons weight. Around 15-20mg of powder is used with a 14-mm diameter die. Once a thin wafer is obtained, it is placed on a sample holder made of Pyrex, containing a 14mm-diameter opening with a 2mm sill around the edge. A 14mm-diameter glass ring hold the wafer in place.

- Background measurement and first desorption

Vacuum is created inside the empty IR cell in order to record a background spectrum for the next measurements. Then, the sample holder containing the wafer is put inside the IR cell and connected to the vacuum ramp for a first desorption step at 450°C over a night. Afterwards, when the temperature of the sample cell drops to ambient temperature, an IR spectrum of the wafer rid of any adsorbed species is recorded.

- Adsorption and desorption of pyridine

The pyridine is frozen, degassed and thawed in order to remove any dissolved gases. Adsorption of pyridine on the wafer is performed at room temperature for 15 min. Desorption of the pyridine is performed at 150°C (for 2h), 250°C (1h), 350°C (1h) and 450°C (1h). Each desorption steps is followed by an IR analyse of the wafer at ambient temperature.

### 4.3 Analysis of IR spectra

Two mains regions of the IR spectra of the zeolites are analysed. The first region to be considered is in the range of 3800-3300  $\text{cm}^{-1}$ , corresponding to the hydroxyl groups. Figure 7 displays an example of IR spectra of two Y zeolites recorded by Daniell et al. [19].

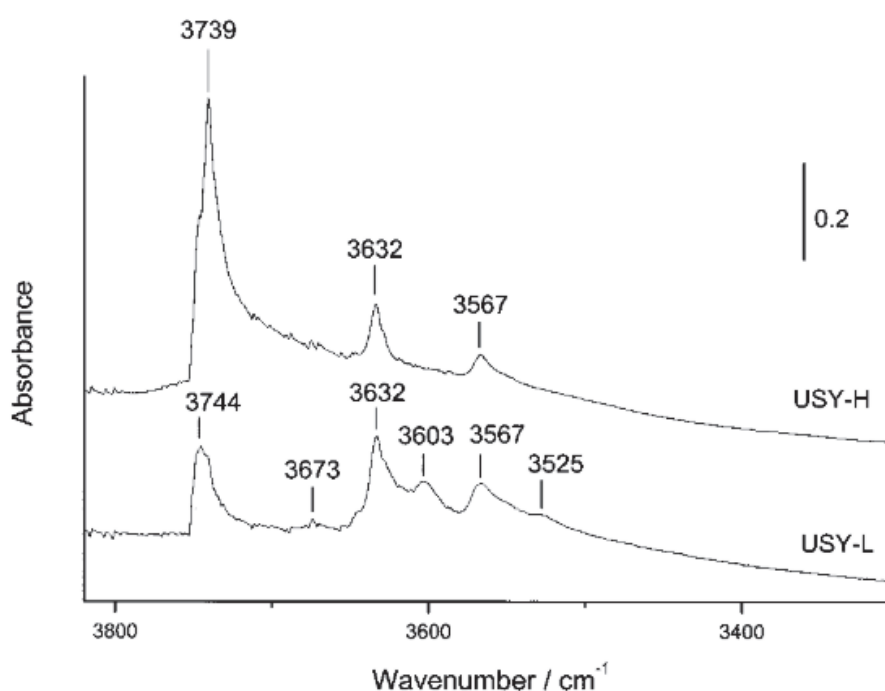


**Figure 7.** Comparison of OH stretching regions of two faujasite zeolite after pretreatment under vacuum at 350°C for 16h. USY-H corresponds to CBV760 (Si/Al=30) and USY-L corresponds to CBV712 (Si/Al=6). Reproduced from [19].

The most intense peak at 3744 $\text{cm}^{-1}$  is assigned to terminal silanol group  $\equiv\text{Si}(\text{O}-\text{H})$  that are on the external surface of the crystals. Bridging hydroxyl groups  $\equiv\text{Si}(\text{O}-\text{H})-\text{Al}\equiv$ , corresponding to the Brønsted-type acid sites, are observed at 3632 and 3567 $\text{cm}^{-1}$ . They are assigned to the protons pointing into the supercages and the sodalite cages, respectively. Some associated bands, corresponding to these hydroxyl groups perturbed by extra framework phase, can be observed at 3603 $\text{cm}^{-1}$  and 3525 $\text{cm}^{-1}$ . A less intense band at 3673 $\text{cm}^{-1}$  is attributed to hydroxyl groups present on

extra framework phase. The assignments of the adsorption bands that are observed in this hydroxyl region are listed in Table 2.

**Table 2.** Assignment of the vibration bands observed in the range of 4000-3300  $\text{cm}^{-1}$

Wavenumber ( $\text{cm}^{-1}$ )	Adsorbed species	References
3744	Terminal silanol $\equiv\text{Si}(\text{O}-\text{H})$	[8][20]
3673	Hydroxyl group on extra framework species	[19]
3632	Bridging hydroxyl groups $\equiv\text{Si}(\text{O}-\text{H})-\text{Al}\equiv$ pointing in supercages	[21]
3567	Bridging hydroxyl groups $\equiv\text{Si}(\text{O}-\text{H})-\text{Al}\equiv$ pointing sodalite cages	[21]
3603; 3525	Bridging hydroxyl groups interacting with extraframework species	[19]

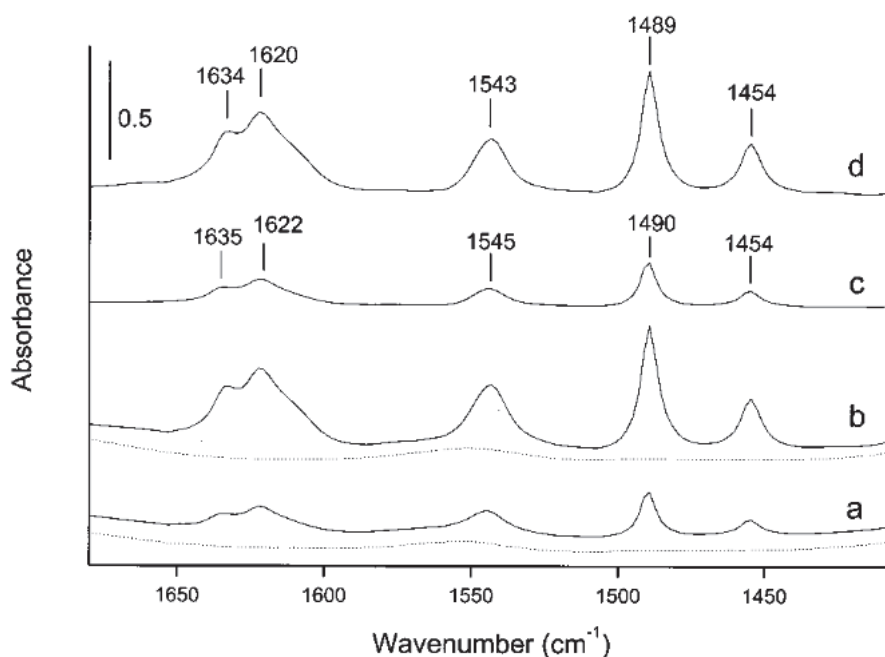


**Figure 8.** FTIR spectra showing the 1700-1400  $\text{cm}^{-1}$  region of pyridine desorbed at 150°C on (a) CBV760 and (b) CBV712 (stippled and solid spectra are recorded before and after pyridine adsorption). (c) and (d) are the subtracted spectra showing the spectral changes due to pyridine on CBV760 and CBV712. Reproduced from [19].

The second region of interest is in the range of 1700-1400  $\text{cm}^{-1}$ , corresponding to the interaction between the pyridine and the surface of the material. Figure 8 displays the FTIR spectra of Y zeolite

after pyridine adsorption. Two bands at 1635 and 1545  $\text{cm}^{-1}$  are assigned to the ring vibration of pyridinium ion ( $\text{PyH}^+$ ). Pyridine coordinated to the zeolite leads to the vibration bands at 1621 and 1455  $\text{cm}^{-1}$  (PyL). A fifth band, that cannot be assigned to a single site is observed at 1490  $\text{cm}^{-1}$  [17].

**Table 3.** Assignment of the vibration bands observed in the range of 1700-1400  $\text{cm}^{-1}$  [19][22]

Wavenumber ( $\text{cm}^{-1}$ )	Adsorbed species	Corresponding acid sites
1635	Pyridinium ion	Brønsted
1621	Pyridine	Lewis
1545	Pyridinium ion	Brønsted
1490	Pyridine + pyridinium ion	Lewis + Brønsted
1455	Pyridine	Lewis

### 4.4 Calculation of the number of acid sites

The adsorption bands at 1545 and 1455  $\text{cm}^{-1}$  are used for the calculation of the number of Brønsted and Lewis acid sites, respectively. The concentration of these acid sites,  $q_B$  and  $q_L$ , are calculated according to the following equation:

Brønsted acid site

$$q_B = \frac{A_B \pi R^2}{w \varepsilon_B}$$

Lewis acid site

$$q_L = \frac{A_L \pi R^2}{w \varepsilon_L} \quad (10)$$

Where  $A_B$  and  $A_L$  are the area of the adsorption bands at 1545 and 1455  $\text{cm}^{-1}$  [ $\text{cm}^{-1}$ ],  $R$  is the radius of the wafer [cm],  $w$  is the weight of the sample [g] and  $\varepsilon_B$  and  $\varepsilon_L$  are the integrated extinction coefficients for Brønsted and Lewis acid sites.

The extinction coefficients should be determined by introducing a known amount of the probe molecule into the cell. The progressive change in intensity for the considered band as a function of the amount of probe introduced into the cell allows determining the integrated molar adsorption. This method needs the introduction of a carefully calibrated amount of pyridine, which is not possible in our case. Such coefficients have already been determined by other research groups and are widely used in the literature. The integrated extinction coefficients from C. A. Emeis work,  $\varepsilon_B=1.67\text{cm}.\mu\text{mol}^{-1}$  and  $\varepsilon_L=2.22\text{cm}.\mu\text{mol}^{-1}$ , are chosen for the calculations of the equations (8) [23].

The strength of acid sites is investigated by normalization of the number of acid sites obtained after desorption of the pyridine at 150°C.

### 5. Zero Length Column

To investigate the transport limitation within the catalyst used during this project, diffusion measurements are performed via Zero-Length Column (ZLC) method. This method have been developed by Ruthven and applied to many systems, either in gas or liquid phases [19][20].

#### 5.1 Principle of the technique

The ZLC technique has been developed to measure the intracrystalline diffusion in zeolite. A small amount of adsorbent – the zeolite – is exposed to an adsorbate, diluted in an inert carrier gas, at known partial pressure. Equilibration is preferably performed within the Henry's law region of the isotherm in order to simplify the calculation of the ZLC theory [26]. When equilibrium is reached, the system is purged with an inert gas at high flow rate. Thus, the adsorbate concentration in the effluent gas corresponds to the desorption rate of this molecule. A flame ionization detector (FID) is used for the measurement of the organic sorbates concentration since it is a sensitive detector that is not subject to interferences due to inorganic purge gas.

#### 5.2 Experimental system

Figure 9 shows the experimental setup available at IRCELYON. It is composed of gas supply lines, a reactor containing the sample to analyse and a FID system. Separate lines for the adsorption and desorption steps enable a straight change in the gas stream composition. The relation  $MF1+MF2=MF3$  must be respected in order to keep constant flow. The switch of the gas stream is performed by a 4-way valve. Heating cables along the process lines limit the adsorption of the adsorbate on the tube walls and valves. The reactor is a stainless steel tube fitting 1/8" from Swagelok (Figure 10). It contains a small amount of zeolite placed between two porous discs. A monolayer of zeolite powder is made to ensure good contact with the gas stream. The temperature of the reactor is set by the analytical system containing the FID.

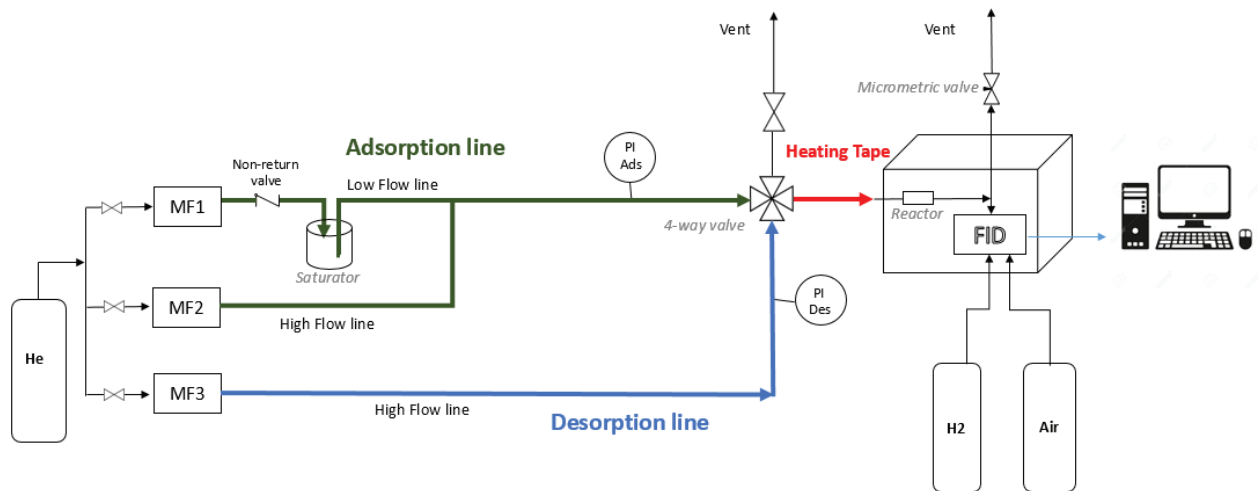


**Figure 9.** Scheme of the ZLC setup

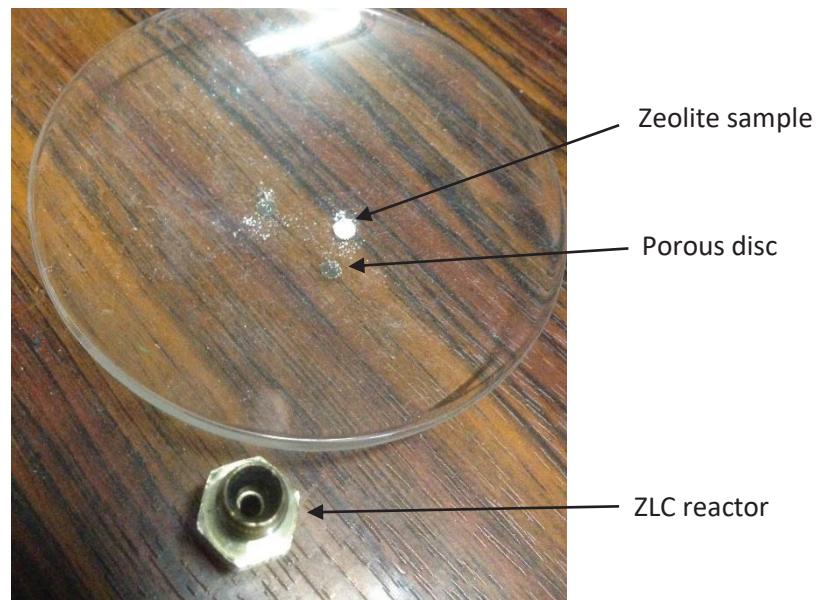


**Figure 10.** Picture of the ZLC reactor, porous discs and zeolite sample after a ZLC measurement.

### 5.3 Theory

Considering there is no significant external resistance to mass transfer since the zeolite crystals are dispersed approximately as a monolayer across the reactor, an equilibrium between the purge gas and the sorbate at the external surface of the crystals is maintained. From Fick diffusion equation and mass balance consideration over the ZLC reactor, Ruthven et al. obtained the following equation [27]:



$$\frac{c}{c_0} = 2L \sum_{n=1}^{\infty} \frac{\exp(-\beta_n^2 Dt/r_c^2)}{\beta_n^2 + L(L-1)} \quad (11)$$

Where  $c$  is the adsorbate concentration,  $D$  is the diffusivity,  $r_c$  is the crystal diameter and  $\beta_n$  is given by:

$$\beta_n \cot \beta_n + L - 1 = 0 \quad (12)$$

And  $L$ :

$$L = \frac{1}{3} \times \frac{\text{purge flow rate}}{\text{crystal volume}} \times \frac{r_c^2}{KD} \quad (13)$$

In the long-time region, the large values of  $t$  simplify the equation (11). Only the first term of the summation is significant, leading to the new equation:

$$\ln\left(\frac{c}{c_0}\right) \approx \ln\left[\frac{2L}{\beta_1^2 + L(L-1)}\right] - \beta_1^2 \frac{Dt}{R^2} \quad (14)$$

At high flow rate, large values of  $L$  are obtained and  $\beta_1$  approaches  $\pi$  (equation 11 and 12). It also implies that the intercept of the plot  $c/c_0 = f(t)$  approaches  $2/L$  and the slope, as well as the diffusion, is independent of the flow rate. These conditions, which correspond to the kinetic regime, are considered to be the best for measurements of the intracrystalline diffusivity [27].

#### 5.4 Typical steps of ZLC measurements

The first step before starting ZLC diffusion measurements is to perform or find in the literature, the adsorption isotherms of the adsorbate on the studied zeolite. The maximal vapour pressure that is found to stay within Henry's law region fixes the saturator temperature and carrier gas flows (MF1 and MF2).

Around 1-2g of zeolite are loaded between two porous discs within the reactor. The sample is activated for one night at 300°C under helium flow. Another preliminary check aiming to determine the experimental regime is performed. To this end, experiments are performed at several purge flows from 50 to 110 mL/min. Kinetic regime is obtained when the slope of the plot  $c/c_0 = f(t)$  is independent of the flow.

After this verification, experiments at several temperatures are carried out, starting from the lowest to the highest. The same time for adsorption and desorption is applied. According to Silva et al. the desorption time should be higher than  $7.0 \times 10^{-2} \frac{r_c^2}{D_c}$  [28]. During this PhD, the ZLC measurement



## Chapter II – Experimental methods

carried out with methylene are performed with desorption of 1h. The smallest  $D/R^2$  coefficients are in the order of  $0.5E-04 \text{ s}^{-1}$ , which lead to desorption time of 1400s according to Silva et al. assumption. Hence, the desorption time applied fulfils this criterion.

A blank test – without zeolite – is performed with each adsorbate to determine the response time of the system.

To compute the data, normalization of the signal is performed according to the equation (Figure 11):

$$\frac{c}{c_0} = \frac{I - I_{inf}}{I_0 - I_{inf}} \quad (15)$$

Where:  $I$  is the intensity of FID signal

$I_0$  is the highest value after the switch from adsorption step to desorption step

$I_{inf}$  is the value for large  $t$ . For our experiments,  $I_{inf}$  is taken equal to 50.

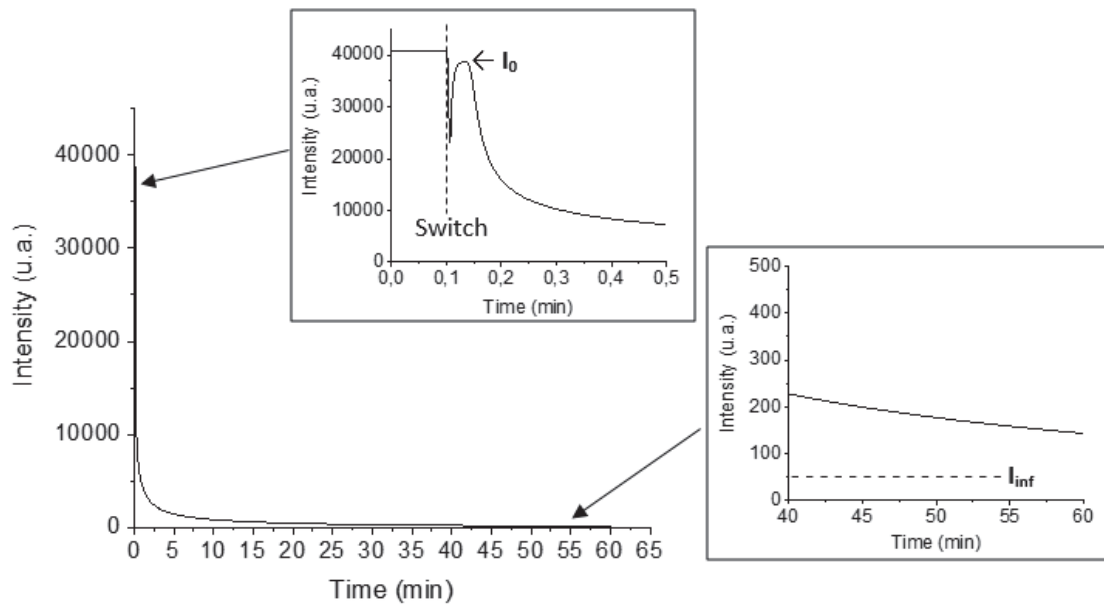


**Figure 11.** Processing of the FID data obtained during ZLC measurement

Then  $c/c_0$  is plot as a function of the time and the exponential of equation (14) is fitted to the experimental data in the long-term region, leading to  $D/R^2$  and  $\beta$  values. The long-term slope should decrease with an increase of the temperature [Figure 7].

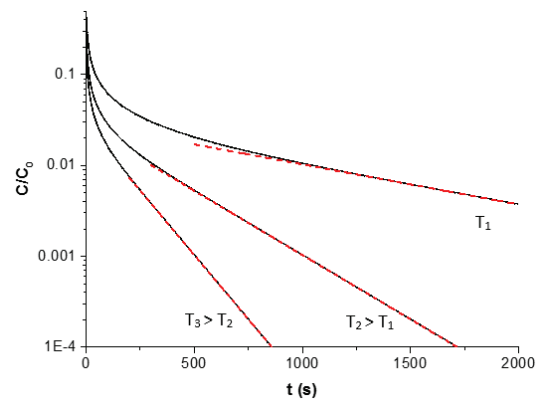


**Figure 12.** Example of ZLC curves (black) and long-term fittings (red) obtained at three different temperatures.

### References for Chapter II

- [1] X. Hou and B. T. Jones, "Inductively Coupled Plasma/Optical emission Spectrometry," *Encyclopedia of Analytical Chemistry*. pp. 58-, 2000.
- [2] "International Centre for Diffraction." [Online]. Available: <http://www.icdd.com/>.
- [3] "Standard Test Method for Determination of Relative X-ray Diffraction Intensities of Faujasite-Type Zeolite-Containing Materials," in *ASTM INTERNATIONAL*, .
- [4] H. Fichtner-Schmittler, U. Lohse, G. Engelhardt, and V. Patzelova, "Unit Cell Constants of Zeolites Stabilized by Dealumination," *Cryst. Res. Technol.*, vol. 19, no. 1, pp. K1–K3, 1984.
- [5] G. Engelhardt, U. Lohse, V. Patzelová, M. Mägi, and E. Lippmaa, "High resolution  $^{29}\text{Si}$  n.m.r. of dealuminated Y-zeolites. 1. The dependence of the extent of ammonium exchange and the temperature and water vapour pressure of thermochemical treatment," *Zeolites*, vol. 3, pp. 233–238, 1983.
- [6] G. Engelhardt and U. Lohse, "High resolution  $^{29}\text{Si}$  n.m.r. of dealuminated Y-zeolites. 2. Silicon, aluminium ordering in the tetrahedral zeolite lattice," *Zeolites*, vol. 3, pp. 239–243, 1983.
- [7] D. W. Breck and E. M. Flanigen, "Molecular Sieves," *Soc. Chem. Ind. London*, p. 47, 1968.
- [8] L. E. Sandoval-Diaz, J. A. Gonzalez-Amaya, and C. A. Trujillo, "General aspects of zeolite acidity characterization," *Microporous Mesoporous Mater.*, vol. 215, pp. 229–243, 2015.
- [9] M. Thommes *et al.*, "Physisorption of gases, with special reference to the evaluation of surface area and pore size distribution (IUPAC Technical Report)," *Pure Appl. Chem.*, vol. 87, no. 9–10, pp. 1051–1069, 2015.
- [10] S. Brunauer, P. H. Emmett, and E. Teller, "Adsorption of Gases in Multimolecular Layers," *J. Am. Chem. Soc.*, vol. 60, no. 2, pp. 309–319, 1938.
- [11] A. Galarneau, F. Villemot, J. Rodriguez, F. Fajula, and B. Coasne, "Validity of the t-plot method to assess microporosity in hierarchical micro/mesoporous materials," *Langmuir*, 2014.
- [12] J. Klinowski, "Nuclear Magnetic Resonance Studies of Zeolites," *Prog. NMR Spectrosc.*, vol. 16, pp. 237–309, 1984.
- [13] H. Ben and J. R. Ferrell Iii, "In-depth investigation on quantitative characterization of pyrolysis oil by  $^{31}\text{P}$  NMR," *RSC Adv.*, vol. 6, 2016.
- [14] B. Omais, M. Courtiade, N. Charon, D. Thiébaud, A. Quignard, and M. C. Hennion,

- “Investigating comprehensive two-dimensional gas chromatography conditions to optimize the separation of oxygenated compounds in a direct coal liquefaction middle distillate,” *J. Chromatogr. A*, vol. 1218, no. 21, pp. 3233–3240, 2011.
- [15] A. Margeriat *et al.*, “Catalytic conversion of beech wood pyrolytic vapors,” *J. Anal. Appl. Pyrolysis*, vol. 130, no. August 2017, pp. 249–255, 2018.
- [16] J. N. Miale, N. Y. Chen, and P. B. Weisz, “Catalysis by Crystalline Aluminosilicates IV. Attainable Catalytic Cracking Rate Constant, and Superactivity,” *J. Catal.*, vol. 6, no. 2, pp. 278–287, 1966.
- [17] T. Barzetti, E. Selli, D. Moscotti, and L. Forni, “Pyridine and ammonia as probes for FTIR analysis of solid acid catalysts,” *J. Chem. Soc. Faraday Trans.*, vol. 92, no. 8, p. 1401, 1996.
- [18] S. Bordiga, C. Lamberti, F. Bonino, A. Travert, and F. Thibault-Starzyk, “Probing zeolites by vibrational spectroscopies,” *Chem. Soc. Rev.*, vol. 44, no. 20, pp. 7262–7341, 2015.
- [19] W. Daniell, N. Y. Topsøe, and H. Knözinger, “An FTIR study of the surface acidity of USY zeolites: Comparison of CO, CD<sub>3</sub>CN, and C<sub>5</sub>H<sub>5</sub>N probe molecules,” *Langmuir*, vol. 17, no. 20, pp. 6233–6239, 2001.
- [20] V. Rac, D. Stošić, V. Rakić, and A. Auroux, “Acidity of Hierarchical Fau , Bea and Zsm-5 Zeolites,” pp. 140–143.
- [21] J. A. Lercher and A. Jentys, “Chapter 13 - Infrared and raman spectroscopy for characterizing zeolites,” in *Introduction to Zeolite Science and Practice*, vol. 168, 2007, pp. 435–476.
- [22] E. P. Parry, “An Infrared Study of Pyridine Adsorbed on Acidic Solids. Characterization of Surface Acidity,” *J. Catal.*, vol. 2, pp. 371–379, 1963.
- [23] C. A. Emeis, “Determination of integrated molar extinction coefficients for infrared absorption bands of pyridine adsorbed on solid acid catalysts,” *Journal of Catalysis*, vol. 141, no. 2. pp. 347–354, 1993.
- [24] M. Eic and D. M. Ruthven, “Diffusion of linear paraffins and cyclohexane in NaX and 5A zeolite crystals,” *Zeolites*, vol. 8, no. 6, pp. 472–479, 1988.
- [25] S. Brandani and D. M. Ruthven, “Analysis of ZLC desorption curves for liquid systems,” *Chem. Eng. Sci.*, vol. 50, no. 13, pp. 2055–2059, 2002.
- [26] S. Brandani, M. A. Jama, and D. M. Ruthven, “ZLC measurements under non-linear conditions,” *Chem. Eng. Sci.*, vol. 55, no. 7, pp. 1205–1212, 2000.

- [27] J. Kärger, D. M. Ruthven, and D. N. Theodorou, *Diffusion in Nanoporous Materials*. 2012.
- [28] J. A. C. Silva and A. E. Rodrigues, “Limitations of the Zero-Length Column Technique to Measure Diffusional Time Constants in Microporous Adsorbents,” *Chem. Eng. Technol.*, vol. 38, no. 12, pp. 2335–2339, 2015.

# Chapter III: Preparation and characterization of the hierarchical Y zeolites

---

## 1. Synthesis of the materials

### 1.1 Zeolite Y from Zeolyst

Post-synthesis modification of Y zeolite has been chosen as preparation method of the hierarchical zeolites. The starting Y zeolite used for this preparation of the hierarchical catalysts is manufactured by the company Zeolyst. This company offers Y zeolites with Si/Al ratios from 2.55 to 40 and  $H^+$ ,  $NH_4^+$  or  $Na^+$  counter ions (Table 1). To be an effective catalyst in the FCC process, the Y zeolite needs to be ultra-stabilized (see Chapter I, Part 4.2) [1]. A common way to obtain such USY zeolite is to perform a steaming treatment that removes some aluminium atoms from the framework. The Y zeolite CBV720, which is considered as a USY zeolite with its Si/Al ratio of 15 due to a steaming and ion exchange of the CBV100, has been chosen as starting parent material for the preparations of the hierarchical zeolites.

**Table 1.** Zeolite Y available from the manufacturer Zeolyst and sample characteristics published on their website [2].

Zeolyst Products	Si/Al Mole Ratio	Nominal Cation Form	Na <sub>2</sub> O Weight %	Unit Cell Size, Å	Surface Area, m <sup>2</sup> /g
CBV100	2.55	Sodium	13.0	24.65	900
CBV300	2.55	Ammonium	2.8	24.68	925
CBV400	2.55	Hydrogen	2.8	24.50	730
CBV500	2.6	Ammonium	2.8	24.53	750
CBV600	2.6	Hydrogen	0.2	24.35	660
CBV712	6	Ammonium	0.05	24.35	730

CBV720	15	Hydrogen	0.03	24.28	780
CBV760	30	Hydrogen	0.03	24.24	720
CBV780	40	Hydrogen	0.03	24.24	780
CBV901	40	Hydrogen	0.03	24.24	700

### 1.2 Hierarchical Y zeolite with Si/Al=15

To prepare hierarchical zeolites, the top-down approach based on surfactant-templated crystal rearrangement has been chosen. In this approach, a diluted alkaline solution is used in order to avoid the usual loss of silica that the desilication method is facing. The chosen approach allows the preparation of hierarchical zeolites without creating a significant amorphous phase nor desilication because of the reasonable pH value around 10.5 [3], [4].

A first sample, based on the work published by Javier Garcia-Martinez et al. [4], is prepared. According to this method, 4.38g of cetyltrimethylammonium Bromide (CTAB) is dissolved into 400mL of a 0.37M  $\text{NH}_4\text{OH}$  solution. After a short time of homogenization, 6.25g of CBV720 is added and followed by a 20min stirring step. Then, the mixture is heated under autogenous pressure for 10h at 150°C. After cooling down at room temperature the sample is washed with deionized water, dried overnight at 90°C and calcined for 10h at 550°C. This sample is referred to as H-USY-1 within the following results sections.

A second preparation, based on the same surfactant-templated mechanism and published by Gérardin et al. [5], is prepared. For this preparation, 9.50g of tetramethylammonium hydroxide (TMAOH) is dissolved into 290mL of water to prepare a 0.09M TMAOH solution. Then, 5g of CTAB is added and the solution is stirred. When a homogeneous solution is obtained, 10g of CBV720 is added and followed by a 20min stirring step. The mixture is transferred to a Teflon-lined stainless-steel autoclave for a 20h-treatment at 150°C. After cooling down at room temperature the sample is washed with deionized water, dried overnight at 90°C and calcined for 10h at 550°C. This sample is called H-USY-2 within the following results sections.

An additional sample, named H-Y and consisting of the CBV400 from Zeolyst has been characterized and tested with the USY series in order to enlarge the comparison scale of materials.

**Table 2.** Sum up of treatment conditions carried out on CBV720

Parent material	Base	Surfactant	Amount of zeolite	Treatment at autogenous pressure	Sample name
CBV720	-	-	-	-	H-USY-0
CBV720	400mL 0.37M NH <sub>4</sub> OH solution	4.38g of CTAB	6.25g	10h at 150°C	H-USY-1
CBV720	290mL 0.09M TMAOH solution	5g of CTAB	10g	20h at 150°C	H-USY-2

## 2. Characterization results

### 2.1 Transmission Electronic Microscopy

Looking at the TEM images in Figure 1, mesopores are observed within the H-USY-0 structure (Figure 1-a). These irregular shaped channels disappear when the material is treated by the solutions of CTAB in TMAOH (H-USY-1) or NH<sub>4</sub>OH (H-USY-2). The new formed channels are easily observable on the HR-TEM of the H-USY-2 sample (Appendix III). As Garcia-Martinez et al. [4] explained, this phenomenon is due to the dissolution-reorganization process occurring during the treatment. Alkaline solution favours Si-O-Si bonds opening, creating negative charges into the zeolite framework. Positively charged surfactants move through the zeolite by means of electrostatic interactions. The crystal rearrangements occurring around the micelles formed by the self-assembled surfactant cations are responsible for the disappearance of the irregular mesopores, in favour of the regular shaped ones. This addition of a mesoporous network led to the concept of hierarchical zeolite, materials having multi-scale porosity that allow an inlet flow to be well distributed through the zeolite crystal [6].



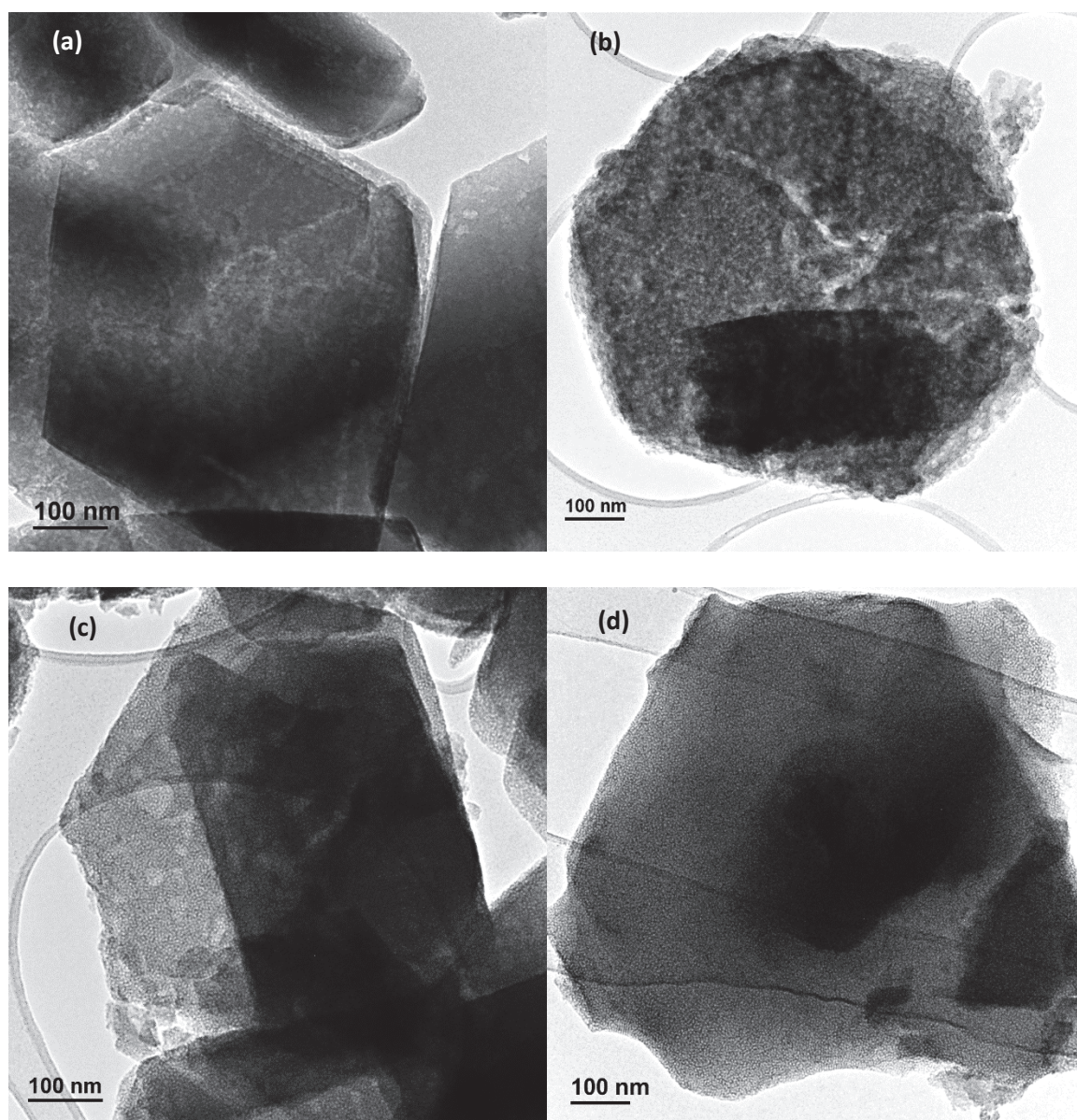


**Figure 1:** TEM images of the samples (a) H-Y, (b) H-USY-0, (c) H-USY-1 and (d) H-USY-2.

## 2.2 Nitrogen adsorption-desorption isotherms

Figure 2-a displays the  $N_2$  adsorption-desorption isotherms obtained for the materials H-USY-0, H-USY-1, H-USY-2 and H-Y (CBV400). The H-Y sample exhibits a type-I isotherm, typical for microporous solids. The sample H-USY-0 displays a combination of type-I and IV isotherms. The adsorption branch is similar to type-I isotherm, typical of the microporous structure, and a hysteresis loop appears above  $p/p_0 = 0.45$ , corresponding to the IUPAC H4-type [7]. When looking at the desorption branch, it is parallel to the adsorption branch in the 1 to 0.8 range, indicating that those large mesopores are “open” and may correspond to the large fractures visible in Fig. 1-a. For lower pressures, it is almost horizontal and the closure at  $p/p_0 = 0.45$  indicates that some of the mesopores are closed and

communicate with the surface via a porosity smaller than 4 nm. These mesopores are created during the dealumination process carried out by Zeolyst. The H-USY-1 and H-USY-2 samples show type-IV isotherms with an  $N_2$  uptake at  $p/p_0 = 0.3$ -0.4. This is due to the creation of an additional mesoporous network to the parent materials. The sharpest increase of  $N_2$  adsorbed for H-USY-2 indicates the presence of more uniform mesopores in this material [5]. The uptake is not only sharper, but it is also greater, which suggests that the mesopore volume is higher in H-USY-2. Looking at the values in Table 3, the mesopore volumes – obtained by difference between the total and microporous volumes – are  $0.22 \text{ cm}^3/\text{g}$  for H-USY-1 and  $0.32$  for H-USY-2. Moreover, there are no hysteresis loops on these two isotherms. All newly created mesopores are totally open, as they are for MCM-41 amorphous silicas for example.

Higher pore volumes are obtained for the H-USY-1 and H-USY-2 materials than for the parent H-USY-0, with  $0.50 \text{ cm}^3/\text{g}^{-1}$  and  $0.55 \text{ cm}^3/\text{g}^{-1}$  against  $0.45 \text{ cm}^3/\text{g}^{-1}$ , respectively (Table 3). The higher total pore volumes for hierarchical materials go in pairs with lower microporous volumes. The addition of the mesoporous network seems to be at the expense of the initial microporous volume. For a theoretically perfect FAU zeolite, the microporous volume is  $0.31 \text{ cm}^3/\text{g}^{-1}$ .

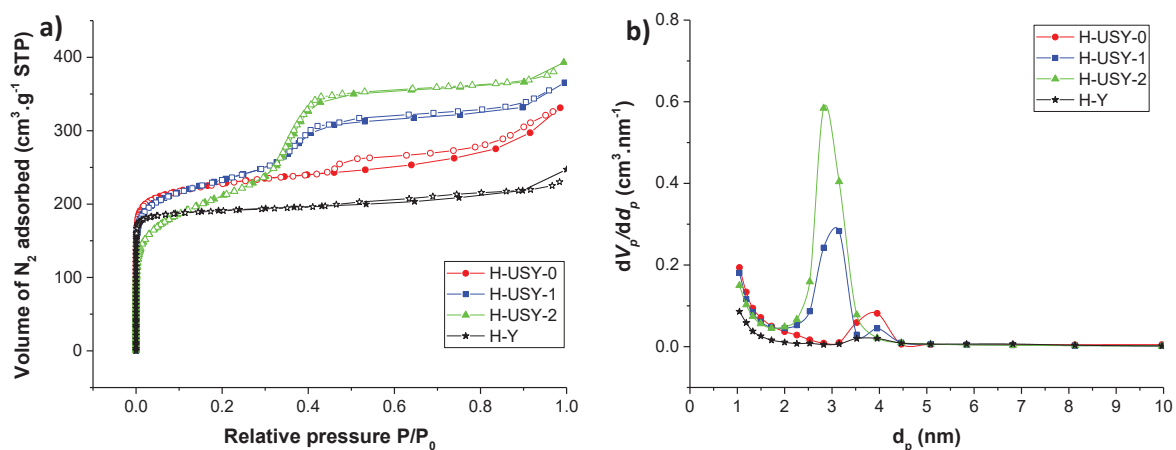


**Figure 2:** (a)  $N_2$  adsorption-desorption isotherm at 77K and (b) the pore size distribution using the BJH on the desorption branch.

**Table 3:** BET surface area, micropore volume and total pore volume obtained from  $N_2$  isotherm displayed in Figure 1.

Catalyst	$S_{\text{BET}}^a [\text{m}^2 \cdot \text{g}^{-1}]$	$V_{\text{micro}}^b [\text{cm}^3 \cdot \text{g}^{-1}]$	$V_{\text{total}}^c [\text{cm}^3 \cdot \text{g}^{-1}]$
H-USY-0	869	0.30	0.45
H-USY-1	827	0.28	0.50

H-USY-2	709	0.23	0.55
H-Y	721	0.26	0.30

<sup>a</sup> BET method (constant C positive and  $p/p_0 < 0.1$ ). <sup>b</sup> Volume of N<sub>2</sub> adsorbed when the slope of adsorption branch becomes lower than 10<sup>3</sup> cm<sup>3</sup> g<sup>-1</sup>. <sup>c</sup> Volume of N<sub>2</sub> adsorbed at  $p/p_0 = 0.90$ .

The pore size distribution (PSD) of the materials can be determined by using either the non-local density functional theory method (NLDFT) on the adsorption branch of N<sub>2</sub> isotherms, or the Barrett-Joyner-Halenda (BJH) algorithm on the desorption branch. The NLDFT method, which is starting to be widely used for the characterisation of a large range of materials having multi-level porosity, is a molecular modelling approach taking into account details such adsorbate-adsorbent interactions or pore geometry [8], [9]. Whereas BJH approach is based on physical consideration coming from Kelvin equation that relates the pressure and the size of the hemispherical meniscus formed during liquid condensation in the pores. A NLDFT model based on adsorption of nitrogen at 77K in cylindrical siliceous pores is applied to the adsorption branch of the nitrogen isotherm of the four materials (Figure 3.a). The comparison between the fitted theoretical NLDFT adsorption isotherms with the measured ones is displayed in Figure 3.b. The PSD gives a good idea of the contribution made by the hierarchization of the parent H-USY-0. The apparition of the peak corresponding to mesopores is observed around 5nm of diameter, which is in the range of the 4 to 6nm-diameter that is expected with CTAB micelles as a structural agent [4]. This peak is broader for H-USY-1 sample than H-USY-2 one. The better fitting of NLDFT method, at the step level between  $P/P_0$  of 0.2 and 0.4, can explain this difference. The BJH plot applied to the desorption branch led to lower pore diameter (Figure 2-b). By this method, the H-USY-0 sample exhibits mesopores of 4-nm diameter, due to the consideration of the hysteresis loop by applying BJH method to the desorption branch. The hierarchical H-USY-1 and H-USY-2 samples display a mesoporous network with a pore size diameter of 3nm.

Regarding the peak corresponding to the micro porosity, from NLDFT method, small variations of pore diameter are observed between the four samples. This could be explained by the quadrupole moment of the nitrogen that is known to interact with zeolite surfaces, affecting the micropores filling pressure by shifting it and inducing some experimental errors [7], [9]. However, the exact pore diameter of micropores is not essential, already knowing Y zeolite is composed of supercavities of 1.3nm diameter connected through 0.74nm windows [10].

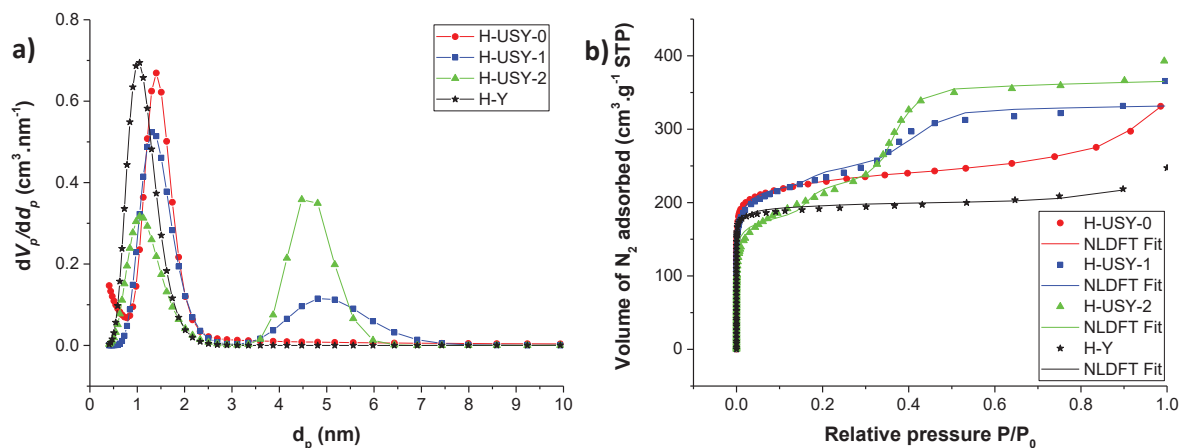


**Figure 3.** Application of NLDFT method to H-USY-0, H-USY-1, H-USY-2 and H-Y. (a) PSD derived from the NLDFT method applied to the nitrogen adsorption isotherms. (b) Comparison between the NLDFT theoretical adsorption branch isotherms with experimental nitrogen adsorption isotherms.

### 2.3 X-Ray Diffraction

Figure 4 presents the powder X-Ray Diffraction (XRD) patterns of zeolites H-Y, H-USY-0, H-USY-1 and H-USY-2 at low and wide angles. At wide angles, all patterns exhibit the characteristic peaks of the Y zeolite framework as it has been confirmed by comparison with the XRD pattern database. The intensities of the peaks of the hierarchical zeolites H-USY-1 and H-USY-2 decrease by comparison with the parent H-USY-0. This is due to a loss of crystallinity, which can be semi-quantified and calculated as described in Chap. II part 1.2. The values are reported in Table 4. The exact positions of the XRD peaks on the wide angles XRD patterns depend on the unit cell parameters  $a_0$  of the samples, which are also reported in Table 4. A shift to slightly higher angles is observed for the hierarchical samples, leading to a higher framework Si/Al ratio according to the Fichtner-Schmittler formula. This could be explained by the localized hydrolysis of Al-O bonds, removing some aluminium atoms from the framework [11]. The phenomenon is less significant on the H-USY-1 sample than H-USY-2.

Regarding the low angles XRD patterns in Figure 4-a, an intense peak at  $1.9^\circ$   $2\theta$  appears for the hierarchical zeolites, which is typical of vermicular mesoporous structure [5]. The spatial pore arrangement of these mesoporosity is found to be hexagonal because of the weak and broad peak observed around  $4^\circ$   $2\theta$ . Using Bragg's law, the corresponding  $d$  spacing calculated from the position of the (100) peak at  $1.9^\circ$   $2\theta$  is  $46.5\text{\AA}$ , which corresponds to lattice constant of  $53.7\text{\AA}$ . This value is slightly above the mesopore diameter of 4-5nm observed on the PSD obtained via NLDFT, which is normal.

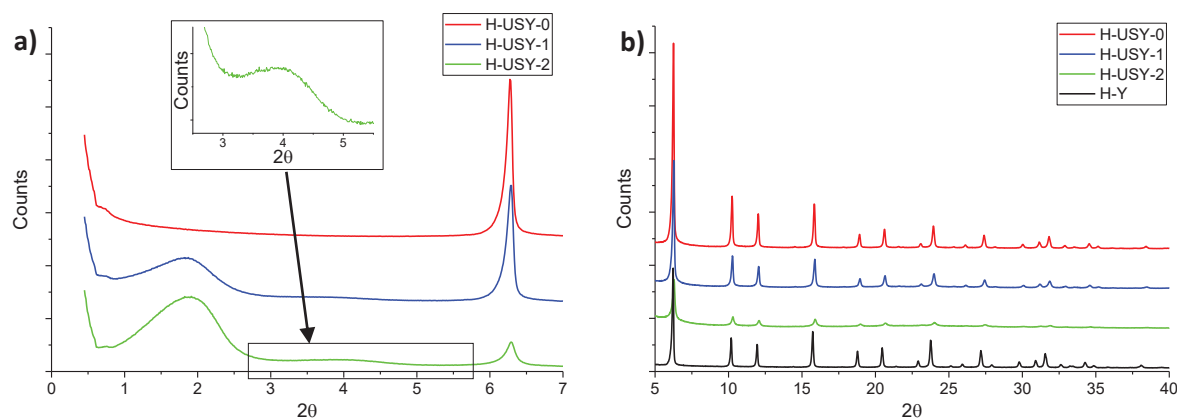


**Figure 4:** Small (a) and wide (b) angles XRD patterns.

**Table 4:** Framework Si/Al ratio and crystallinity obtained from XRD measurements

Sample	$a_0$ (Å)	Si/Al <sup>a</sup>	Crystallinity (%)
H-USY-0	24.35	13.6	100
H-USY-1	24.32	18.6	70.7
H-USY-2	24.29	29.0	25.1
H-Y	24.53	2.9	-

<sup>a</sup> Calculated according to the Fichtner-Schmittler formula.

## 2.4 Elementary analysis (ICP-OES)

The Si/Al ratios obtained from XRD analysis are compared to the ones calculated from ICP-OES. The chemical compositions of H-USY-0, H-USY-1, H-USY-2 and H-Y samples are determined from ICP-OES and reported in Table 5. The H-USY-1 and H-USY-2 samples show a slightly lower silica concentration by comparison with the parent H-USY-0. This is explained by the treatment carried out in an alkaline solution, which is commonly used for desilication. However, the loss of silica is limited and the Si/Al ratio of the three materials H-USY-0, H-USY-1 and H-USY-2 are still similar. However, the Si/Al ratio obtained from XRD differs from the one obtained from elementary analysis. The presence of extra framework aluminium (EFAL) is expected. This EFAL proportion should be the highest for the sample H-USY-2, since the difference between the structural (by XRD) and overall (by ICP-OES) Si/Al ratios is the highest.



**Table 5:** Elemental composition determined by ICP-OES.

Sample	Si (wt. %)	Al (wt. %)	Na (wt. %)	Si/Al (molar ratio) <i>From ICP-OES</i>	Si/Al (molar ratio) <i>From XRD</i>
H-USY-0	38.5	2.5	0.02	14.8	13.6
H-USY-1	36.9	2.5	0.05	14.4	18.6
H-USY-2	36.7	2.5	0.02	14.1	29.0
H-Y	25.1	9.7	1.6	2.5	2.9

## 2.5 $^{27}\text{Al}$ and $^{29}\text{Si}$ NMR

From  $^{27}\text{Al}$  MAS-NMR analyses (Figure 5-a), the presence of framework aluminium (FAL) and hexacoordinated extra framework aluminium (EFAL) are observed for the sample H-USY-0 at 60ppm and 0ppm, respectively. A similar observation is made for H-USY-1. The shoulder that is observed at 52ppm can be assigned to non-framework tetrahedral aluminium [12]. The hierarchical H-USY-2 sample exhibits a different  $^{27}\text{Al}$  MAS-NMR signal. For this material, non-clearly defined peaks appear in the range of 0-60ppm, suggesting the presence of the three aluminium species: hexa- (0ppm) and pentacoordinated (30ppm) EFAL as well as tetracoordinated FAL (60ppm). This presence of EFAL is in line with the framework Si/Al ratio obtained from XRD analyses, where higher structural Si/Al ratios were obtained for the hierarchical materials (Table 5). The presence of extra framework aluminium is also observed for the H-Y sample. This sample, prepared from CBV100 by Zeolyst via ion exchange and calcination, undergoes harsh treatment conditions. The calcination of the  $\text{NH}_4^+$ -form zeolite to obtain the  $\text{H}^+$ -form creates the EFAL that are identified.

The  $^{29}\text{Si}$  MAS-NMR spectra (Figure 5-b) of the parent H-USY-0 shows three signals. The strongest at -107ppm is assigned to the Si(0Al) environment, while the other signal at -102ppm is assigned to Si(1Al). The latter also contains the contribution of Si-OH groups formed upon dealumination and/or desilication. For this reason, it is not possible to calculate an accurate value of the Si/Al framework ratio from  $^{29}\text{Si}$  NMR spectra. The third weak signal at -111ppm is due to amorphous silica. The intensity of this signal at -111ppm is higher for the hierarchical H-USY-1 and H-USY-2 samples. It ascertains the loss of crystallinity observed by XRD for these samples. The H-Y sample exhibits an additional peak at -97ppm, corresponding to the Si(2Al) environment. This is due to its high aluminium content by comparison with the other investigated samples.

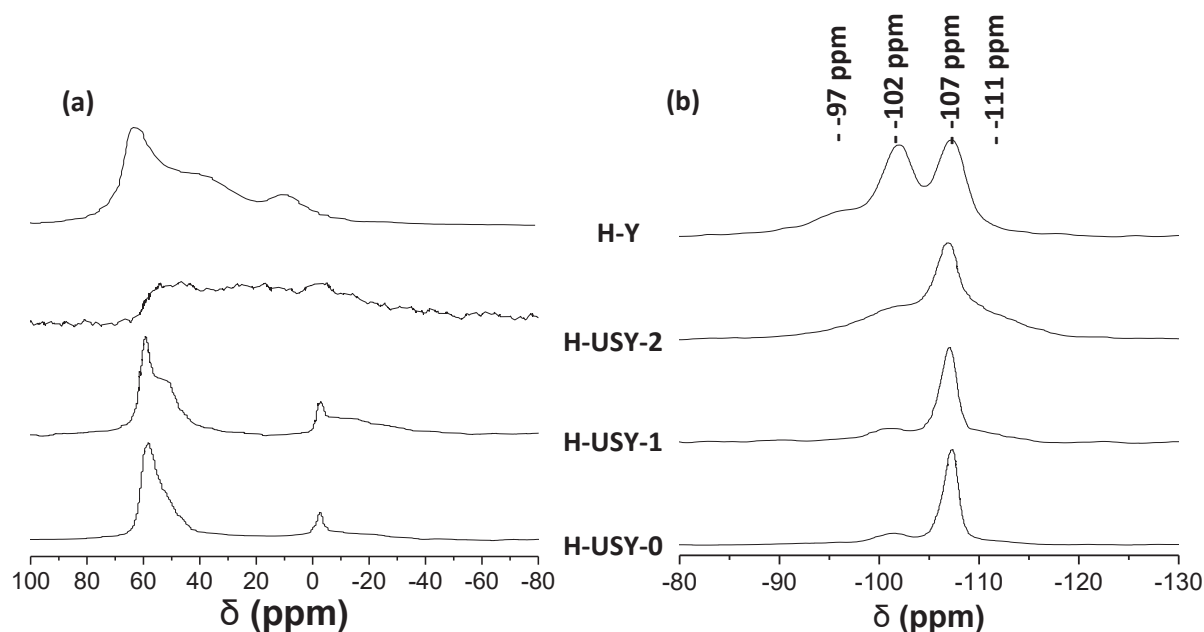


**Figure 5:** (a)  $^{27}\text{Al}$  MAS-NMR and (b)  $^{29}\text{Si}$  MAS-NMR of H-USY-0, H-USY-1, H-USY-2 and H-Y samples.

### 3. Zero Length Column

The zero length column (ZLC) method for intraparticle diffusion measurement in zeolites has been initially developed by Eic and Ruthven [13]. Since then, this method has been used with various combinations of adsorbates and adsorbents. Cavalcante Jr. et al. have studied the diffusivity of  $n\text{-C}_7$ ,  $n\text{-C}_8$  and  $n\text{-C}_{10}$  into dealuminated USY zeolite at 150-210°C [14]. They concluded to an absence of significant difference in diffusivities between all these adsorbates because of the large mesopore of USY material. Diffusion of larger molecules such as 1,3-diisopropylbenzene and 1,3,5-triisopropylbenzene, have been investigated in NaY zeolite by Zaman et al. [15], [16]. However, conversion of the 1,3,5-triisopropylbenzene into 1,3-diisopropylbenzene and propylene was hypothesized because of structural instability and/or catalytic cracking happening during the diffusion measurements, which were performed at temperatures above 150°C. This led to coke deposition on the adsorbent that might affect the experiment. To avoid this kind of issue, the diffusion measurements presented in this work have been carried out at lower temperatures with mesitylene, which is less reactive than the ethyl- and propyl-substituted benzene [17].

#### 3.1 Ion exchange

##### 3.1.1 Experimental conditions

To minimize the cracking reactions during diffusion measurements, the proton form of the materials previously described is exchanged to the sodium form. The ion exchanges are carried out three times

with NaCl solution at 80°C for 1h. For 1 g of H-USY-0, H-USY-1 or H-USY-2 zeolites, 100 mL of NaCl solution containing 50 mmol<sub>Na<sup>+</sup></sub>.L<sup>-1</sup>, which corresponds to around ten times more sodium ions than the zeolite has hydrogen ions, is used. For the H-Y sample, the exchange of 1g of zeolite is performed with a NaCl solution at 100 mmol<sub>Na<sup>+</sup></sub>.L<sup>-1</sup>. After each treatment, the solution is washed and filtered. After drying overnight, the Na-USY-0, Na-USY-1, Na-USY-2 and Na-Y samples are obtained from H-USY-0, H-USY-1, H-USY-2 and H-Y, respectively.

### 3.1.2 Characterization of the Na samples

The elemental composition of the Na-USY-0, Na-USY-1, Na-USY-2 and Na-Y materials, is displayed in Table 6. The Na/Al ratio of the materials is a key parameter to check the efficient execution of the ion exchange. Na-USY-0 sample has a Na/Al ratio of 1, which is coherent with the fact that according to <sup>27</sup>Al-MAS-NMR almost every aluminium atoms of the H form of the sample are part of the framework (Figure 5-a). For Na-USY-1, Na-USY-2 and Na-Y samples, the Na/Al ratio drops to 0.22, 0.18 and 0.26, respectively. This is explained by the high content of EFAL for these three materials.

**Table 6:** Elemental composition determined by ICP-OES

Sample	Si (wt. %)	Al (wt. %)	Na (wt. %)	Si/Al (molar ratio)	Na/Al (molar ratio)
Na-USY-0	37.7	2.2	2.7	16.5	1.0
Na-USY-1	37.9	2.4	0.61	15.3	0.22
Na-USY-2	37.4	2.4	0.50	15.3	0.18
Na-Y	29.0	7.9	2.4	3.5	0.26

Figure 6-a shows the volume of nitrogen adsorbed at 77K against the relative pressure  $p/p_0$  for the Na-form zeolite. For each sample, the same isotherm shape as for the H-form is obtained (Figure 1). However, the volumes of nitrogen adsorbed on the Na-form materials are slightly lower than for the H-form. By comparison, this leads to lower pore volume than the H-form zeolites (Table 3 and Figure 6-b). This could be explained by several factors. Firstly, sodium atoms have a higher radius than hydrogen atoms, which may occupy more space inside zeolite porosity. Secondly, the densities of the Na-form zeolites are higher than the H-form, leading to a lower volume of nitrogen adsorbed per gram of adsorbent. However, this latter reason may not be the most significant. For a zeolite having a



Si/Al ratio 15, a rapid calculation shows that the exchange of  $H^+$  to  $Na^+$  increases the mass weight by only 2.2%. A loss of crystallinity could have been an additional reason for such a loss of porous volume, but the comparison of the XRD patterns before and after exchange does not reveal any changes (Figure 7).

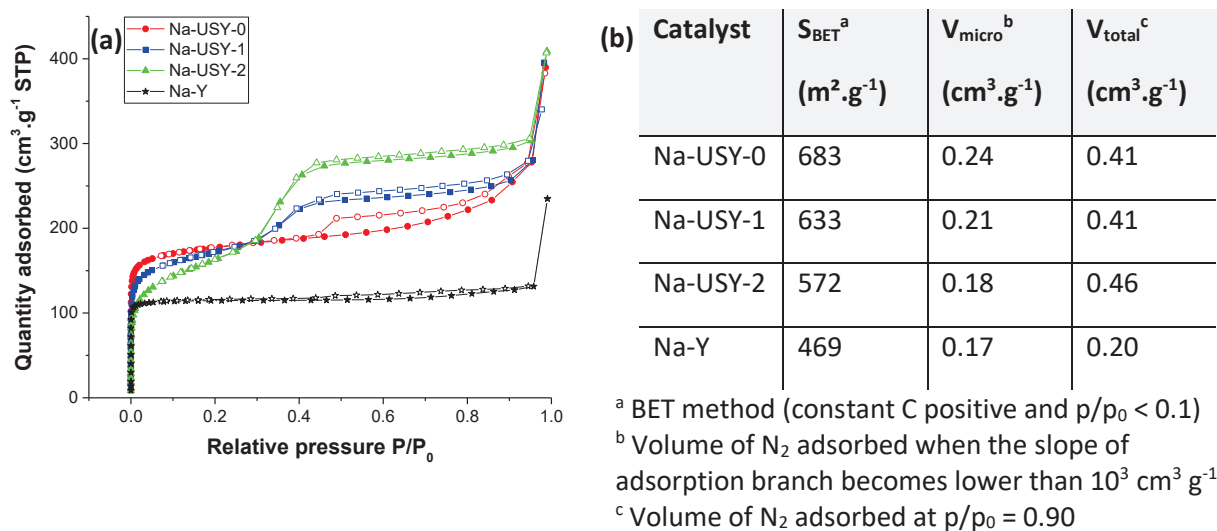


**Figure 6.** (a)  $N_2$  adsorption-desorption isotherm at 77K of the zeolite in sodium form and (b) the BET surface area, micropore volume and total pore volume corresponding.

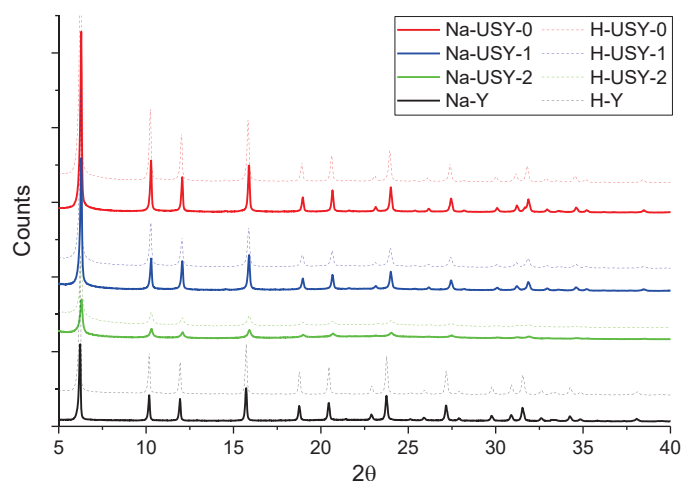


**Figure 7.** Comparison of the XRD patterns of the H and Na forms of the samples

## 3.2 Diffusion of mesitylene

Mesitylene has been chosen for transport measurement due to its kinetic diameter of  $8.4\text{\AA}$ , slightly larger than the pore opening of  $7.4\text{\AA}$  of the Y zeolite [18]. The molecule is expected to flex to enter within the micropores of Y zeolite, probing the diffusion into the entire porosity of the material. Already in 1993, Ruthven et al. studied the adsorption and diffusivities of mesitylene in NaX zeolite

using a gravimetric method [17]. The mesitylene has also been chosen by Kaliaguine et al. for their study of diffusion in mesostructured SBA-15 and SBA-16 materials by ZLC method [19], [20].

### 3.2.1 Preliminary checks

As depicted in Chapter II part 5, the zero-length column method studies the transport through a very small amount of sample, packed between two drilled disks in a Swagelok union. The diffusion data acquired from the ZLC method have to be obtained from the kinetic regime. It is a convenient condition for the determination of the diffusion time constant from the slope of the long-time linear asymptote of the plot  $\ln(C/C_0) = f(t)$ , which is the most robust and less sensitive to experimental error approach [21] (see Chapter II, part 5.3).

Under the equilibrium-controlled regime, the response curves  $C/C_0$  should only be dependent on the desorption volume. It means that the plots  $C/C_0 = f(Ft)$ , where  $F$  corresponds to the purge flow rate and  $t$  to the desorption time, should overlap for experiments recorded at different  $F$  values [22][23]. Conversely, under the diffusion-controlled regime, the curves should diverge. Such a plot is represented in Figure 8 for the desorption of mesitylene from Na-USY-0 at 60°C, with purge flow rates of 50 and 100 mL/min. The partial pressure of mesitylene is 0.05 kPa and it has been adsorbed on 1.7 mg of Na-USY-0 for 2.5 h. We see the divergence of the curves obtained at 50 and 100 mL/min of helium purge flow, confirming the kinetic-controlled regime.

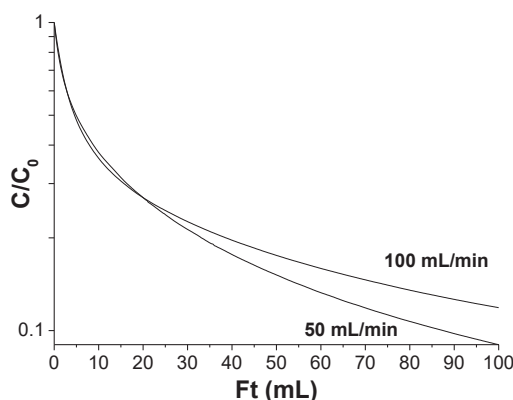
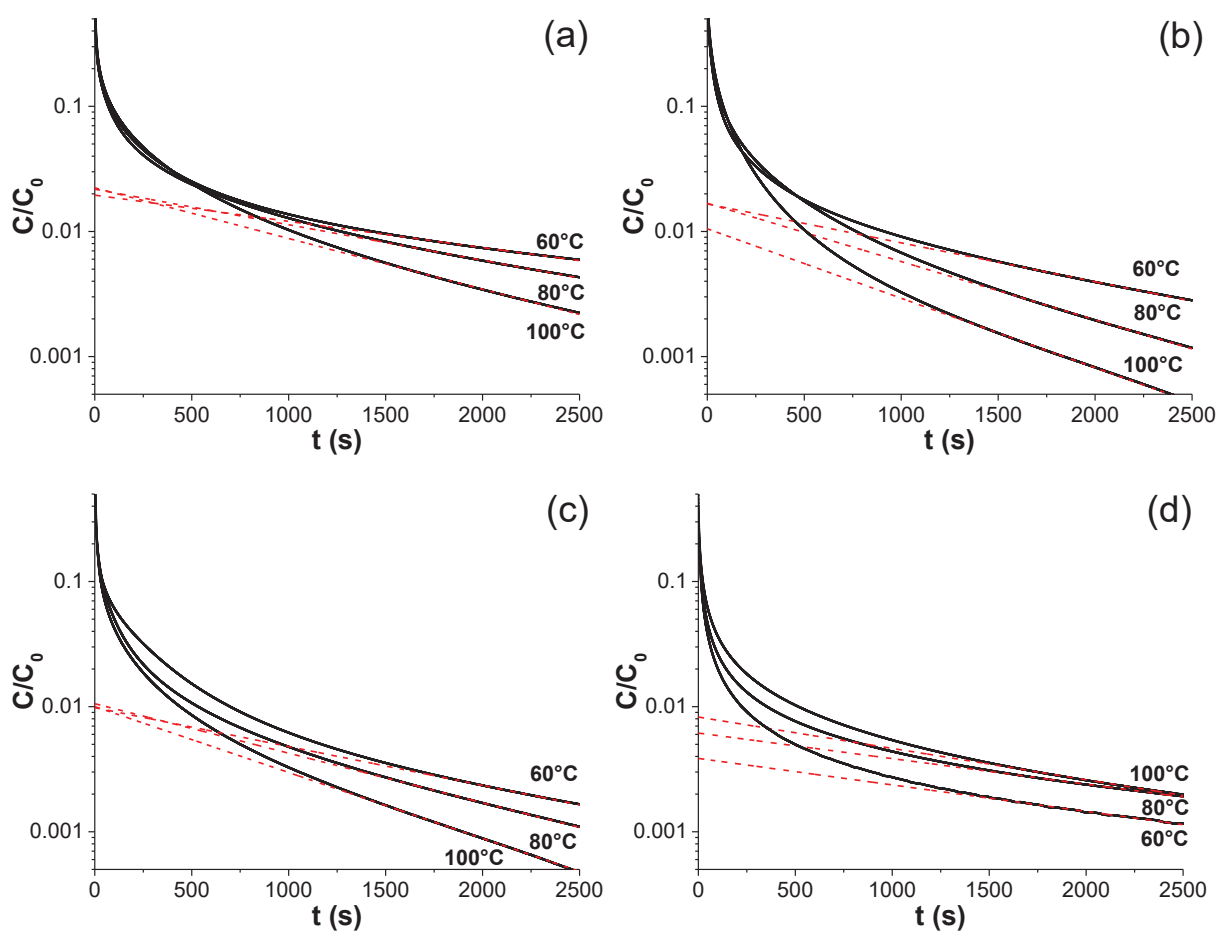


**Figure 8:** Experimental  $Ft$  plot of Na-USY-0 at 60°C with 0.05 kPa of mesitylene in nitrogen and purge flow rates of 50 and 100 mL/min.

## 3.2.2 ZLC results

Since the kinetic-controlled regime for desorption of mesitylene from Na-USY-0 with 100 mL/min purge flow was confirmed, the following exposed measurements have been carried out by keeping this purge flow.

Mesitylene has been adsorbed at 60, 80 and 100°C on the Na-USY-0, Na-USY-1, Na-USY-2, Na-Y samples, as well as an empty reactor, for 1h. Figure 9 displays the relative concentration  $C/C_0$  of mesitylene at the outlet of the reactor against the time of desorption. As expected, for Na-USY-0, Na-USY-1 and Na-USY-2, the slopes of the long-time asymptote decrease when the temperatures increase. It means that the coefficient  $D/R^2$  increases with temperature. However, such behaviour is not observed for the Na-Y sample where the slopes are constant for the three temperatures (Figure 9-d), giving the impression that mesitylene does not diffuse through the entire crystals of Na-Y zeolite. To confirm or infirm this point, a comparison of the amount of mesitylene desorbed during the ZLC measurements and the amount of mesitylene adsorbed at the equilibrium during an isotherm measurement has been made.



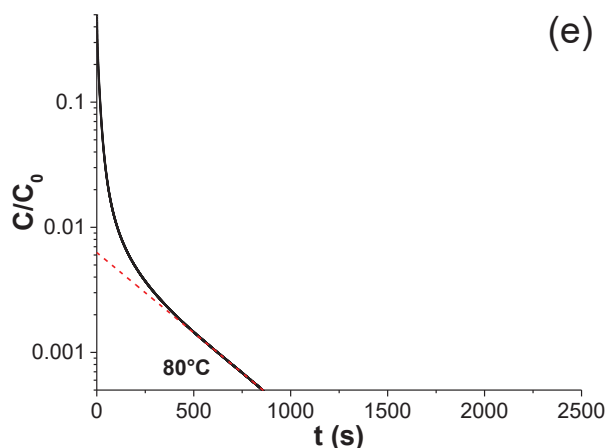


**Figure 9.** ZLC response curves for mesitylene in (a) Na-USY-0, (b) Na-USY-1, (c) Na-USY-2, (d) Na-Y and (e) empty reactor at various temperatures. Red dotted lines correspond to the long-time asymptotes.

Under the experimental conditions, the flow rate of mesitylene during the adsorption phase is  $1.76 \mu\text{mol} \cdot \text{min}^{-1}$ . Considering this value as the mesitylene flow rate at the beginning of the desorption phase - at  $C/C_0 = 1$  - it is possible to plot the amount of mesitylene desorbed against the time of desorption (Figure 10). The area integration under these curves gives us the amount of mesitylene desorbed during the experiments. Since ZLC measurements are carried out with 1.7 mg of catalyst, the amount of mesitylene that is desorbed per gram of Na-USY-0, Na-USY-1, Na-USY-2 and Na-Y are 0.80, 0.61, 0.35 and  $0.16 \text{ mmol} \cdot \text{g}^{-1}$ , respectively (Table 7). These values are obtained after subtraction of the amount desorbed from the empty reactor.

It is interesting to compare these quantities to the ones obtained from the adsorption isotherms recorded at the equilibrium on the BELMAX Japan setup (Figure 11). From isotherm measurements, the amounts of mesitylene adsorbed at 0.05 kPa, which is the partial pressure used for ZLC measurements, are 1.10, 0.81, 0.52 and  $0.92 \text{ mmol} \cdot \text{g}^{-1}$  for Na-USY-0, Na-USY-1, Na-USY-2 and Na-Y, respectively. For the first three samples, the amount of mesitylene desorbed during ZLC measurements at  $80^\circ\text{C}$  represents between 68 and 75% of the amount calculated at the equilibrium. These percentages are probably underestimated since the switch from the adsorption to the desorption lines disturbs the FID signal during the first two seconds of desorption. Hence, the quantities of mesitylene obtained from ZLC measurements are in good agreement with those predicted from the adsorption isotherms for samples Na-USY-0, Na-USY-1 and Na-USY-2. However, the Na-Y sample differs from the others, with less than 20% of correspondence between the two measurements. The ZLC response curves obtained for this sample, and the  $D/R^2$  coefficients calculated from the long-time asymptotes, cannot correspond to the diffusion of the molecule through the entire crystal. Looking at the Figure 5, we can see that the H-Y sample contains a high

amount of extra framework species. We can assume that is also the case for Na-Y sample, which is obtained from H-Y by ion exchange. It is difficult to say whether these species are in the porosity or not, but it seems reasonable to assume that they may partly block the accessibility to large molecules such as mesitylene, even though they do not significantly modify the amount of N<sub>2</sub> adsorbed.

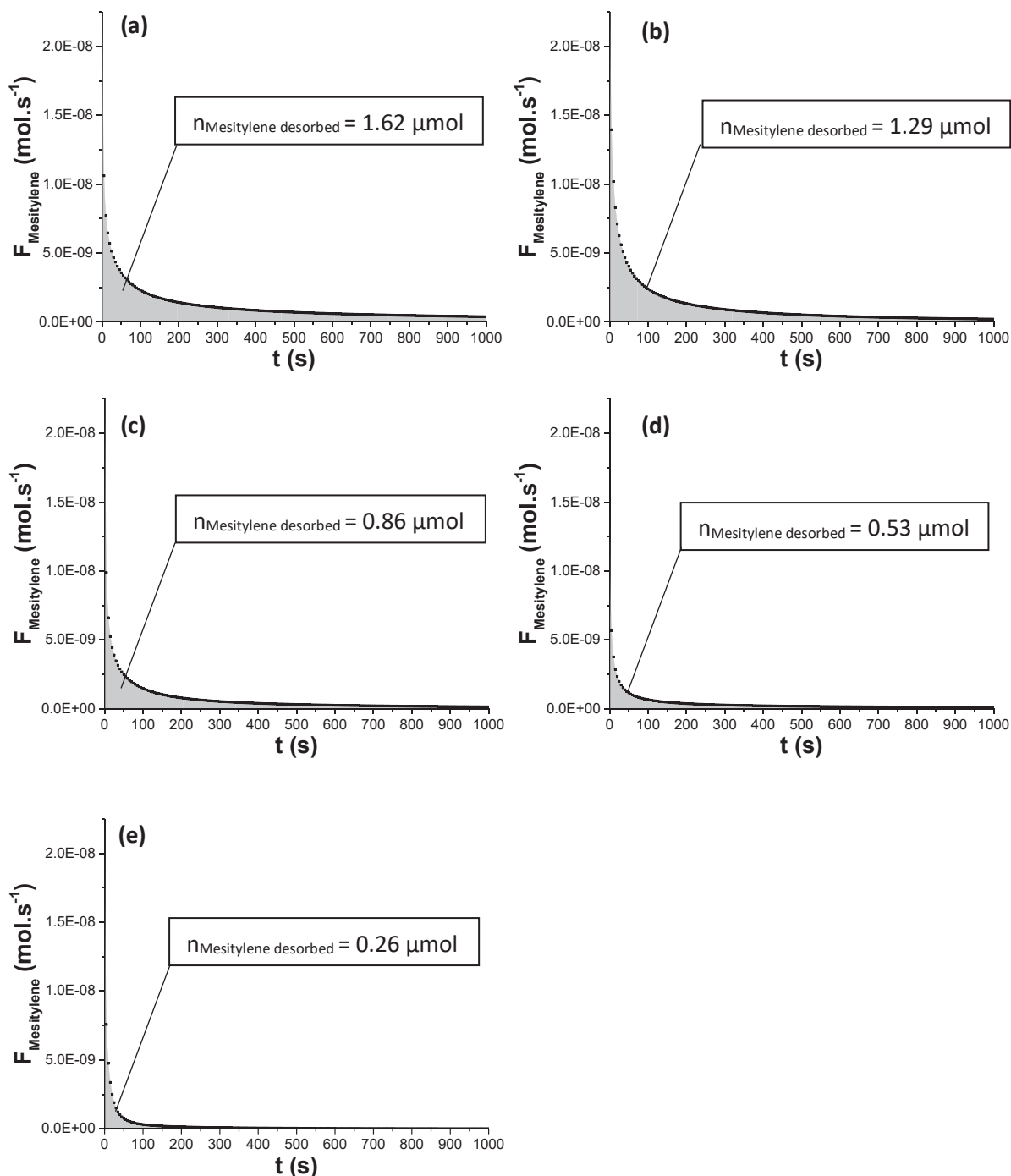


**Figure 10.** Flow of mesitylene desorbed during the desorption phase at 80°C as a function of the time for experiments carried out with (a) Na-USY-0, (b) Na-USY-1, (c) Na-USY-2, (d) Na-Y and (e) an empty reactor. The surrounded boxes correspond to the number of moles of mesitylene desorbed during 2.5h and calculated from the integration of the curves.

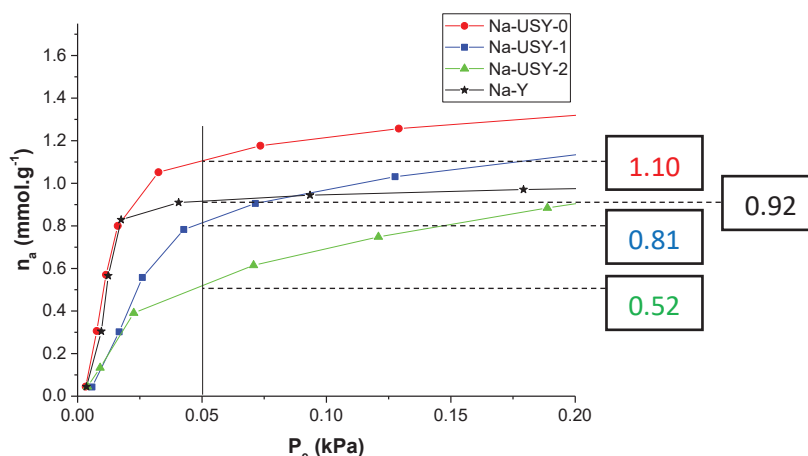


**Figure 11.** Mesitylene adsorption isotherms recorded on Belmax Japan setup at 80°C.

**Table 7.** Comparison between ZLC and isotherm measurements.

Sample	Amount of mesitylene...	
	...desorbed from ZLC measurements [mmol.g <sup>-1</sup> ]	...adsorbed from isotherm measurements [mmol.g <sup>-1</sup> ]
Na-USY-0	0.80	1.10
Na-USY-1	0.61	0.81
Na-USY-2	0.35	0.52
Na-Y	0.16	0.92

### 3.2.3 Variation of D and R coefficients

Table 8 displays the  $D/R^2$  coefficients obtained for the investigated samples at three temperatures. The  $D/R^2$  coefficients obtained for the hierarchical materials are slightly higher than for the parent Na-USY-0. However, the order of difference is not as large as expected. An order of 1.5 between the values from the hierarchical materials and the parent is observed.

There is two ways to interpret these results. Either we can consider that the radius  $R$  of the sorbent particle is constant for the three Na-USY-0, Na-USY-1 and Na-USY-2 materials. In this case, the measured diffusion is an effective coefficient ( $D_{\text{eff}}$ ) which integrates diffusion in micro and mesoporous domains. Considering for example the results at 100°C:

$$D_1 = 1.35 \times D_0 \text{ and } D_2 = 1.28 \times D_0$$

Where:  $D_0$ ,  $D_1$  and  $D_2$  are the diffusion coefficients within Na-USY-0, Na-USY-1 and Na-USY-2, respectively.

This would mean that the effective diffusion of mesitylene is slightly improved for both hierarchical materials in comparison with the parent one.

Another way to consider the results is that the measured diffusion from the experiments is the diffusion within the micropores, which is constant and non-intrinsic to the materials. In this case, the  $R$  coefficient would correspond to the mean distance between mesopores, which corresponds to the characteristic size of the microporous domain. At 100°C, this consideration leads to:

$$R_1 = 0.86 \times R_0 \text{ and } R_2 = 0.88 \times R_0$$

Where:  $R_0$ ,  $R_1$  and  $R_2$  are the mean distances between mesopores within Na-USY-0, Na-USY-1 and Na-USY-2, respectively.

These results are coherent with the creation of the extra mesoporous network for hierarchical samples. However, both hierarchical Na-USY-1 and Na-USY-2 materials seem to lead at similar diffusion coefficients, no matter the amount of mesoporosity introduced into the parent material. In the literature, Zaman et al. reported a  $D/R^2$  coefficient of  $8.22\text{E-}05 \text{ s}^{-1}$  for the kinetic desorption of 1,3-diisopropylbenzene from NaY zeolite at 150°C [16]. Kaliaguine et al. obtained  $D/R^2$  of  $3.45\text{E-}04 \text{ s}^{-1}$  for the kinetic desorption of mesitylene from mesostructured SBA-16, having a total pore volume of  $0.42 \text{ cm}^3.\text{g}^{-1}$  and mesopores diameter of 9.15 nm, at 90°C [19]. The values from  $7.3\text{E-}05$  to  $1.24\text{E-}04 \text{ s}^{-1}$  we obtained for mesoporous NaY zeolite, having mesopore diameter of 4-5nm, do not appear absurd regarding the comparable published results. Activation energies ( $E_a$ ) between 14 and 17 kJ/mol, calculated with the Arrhenius plot, are also in line with what can be expected for the diffusion of mesitylene in the investigated materials.

**Table 8:** Diffusivity values obtained from the ZLC method with mesitylene.

Catalyst	Temperature (°C)	$D/R^2 \times 10^4 \text{ (s}^{-1}\text{)}$	$E_a \text{ (kJ/mol)}$
Na-USY-0	60	0.50	17
	80	0.68	
	100	0.97	
Na-USY-1	60	0.74	15

	80	1.10	
	100	1.31	
Na-USY-2	60	0.73	14
	80	0.93	
	100	1.24	
Na-Y	60	0.50	-
	80	0.48	
	100	0.59	

## 4 Conclusion

The objective of this chapter is to describe in detail the preparation of the zeolites used for the catalytic testing that follows, as well as to identify their physical and chemical differences. To do so, four materials were chosen. Two of the materials were commercial Y zeolites, labelled as H-Y and H-USY-Y. The two others were hierarchical Y zeolites, obtained from surfactant-templated crystal rearrangement of the H-USY-0 sample, labelled as H-USY-1 and H-USY-2.

These four materials cover a large range of porosity:

- H-Y has mainly micropores.
- H-USY-0 has closed mesopores communicating with the crystal surface via micropores. Some large fractures at the crystal surface are also assimilated to mesopores.
- H-USY-1 has a combination of micropores and totally opened mesopores with a diameter of 3-5 nm.
- H-USY-2 is similar to the H-USY-1 sample but with a higher proportion of mesopores and fewer micropores.

The creation of the newly mesoporous network was associated with a loss of structural aluminium (XRD/ICP-OES), leading to an increase of the extra framework aluminium species, as it has been confirmed by  $^{27}\text{Al}$  NMR. As seen in the mass transfer study of mesitylene, carried out with the zero-length column method, the diffusion within the materials was slightly improved for the two hierarchical Y zeolites. A factor of 1.5 between the values for hierarchical H-USY-1 and H-USY-2 zeolites and the parent H-USY-0 was observed.



### References for Chapter III

- [1] E. T. C. Vogt and B. M. Weckhuysen, “Fluid catalytic cracking: recent developments on the grand old lady of zeolite catalysis,” *Chem. Soc. Rev.* *Chem. Soc. Rev.*, vol. 7342, no. 44, pp. 7342–7370, 2015, doi: 10.1039/c5cs00376h.
- [2] “Zeolite Y - Zeolyst.” [Online]. Available: <https://www.zeolyst.com/our-products/standard-zeolite-powders/zeolite-y.html>.
- [3] K. Li, J. Valla, and J. Garcia-Martinez, “Realizing the commercial potential of hierarchical zeolites: New opportunities in catalytic cracking,” *ChemCatChem*. 2014, doi: 10.1002/cctc.201300345.
- [4] J. Garcia-Martinez, M. Johnson, J. Valla, K. Li, and J. Y. Ying, “Mesostructured zeolite Y—high hydrothermal stability and superior FCC catalytic performance,” *Catal. Sci. Technol. Catal. Sci. Technol.*, vol. 2, no. 2, pp. 987–994, 2012, doi: 10.1039/c2cy00309k.
- [5] R. Chal, T. Cacciaguerra, S. van Donk, and C. Gérardin, “Pseudomorphic synthesis of mesoporous zeolite Y crystals,” *Chem. Commun.*, vol. 46, no. 41, p. 7840, 2010, doi: 10.1039/c0cc02073g.
- [6] W. Schwieger *et al.*, “Hierarchy concepts: classification and preparation strategies for zeolite containing materials with hierarchical porosity,” *Chem. Soc. Rev.*, vol. 45, no. 12, pp. 3305–3566, 2016, doi: 10.1039/C5CS00599J.
- [7] M. Thommes *et al.*, “Physisorption of gases, with special reference to the evaluation of surface area and pore size distribution (IUPAC Technical Report),” *Pure Appl. Chem.*, vol. 87, no. 9–10, pp. 1051–1069, 2015, doi: 10.1515/pac-2014-1117.
- [8] J. Landers, G. Y. Gor, and A. V. Neimark, “Density functional theory methods for characterization of porous materials,” *Colloids Surfaces A Physicochem. Eng. Asp.*, vol. 437, pp. 3–32, 2013, doi: 10.1016/j.colsurfa.2013.01.007.
- [9] F. J. Sotomayor, K. A. Cychosz, and M. Thommes, “Characterization of Micro/Mesoporous Materials by Physisorption : Concepts and Case Studies,” *Acc. Mater. Surf. Res.*, vol. 3, no. 2, pp. 34–50, 2018.
- [10] W. Lutz, “Zeolite Y: Synthesis, modification, and properties - A case revisited,” *Adv. Mater. Sci. Eng.*, vol. 2014, 2014, doi: 10.1155/2014/724248.
- [11] S. Mitchell *et al.*, “Aluminum Redistribution during the Preparation of Hierarchical Zeolites by

- Desilication," *Chem. - A Eur. J.*, vol. 21, no. 40, pp. 14156–14164, 2015, doi: 10.1002/chem.201500992.
- [12] M. Gackowski, Ł. Kuterasi, J. Podobinski, B. Sulikowski, and J. Datka, "IR and NMR studies of hierarchical material obtained by the treatment of zeolite Y by ammonia solution," *Spectrochim. Acta Part A Mol. Biomol. Spectrosc.*, vol. 193, pp. 440–446, 2018, doi: 10.1016/j.saa.2017.12.042.
- [13] M. Eic and D. M. Ruthven, "Diffusion of linear paraffins and cyclohexane in NaX and 5A zeolite crystals," *Zeolites*, vol. 8, no. 6, pp. 472–479, 1988, doi: 10.1016/S0144-2449(88)80223-9.
- [14] C. L. Cavalcante, N. M. Silva, E. F. Souza-Aguiar, and E. V. Sobrinho, "Diffusion of paraffins in dealuminated Y mesoporous molecular sieve," *Adsorption*, vol. 9, no. 3, pp. 205–212, 2003, doi: 10.1023/A:1024793615830.
- [15] S. F. Zaman, K. F. Loughlin, and S. S. Al-Khattaf, "Kinetics of desorption of 1,3-diisopropylbenzene and 1,3,5-triisopropylbenzene. 1. Diffusion in Y-zeolite crystals by the zero-length-column method," *Ind. Eng. Chem. Res.*, vol. 44, no. 7, pp. 2027–2035, 2005, doi: 10.1021/ie049095u.
- [16] S. F. Zaman, K. F. Loughlin, and S. A. Al-Khattaf, "Kinetics of desorption of 1,3-diisopropylbenzene and 1,3,5-triisopropylbenzene. 2. Diffusion in FCC catalyst particles by zero length column method," *Ind. Eng. Chem. Res.*, vol. 54, no. 16, pp. 4572–4580, 2015, doi: 10.1021/ie504963e.
- [17] D. M. Ruthven and B. K. Kaul, "Adsorption of Aromatic Hydrocarbons in NaX Zeolite. 2. Kinetics," *Ind. Eng. Chem. Res.*, vol. 32, no. 9, pp. 2053–2057, 1993, doi: 10.1021/ie00021a029.
- [18] K. F. Loughlin, S. S. Al-Khattaf, and S. F. Zaman, "Kinetics of sorption of 1,3 di-isopropyl benzene and 1,3,5 tri-isopropyl benzene in nay crystals, alumina matrix and FCC catalyst particles by zero length column method," *AIChE Annu. Meet. Conf. Proc.*, pp. 1–20, 2005.
- [19] O. C. Gobin, Q. Huang, H. Vinh-Thang, F. Kleitz, M. Eić, and S. Kaliaguine, "Mesostructured silica SBA-16 with tailored intrawall porosity part 2: Diffusion," *J. Phys. Chem. C*, vol. 111, no. 7, pp. 3059–3065, 2007, doi: 10.1021/jp063583t.
- [20] Q. Huang, M. Eić, H. Xiao, and S. Kaliaguine, "Characterization of the diffusion path in micro- and meso-porous materials from ZLC analysis," *Adsorption*, vol. 16, no. 6, pp. 531–539, 2010, doi: 10.1007/s10450-010-9258-6.

- [21] J. Kärger, D. M. Ruthven, and D. N. Theodorou, *Diffusion in Nanoporous Materials*. 2012.
- [22] X. Hu, E. Mangano, D. Friedrich, H. Ahn, and S. Brandani, "Diffusion mechanism of CO<sub>2</sub> in 13X zeolite beads," *Adsorption*, vol. 20, no. 1, pp. 121–135, 2014, doi: 10.1007/s10450-013-9554-z.
- [23] S. Brandani, "A Simple Graphical Check of Consistency for Zero Length Column Desorption Curves," *Chem. Eng. Technol.*, vol. 39, no. 6, pp. 1194–1198, 2016, doi: 10.1002/ceat.201500634.

# Chapter IV: Catalytic cracking of n-hexane over hierarchical Y zeolites

---

## 1. Acidity measurements using infrared study of pyridine adsorbed

Characterisation and quantification of zeolite acidity is particularly relevant for the understanding and interpretation of the catalytic cracking reactions they are used for. Among the experimental methods to determine the acidity of the zeolites, infrared spectroscopy analysis of a basic probe molecule, allows to quantify and discriminate the type of acid sites. The choice of the pyridine as probe molecule is interesting since it interacts with Brønsted acid sites to create pyridinium ion and adsorbs on Lewis acid sites. Both acid sites are distinguishable by IR adsorption bands at  $1545\text{ cm}^{-1}$  and  $1455\text{ cm}^{-1}$ , respectively.

### 1.1 Quantification of the acid sites

#### 1.1.1 Pyridine adsorption

Figure 1 displays the IR spectra of pyridine adsorbed onto the four materials at different temperatures. The adsorption bands at  $1455$  and  $1545\text{ cm}^{-1}$  are due to the adsorption of pyridine and pyridinium ion, respectively. The integration of these two bands allows the calculation of the Lewis and Brønsted acid sites. The variation of their concentration as a function of the temperature can be interpreted as the strength of the various acid sites.

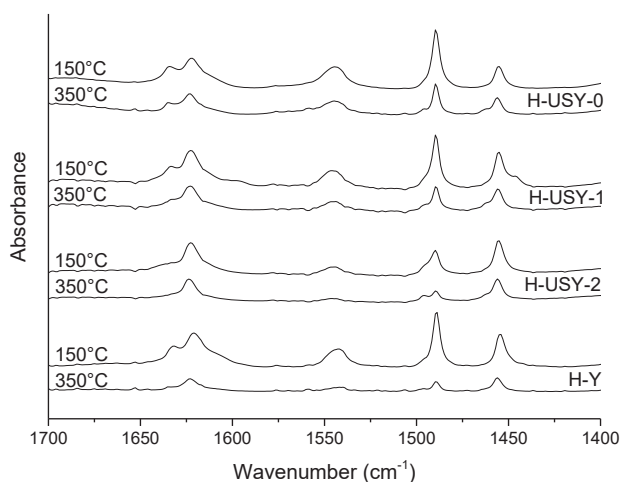


**Figure 1.** IR difference spectra after pyridine adsorption on zeolite samples, followed by outgassing at increasing temperatures.

Table 1 displays the quantification of the Brønsted ( $1545\text{ cm}^{-1}$ ) and Lewis ( $1455\text{ cm}^{-1}$ ) acid sites calculated from the IR spectra obtained at  $150^\circ\text{C}$ . The hierarchical H-USY-1 and H-USY-2 materials exhibit a lower concentration of Brønsted acid site (BAS) and a higher concentration of Lewis acid sites (LAS) than the parent H-USY-0. This can be explained by the formation of EFAL during the material preparation. This has been previously confirmed with  $^{27}\text{Al}$  NMR, as well as differences between bulk and structural Si/Al ratios (see Chapter III, Part 2.4 & 2.5). The H-Y sample exhibits a high LAS concentration too. This sample has a BAS concentration in the same range as H-USY-1, which is lower than H-USY-0. This H-Y sample, which is the Y-zeolite CBV400 produced by Zeolyst, is the only investigated material having a Si/Al ratio of 2.5. Its acidity was expected to be higher than other materials, but the relatively high  $\text{Na}^+$  concentration decreases the number of BAS that could be obtained with a sample completely free of  $\text{Na}^+$ .

**Table 1.** Number of acid sites according to FT-IR study of pyridine adsorbed, and Si/Al ratio found in Chapter III.

Catalysts	Na (wt. %)	Si/Al (molar ratio) <i>From ICP-OES</i>	Si/Al (molar ratio) <i>From XRD</i>	Pyridine FT-IR ( $\text{mmol.g}^{-1}$ )	
				BAS	LAS
H-USY-0	0.02	14.8	13.6	0.28	0.10
H-USY-1	0.05	14.4	18.6	0.23	0.16
H-USY-2	0.02	14.1	29.0	0.13	0.18
H-Y	1.6	2.5	2.9	0.23	0.18

### 1.1.2 Hydroxyl groups

The frequency of the stretching vibration of the hydroxyl groups depends on the strength of the O-H bond [1]. The wavenumber of the O-H stretching vibration is a function of the type of coordination of the oxygen (terminal or bridging), the structural environment (the type of zeolite), and the perturbation of the OH group through the surroundings by lattice or extra-lattice oxygen. The higher the  $\nu(\text{OH})$ , the stronger the O-H bond, i.e. the lower is the strength of the Brønsted acid site [2].

The IR analysis of H-USY-0, H-USY-1, and H-USY-2 after desorption for one night at  $450^\circ\text{C}$  reveals three peaks in the  $3400\text{--}3800\text{ cm}^{-1}$  area (Figure 2). The peak at  $3745\text{ cm}^{-1}$  corresponds to the terminal silanol groups. The peaks at  $3565$  and  $3630\text{ cm}^{-1}$  corresponds to the Brønsted sites hosted in the sodalite cage and the supercage of the Y zeolite, respectively. On H-Y material, the peak at  $3745\text{ cm}^{-1}$

corresponding at the terminal silanol groups is also observed. However, the intensity of this peak is lower than for the other catalysts. The two other peaks observed, at 3600 and 3694  $\text{cm}^{-1}$  correspond to the bridging hydroxyl groups in sodalite cages and supercages, respectively. Due to the low Si/Al ratio, the relative ratio between the intensities of the IR bands of the external silanols and the Brønsted sites is lower than other materials. However, the higher frequencies of the bridging hydroxyl groups for the H-Y materials seem to indicate a lower acidic strength of these Brønsted acid sites.

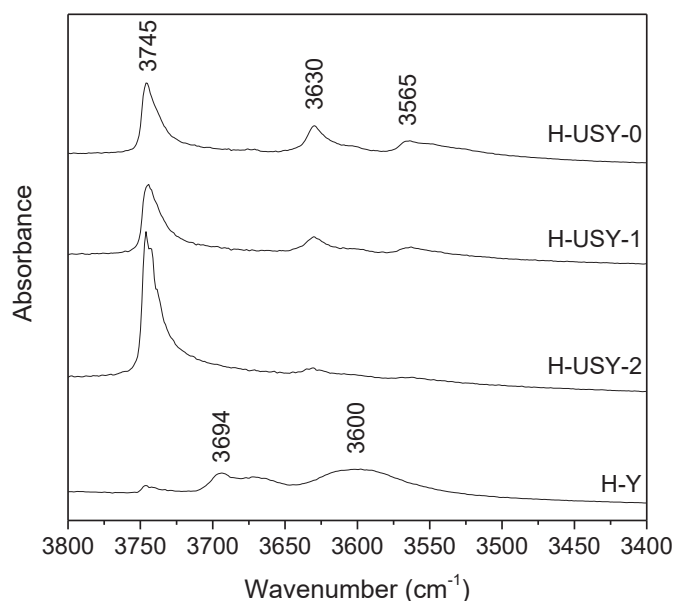


**Figure 2.** FT-IR spectra of the zeolite samples after activation by outgassing at 450°C for 1 night.

### 1.2 Strength of the acid sites

For the strong Lewis and Brønsted acid sites, the pyridine and pyridinium ion stay adsorbed at high desorption temperatures. The relative decrease of the number of the BAS and LAS with the increase of the desorption temperature is a tool for the evaluation of the acid strength. Figure 3 displays the relative concentration of acid sites from 150 to 450°C. At 450°C, almost all pyridinium ions are desorbed from the BAS of the four materials. However, the residual concentration of BAS at 250°C and 350°C differs from the H-USY series and the H-Y sample. For H-Y, the acid strength of the BAS seems weaker than the three other materials. This was previously suggested by the higher peak frequency of the hydroxyl bridging groups of H-Y. In smaller proportion, a similar trend is observed for LAS.

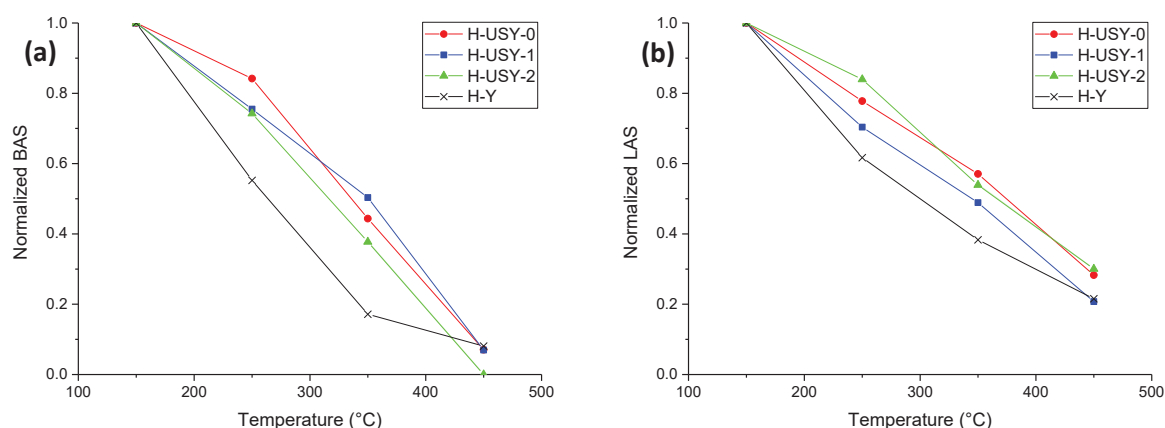


**Figure 3.** Normalized area relative to (a) Brønsted and (b) Lewis acid sites as a function of the outgassing temperature.

## 2. Catalytic cracking of n-hexane

### 2.1 Preliminary check: the deactivation of the catalyst.

N-hexane cracking has been studied as model reaction in order to characterize the acidity of the H-USY-0, H-USY-1, H-USY-2, and H-Y catalysts in absence of diffusion limitations.

To identify any deactivation during the tests, reaction at 550°C, 575°C, 600°C and 650°C are carried out with a time on stream superior at 40 min. A GC analysis is performed every four minutes to determine the gas flow composition at the outlet of reactor. Figure 4 displays the flow of n-hexane within the effluent gas as a function of the time. The n-hexane, initially bypassing the reactor, goes through the catalytic bed at  $t = 0$  min (see Chapter II, Figure 5). For the catalysts H-USY-0 and H-USY-1, a clear increase of the amount of n-hexane within the gas flow during the reaction at 650°C indicates a deactivation of the catalyst. A similar observation can be made at 600°C for H-USY-0. For the tests performed at 550°C and 575°C, the amount of n-hexane – and so the conversion – seems constant for the length of tests. For the catalyst H-USY-2, no deactivation seems to appear for the length of the test. Regarding the microporous H-Y material, a decrease of the hexane flow is observed. This could either be a time required for this catalyst to activate, or an artefact due to issue with the inlet flow of n-hexane.

The very high temperatures tend to deactivate the catalysts showing the highest initial conversions – H-USY-0 and H-USY-1. Since the purpose of these tests is to study the catalytic sites of the four materials, the considered results for the comparison of the samples are the ones obtained during the first minutes of the test.

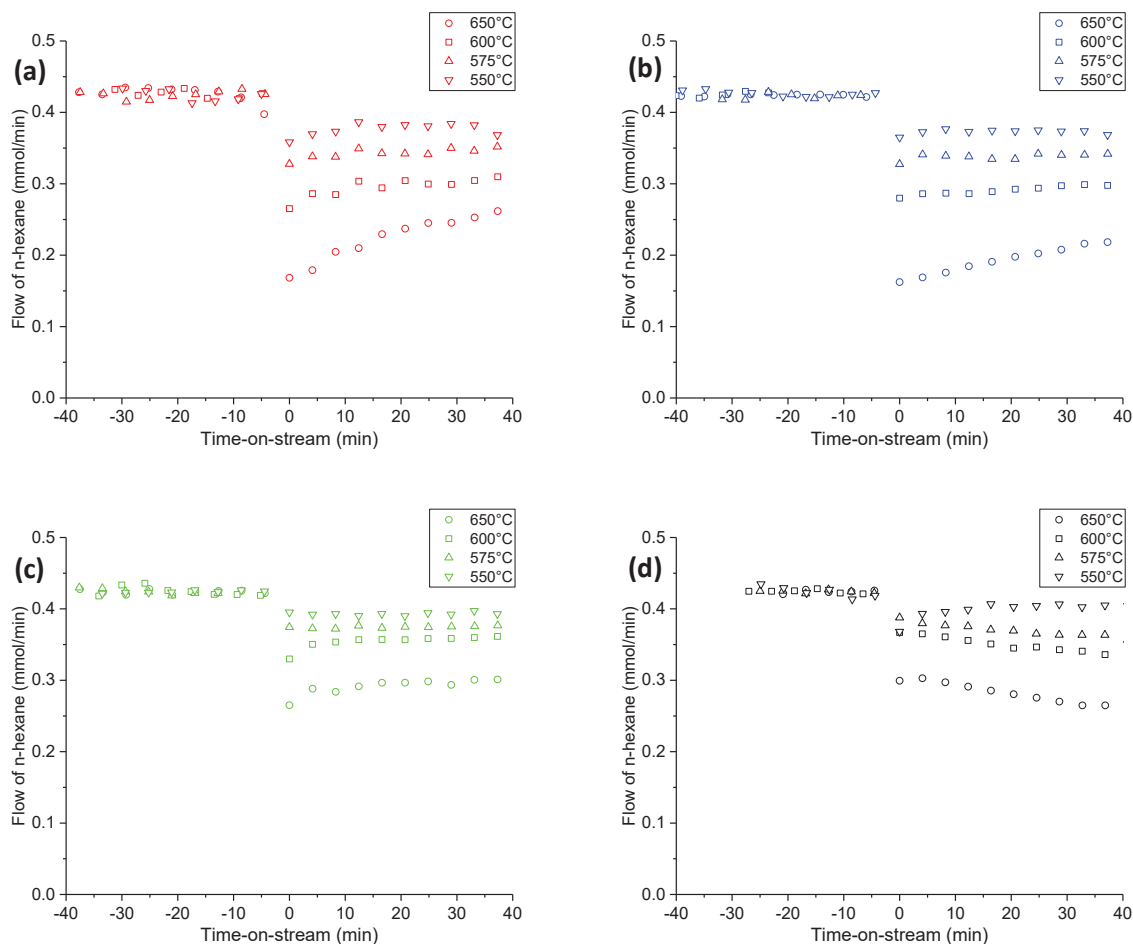


**Figure 4.** The flow of n-hexane during n-hexane cracking reactions carried out on (a) H-USY-0, (b) H-USY-1, (c) H-USY-2 and (d) H-Y at 550, 575, 600 and 650°C.

At each temperature modification, the catalysts are regenerated by a 30 min oxidation step where a flow of air goes through the catalytic bed at 650°C. In this way, the coke formed during the cracking reactions is burned out from the catalysts. Aiming to avoid the comparison of completely fresh and spent catalyst, a first cracking test at 650°C, followed by a regeneration at the same temperature, was performed on each material before the presented cracking results at 550°C, 575°C, 600°C, 650°C.

## 2.2 Conversion

The n-hexane conversion for the tests carried out with the four materials is calculated as follow:

$$Conversion (\%) = \frac{F_{n-C6,0} - F_{n-C6,reactor}}{F_{n-C6,0}} \times 100 \quad (16)$$

Where:  $F_{n-C6,0}$  is the flow of n-hexane going through the bypass before the switch of the valve.



$F_{n-C6,reactor}$  is the outlet flow of n-hexane leaving the reactor, in  $\text{mmol} \cdot \text{min}^{-1}$ .

Working with a Coriolis mass flow meter set up at  $2.2 \text{ g} \cdot \text{h}^{-1}$ ,  $F_{n-C6,0}$  is considered equal to  $0.43 \text{ mmol} \cdot \text{min}^{-1}$ . The outlet flow of n-hexane is obtained from the GC analysis, where the product concentration (in mol.%) is converted into molar flow thanks to the constant concentration of nitrogen during the entire test.

Similarly to the Figure 4, the plot of the n-hexane conversion as a function of the time-on-stream (Figure 5) exhibits the deactivation of the catalysts H-USY-0 and H-USY-1 at  $650^\circ\text{C}$ . When the initial conversion is lower than around 30%, the conversion rate stays mostly constant during the length of the tests.

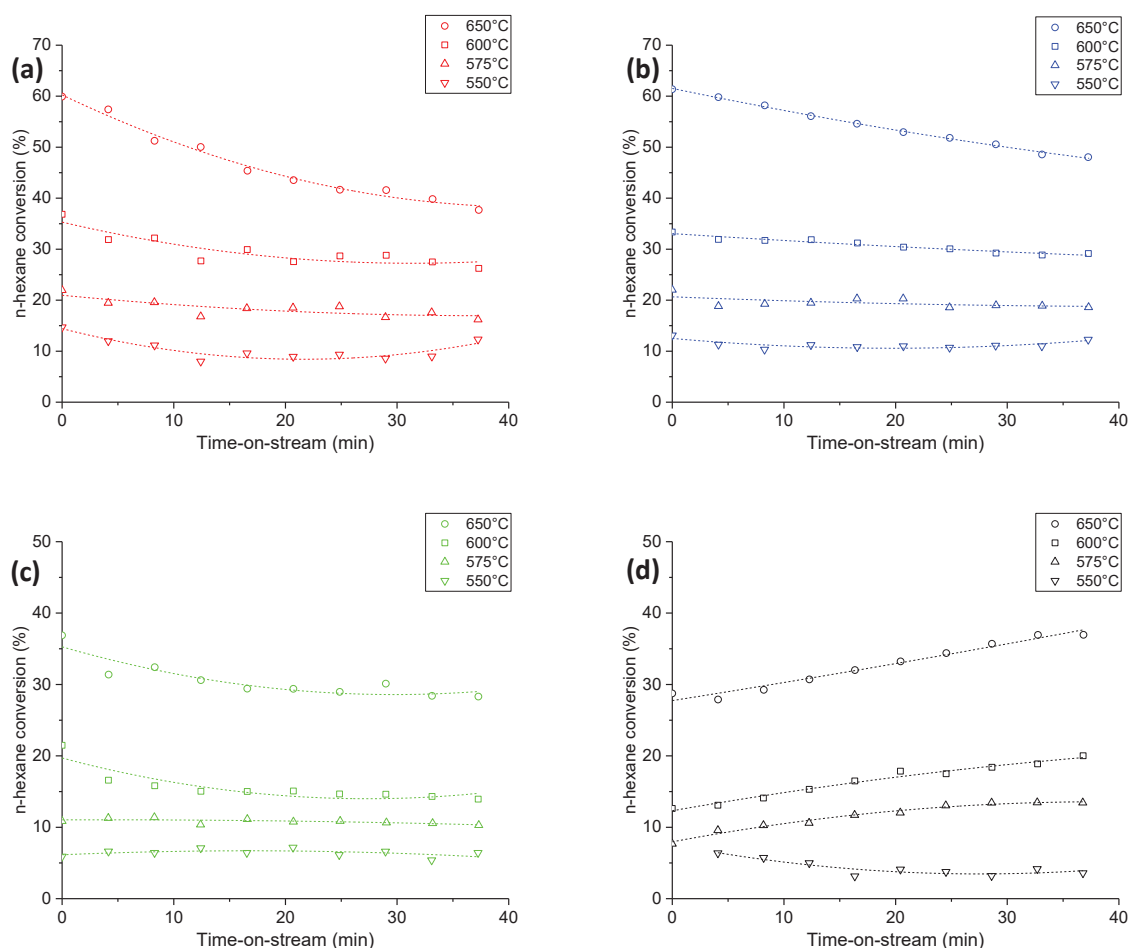


**Figure 5.** Conversion of n-hexane on (a) H-USY-0, (b) H-USY-1, (c) H-USY-2 and (d) H-Y at 550, 575, 600 and  $650^\circ\text{C}$ . Reaction conditions: catalyst  $0.1\text{g}$ ;  $P_{n\text{-hexane}} = 9 \text{ kPa}$ ;  $W/F_{n\text{-hexane}} = 3.9 \text{ g}_{cat} \cdot \text{h} \cdot \text{mol}_{n\text{-hexane}}^{-1}$ ; temperature  $550\text{-}650^\circ\text{C}$ .

### 2.3 Cracking performance as a function of the acid site concentration

To compare the catalytic activity of the four materials, the conversion obtained with each catalyst is divided per the number of acid sites. According to the literature, such a hydrocarbon cracking reaction depends only on the number of Brønsted acid sites. To prove it, Jolly et al. showed that the specific poisoning of the Brønsted acid site of dealuminated HY zeolites with 2,6-lutidine leads to an absence of activity regarding the n-hexane cracking reaction [3]. Thus, the turnover frequency (TOF) of each catalyst is calculated considering the number of Brønsted acid sites previously determined from FT-IR study of adsorption of pyridine:

$$TOF = \frac{Conversion \times F_{n-C6,0}}{N_{BAS} \times W} \quad (17)$$

Where:  $N_{BAS}$  is the number of Brønsted acid sites, in  $mmol.g^{-1}$ .

$W$  is the mass of catalyst used for the experiments, which is 0.1 g.

As previously observed, the conversion may not be constant over the time-on-stream at high temperatures. To compare the activity of each sample, the initial conversion - before deactivation of the catalyst - is considered for the calculation of the TOF. The initial conversions are obtained by fitting a polynomial curve on the experimental data displayed in Figure 5, then taking the values at  $t = 0s$ . These data are reported in Table 2.

**Table 2.** Initial conversions for the catalytic cracking of n-hexane over H-USY-0, H-USY-1, H-USY-2 and H-Y at 550, 575, 600 and 650°C.

Temperature (°C)	Conversion (%)			
	H-USY-0	H-USY-1	H-USY-2	H-Y
550	14.4	12.5	6.1	7.6
575	21.0	20.7	11.0	8.0
600	35.3	33.1	19.7	12.3
650	60.3	61.5	35.3	27.7

The evolution of the TOF as a function of the temperature is shown in Figure 6. The H-Y sample shows a significant lower TOF than the three other samples. The hierarchical material H-USY-1 and H-USY-2 exhibit a similar activity, which is slightly higher than the one from H-USY-0. Even if n-hexane is

a small molecule with a kinetic diameter of 0.43 nm, it seems that diffusion limitation may affect the activity. Another reason that may explain the difference of TOF is the strength of the BAS. The sample H-Y exhibits the lowest activity of the four materials tested. Besides having the lowest volume of mesopore, it is also the sample with the lowest BAS strength, as depicted in the part 1.2. Lower BAS strength can reduce the ability of the acid site to protonate the C-C bond of the hydrocarbon, which is the initial step for the cracking mechanism of small alkane [4].

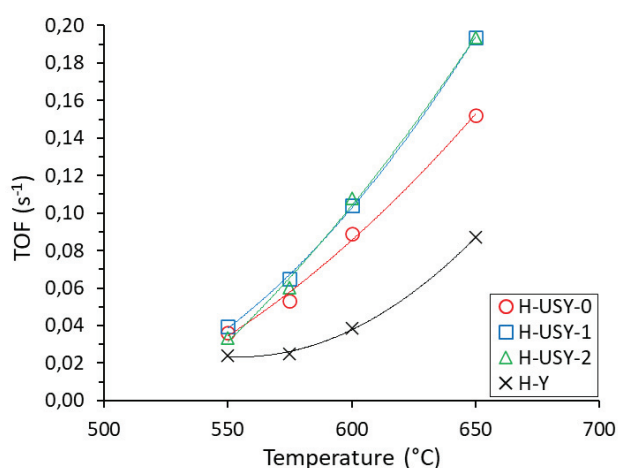


**Figure 6.** Turnover frequency per Brønsted acid sites for the catalytic cracking of n-hexane over y zeolites.

### 2.4 Selectivity

It is possible to discriminate the products formed during the reaction with a calibration of the  $C_1$  to  $C_6$  hydrocarbon compounds. On the GC setup, the identification and quantification of the following products have been done: hydrogen, methane, ethane, ethylene, propane, propene,  $C_4$  (n-butane, isobutane),  $C_4^=$  (but-1-ene, isobutylene, cis and trans-but-2-ene),  $C_5$  (n-pentane, isopentane),  $C_5^=$  (pent-1-ene, 2-methylbut-2-ene, cis and trans-pent-2-ene),  $C_6$  (2-methylpentane, 3-methylpentane), benzene. As previously seen, the reactions performed at temperatures above 600°C show deactivation occurring during the experiment. To compare the selectivity at these temperatures, the initial data are considered. The selectivity values are calculated by considering the identified compounds. For example, the coke formed during the process is not considered in the calculation.

$$S_A = \frac{F_A}{\sum F_i} \times 100 \quad (18)$$

Where:  $S_A$  is the molar selectivity of product A, in %.

$F_A$  is the molar flow of the product A, in  $\text{mol} \cdot \text{min}^{-1}$ .

$\sum F_i$  is the sum of all reaction products formed from n-hexane conversion, in  $\text{mol} \cdot \text{min}^{-1}$ .

### 2.4.1 Selectivity as a function of the temperature

Figure 7 displays the selectivity for each product or group of products as a function of the reaction temperature. The selectivity values for the  $C_5$ ,  $C_5^-$ ,  $C_6$  and benzene are lower than 1%. For a clarity purpose they are not displayed. The main reaction product obtained with the four catalysts is propylene. Regardless of the reaction temperature, or the n-hexane conversion, propylene accounts for between 35% and 40% of the products of reaction. For the other reaction products, only slight differences appear depending of the catalyst. With H-USY-0 and H-USY-1, propane is the second main reaction product, followed by ethane. The selectivity of these two products tends to decrease when increasing the reaction temperature. In opposite, the hydrogen selectivity tends to increase, as well as the ethylene and methane ones. For the cracking reaction over H-USY-2 and H-Y, the selectivity of ethane is higher than propane. The hydrogen selectivity seems constant with reaction temperature.

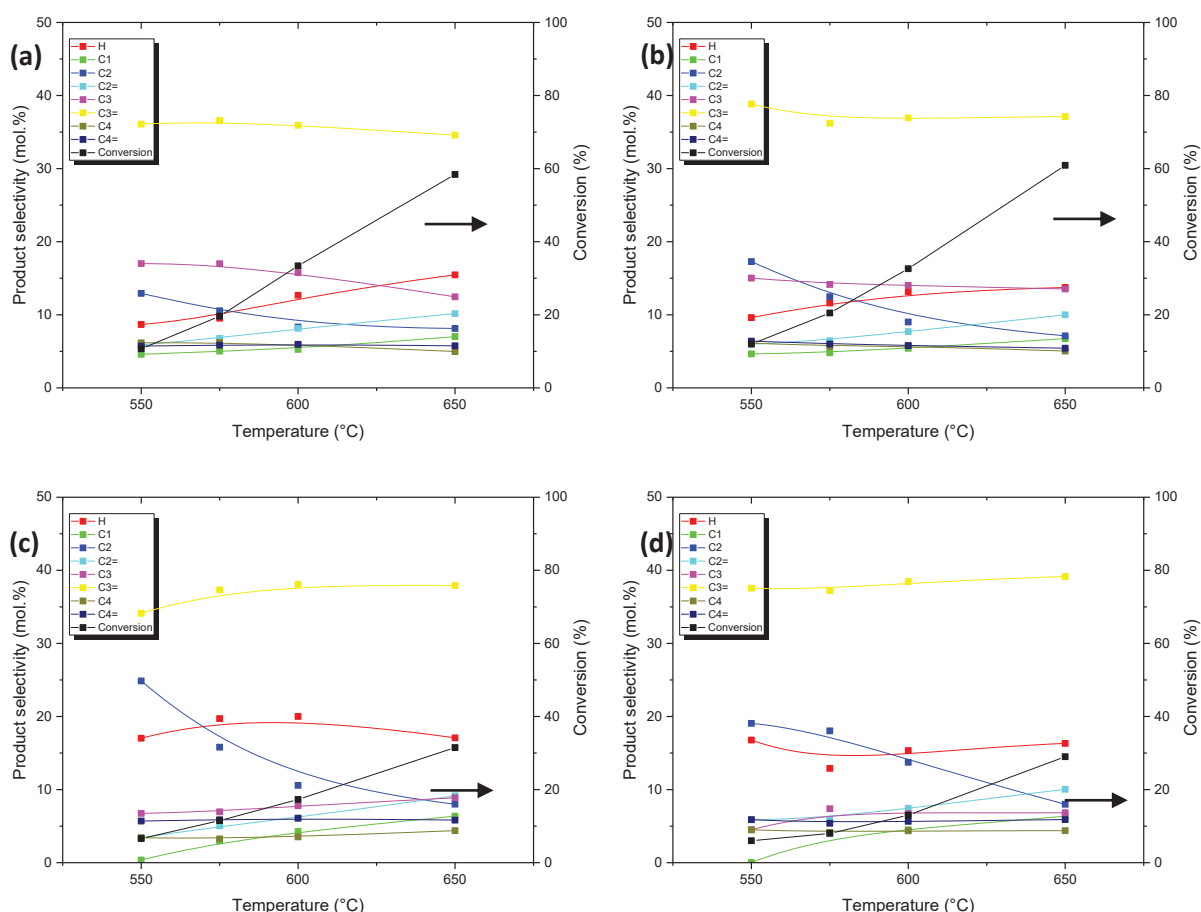


**Figure 7.** Product selectivity for the catalytic cracking of n-hexane on (a) H-USY-0, (b) H-USY-1, (c) H-USY-2 and (d) H-Y. Reaction conditions: catalyst 0.1g;  $P_{n\text{-hexane}} = 9 \text{ kPa}$ ;  $W/F_{n\text{-hexane}} = 3.9 \text{ g}_{\text{cat}} \cdot \text{h} \cdot \text{mol}_{n\text{-hexane}}^{-1}$ ; temperature 550-650°C.

The thermal cracking is investigated with experiments carried out without catalyst. Conversion of n-hexane is only detected at 650°C. At this temperature, 3.7% of the reactant is converted, into mainly C<sub>1</sub> (17.6%), C<sub>2</sub><sup>+</sup> (26.2%), C<sub>2</sub> (20.2%) and C<sub>3</sub><sup>+</sup> (16.5%).

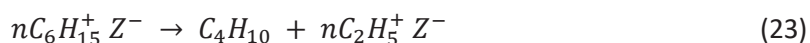
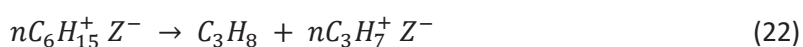
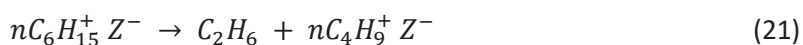
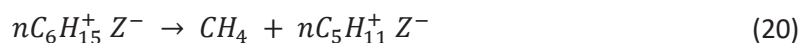
### 2.4.2 Reaction mechanism for the cracking of n-hexane

To interpret these observations, one can look at the reaction pathways already developed and suggested in the literature [5]–[8]. These mechanisms agree on the fact that carbocations – carbenium ions C<sub>n</sub>H<sub>2n+1</sub><sup>+</sup> and carbonium ions C<sub>n</sub>H<sub>2n+3</sub><sup>+</sup> – are reaction intermediates.

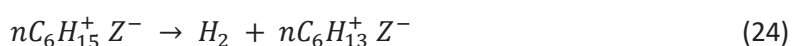
Brønsted acid sites of the catalyst, which are considered as responsible for the activity in n-hexane cracking [3], [5], can protonate the n-hexane to form a C<sub>6</sub>H<sub>15</sub><sup>+</sup> carbonium ion:



Then, a cracking of a C-C bond to form a C<sub>1</sub> to C<sub>4</sub> alkane and a C<sub>2</sub>H<sub>5</sub><sup>+</sup> to C<sub>5</sub>H<sub>11</sub><sup>+</sup> carbenium ion via the protolytic cracking route is possible:



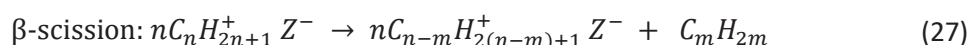
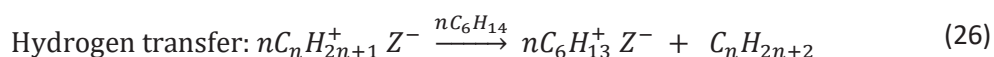
The formation of the hydrogen, widely observed within the reaction products, is also possible via a dehydrogenation of the C<sub>6</sub>H<sub>15</sub><sup>+</sup> carbonium ion. Thus, hydrogen and C<sub>6</sub>H<sub>13</sub><sup>+</sup> carbenium ion are formed:



A feasible next step is the deprotonation of the various carbenium ions to form olefin and reprotonate the zeolite:



However, as Wielers et al. [6] explained, the non-equimolar formation of C<sub>2</sub> and C<sub>4</sub> according to the experimental measurements involves the presence of secondary reactions with the carbenium ions firstly formed. These ions can react via hydrogen transfer, β-scission or isomerization, leading to a large range of reaction products:





A depiction of the various pathways is shown in Figure 8.

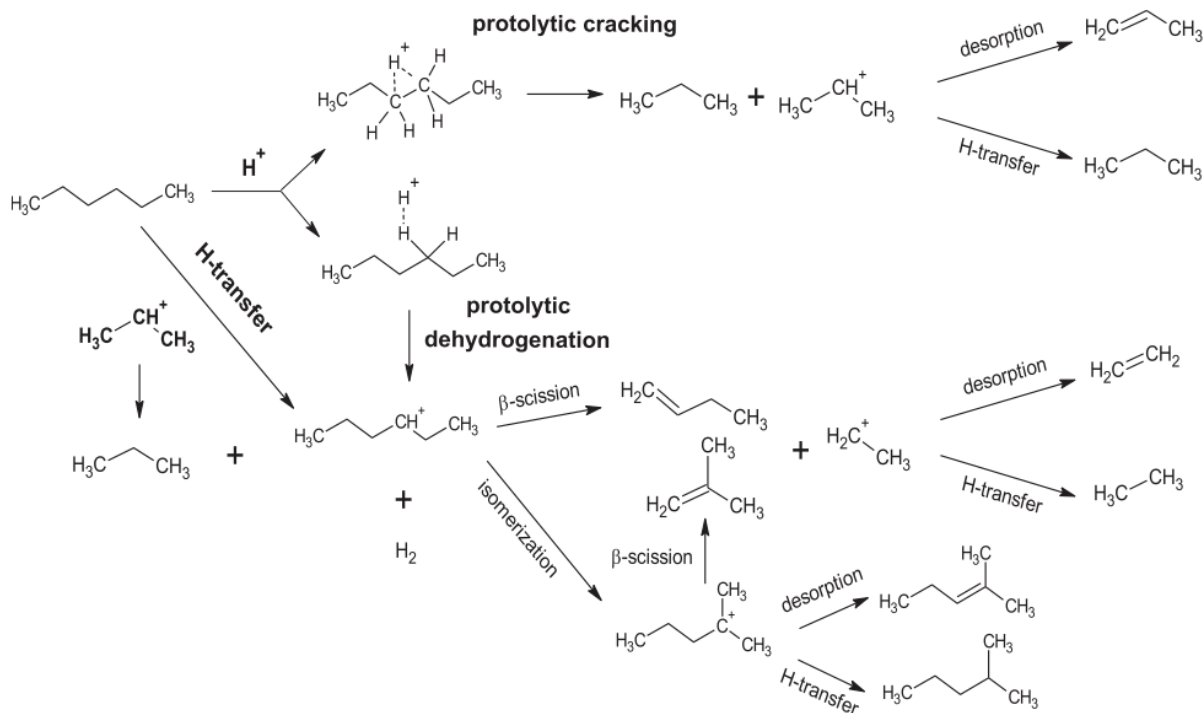


**Figure 8.** Reaction pathways of n-C6 over zeolite. Reproduced from [9].

### 2.4.3 Selectivity as a function of the conversion

To compare the results obtained with each catalyst, the Figure 9 displays the selectivity obtained for each reaction products as a function of the conversion. The main observation from these graphs is the difference regarding  $H_2$ ,  $C_3$  and  $C_4$  selectivity between, on one side, H-USY-0 and H-USY-1, and on the other side, H-USY-2 and H-Y. The latter exhibit higher  $H_2$  and lower  $C_3$  and  $C_4$  selectivity than the two other materials.

In order to compare the contribution of the different pathways previously elucidated the ratio of olefin to paraffin (O/P) is commonly used [9], [10]. When the protolytic dehydrogenation path is followed by  $\beta$ -scission or desorption, it yields olefin products, while the protolytic cracking and H-transfer produce paraffins. These considerations led To et al. [9] to introduce the following comparison between the O/P ratio and the relative contribution of each different pathway:

$$\frac{\text{Protolytic dehydrogenation} + \beta\text{-scission}}{\text{Protolytic cracking} + \text{hydride transfer}} \sim \frac{\text{Olefins}}{\text{Paraffins}} \quad (29)$$

According to this, since the olefin-to-paraffin (O/P) ratio for H-USY-2 and H-Y is higher than the one for H-USY-0 and H-USY-1, the protolytic dehydrogenation and  $\beta$ -scission seem to be boosted for these two materials. The tendency of H-USY-2 and H-Y to produce  $H_2$  is along these lines. This trend can come from pore diameter consideration. Corma et al. [10] studied this point by analysing the olefinicity of the products obtained from the catalytic cracking of n-heptane over a large variety of zeolite topologies. One of the main points was the increase of the olefin proportion when decreasing the pore diameter. The explanation came from spatial consideration: the bimolecular H-transfer involved larger transition state than the unimolecular protolytic cracking. However, H-USY-2 and H-Y are completely different on this point. H-Y porosity is made of micropores, whereas H-USY-2 is the hierarchical sample where the highest volume of mesopores can be found.

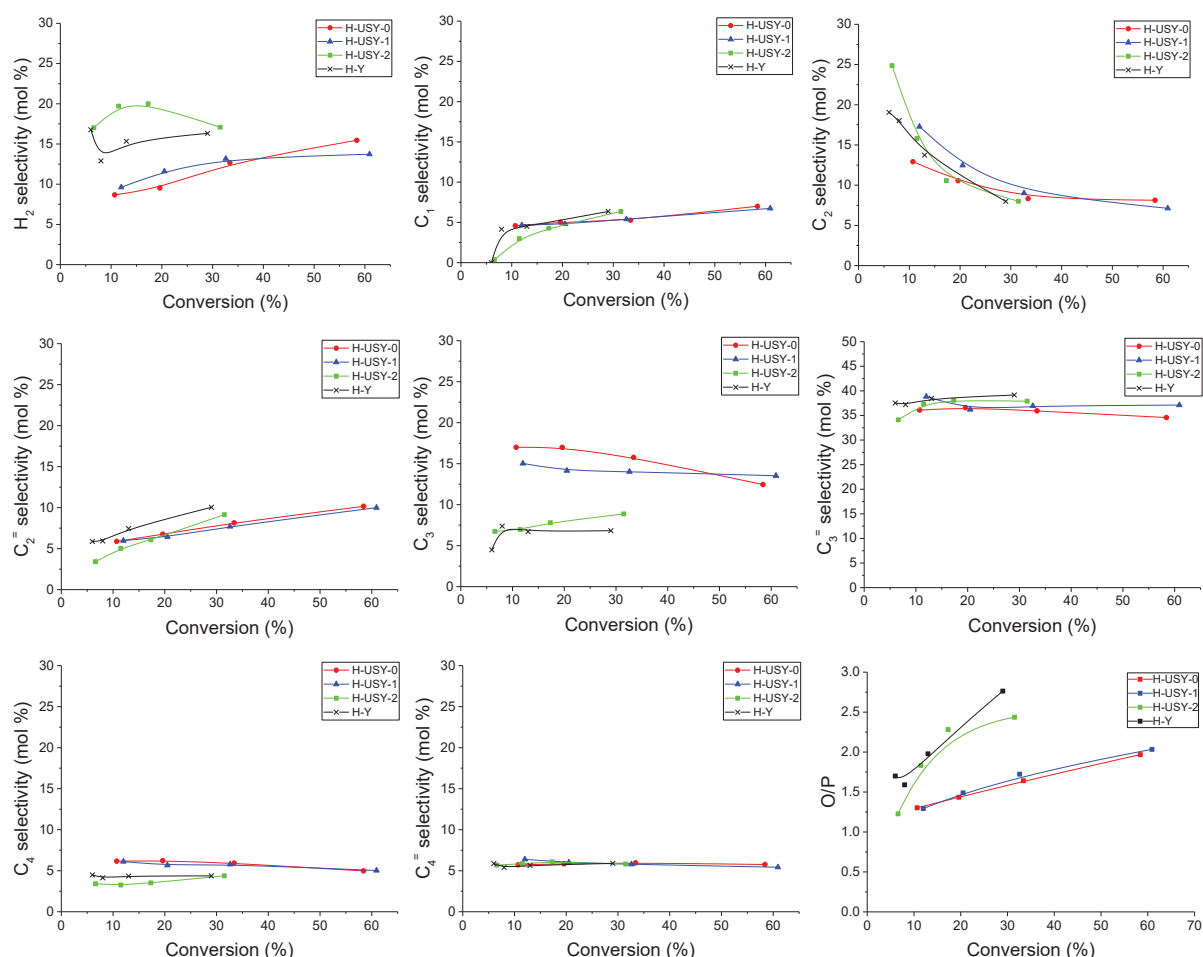


**Figure 20.** Selectivity of  $H_2$ ,  $C_1$ ,  $C_2$ ,  $C_2^-$ ,  $C_3$ ,  $C_3^-$ ,  $C_4$ ,  $C_4^-$  and O/P ratio for  $C_2+C_3+C_4+C_5$  products as a function of the conversion for the catalytic cracking of n-hexane on H-USY-0, H-USY-1, H-USY-2 and H-Y.

A common point of H-USY-2 and H-Y can be the amount of EFAL. They are the two samples exhibiting the highest amount of EFAL according to  $^{27}\text{Al}$ -MAS-NMR (see Chapter III, part 2.5). These EFAL are in pair with the high LAS concentration, which has been suggested to enhance the dehydrogenation of the paraffins [11]. This additional contribution for the dehydrogenation pathway could explain the particularly high O/P ratio for H-USY-2 and H-Y samples.

### 3. Catalytic cracking of n-hexane and butanol

To estimate the effect that might have an oxygenated molecule on the catalytic cracking of hydrocarbons, 2-butanol is added to the flow of n-hexane. The flow of n-hexane is kept the same, i.e.  $0.43 \text{ mmol}\cdot\text{min}^{-1}$ , whereas  $0.05 \text{ mmol}\cdot\text{min}^{-1}$  of 2-butanol is added to it via an additional inlet line. The mixture is diluted within a  $100 \text{ mL}\cdot\text{min}^{-1}$  flow of  $\text{N}_2$ .

#### 3.1 Preliminary check: the deactivation of the catalyst

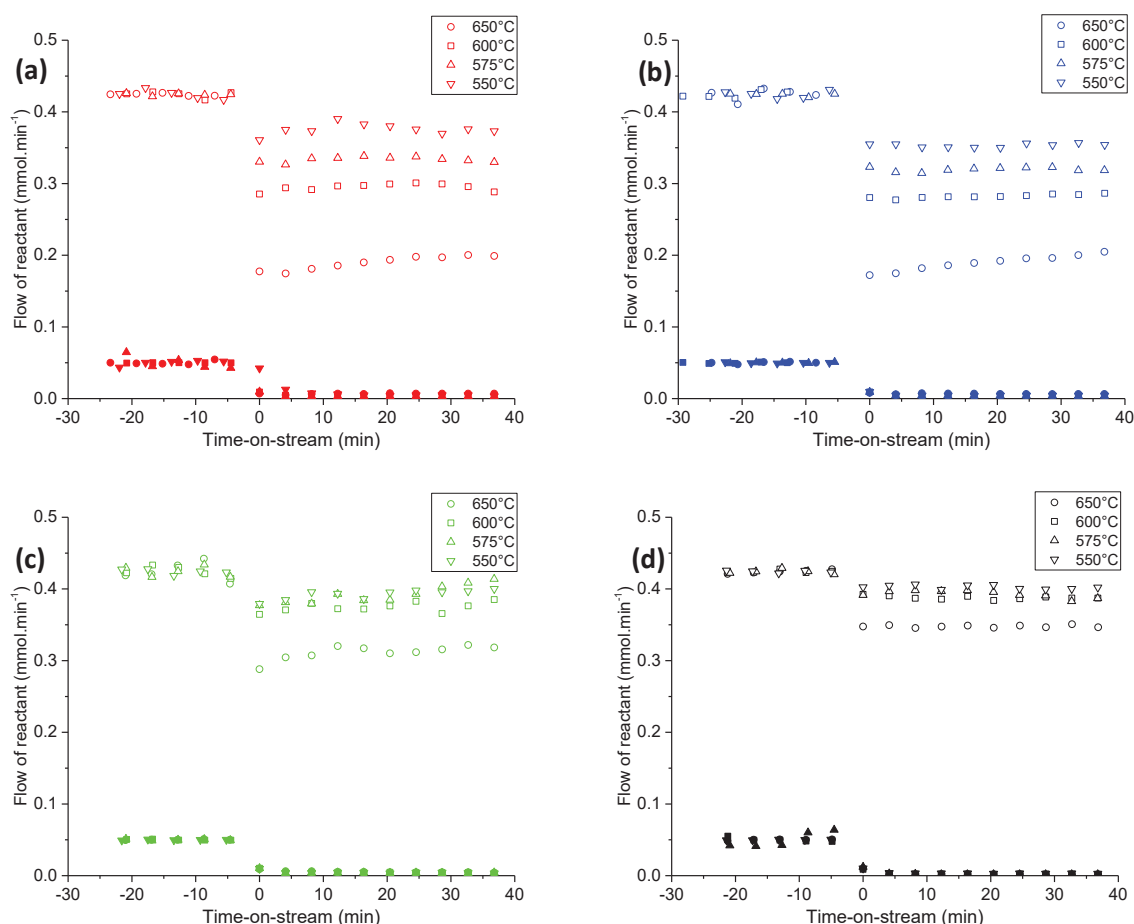


**Figure 10.** Flow of n-hexane (open symbols) and butan-2-ol (closed symbols) for their co-processing over (a) H-USY-0, (b) H-USY-1, (c) H-USY-2 and (d) H-Y.



Similarly to the pure n-hexane cracking, a small deactivation of the catalyst appears for the co-processing of n-hexane and 2-butanol. This is shown by the non-constant flow of n-hexane over the time on stream for the cracking reactions carried out at 650°C (Figure 10). This is similar to the observation made from the experiments carried out without 2-butanol (Figure 4). Regarding the flow of 2-butanol, it stays almost null and constant after the second analysis at TOS = 4 min.

### 3.2 Conversion

For this co-processing of n-hexane and 2-butanol, the initial reactant flows are 0.43 mmol.min<sup>-1</sup> and 0.05 mmol.min<sup>-1</sup>, respectively. The n-hexane conversion is calculated according to equation (16). In Figure 11, the n-hexane conversion for the catalytic cracking of pure n-hexane and n-hexane/2-butanol mixture is displayed. The deactivation of the catalysts H-USY-0, H-USY-1 and H-USY-2 at 650°C is clearly observable. However, the deactivation of H-USY-0 seems less pronounced for the co-processing of the two reactants.

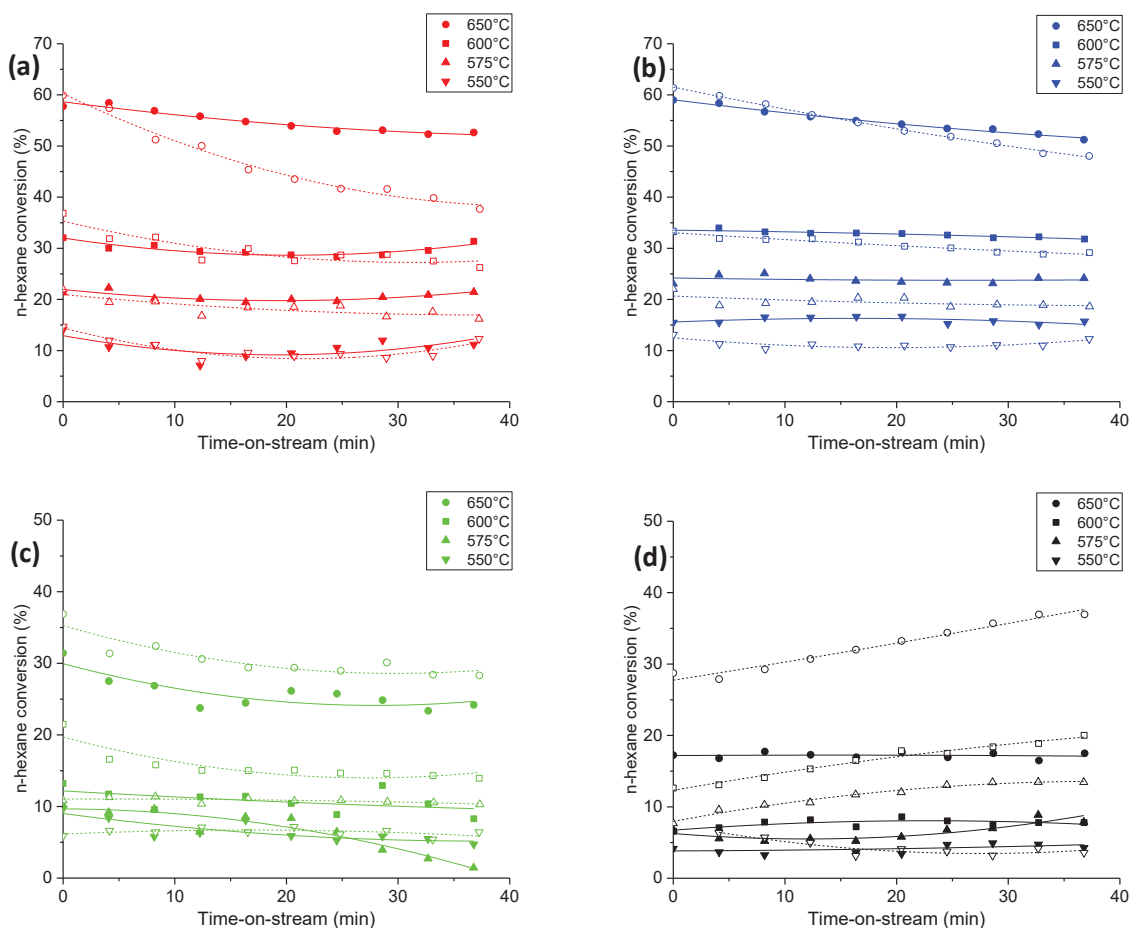


**Figure 11.** n-Hexane conversion as a function of the time-on-stream for the catalytic cracking of pure n-hexane (open symbols) and n-hexane/butan-2-ol mixture (closed symbols) over (a) H-USY-0, (b) H-USY-1, (c) H-USY-2 and (d) H-Y at 550, 575, 600 and 650°C. Reaction conditions: catalyst 0.1g;  $P_{n\text{-hexane}} = 9$  kPa;  $P_{\text{butan-2-ol}} = 1$  kPa;  $W/F_{n\text{-hexane}} = 3.9$  g<sub>cat</sub>.h.mol<sub>n-hexane</sub><sup>-1</sup>;  $W/F_{\text{butan-2-ol}} = 33.3$  g<sub>cat</sub>.h.mol<sub>butan-2-ol</sub><sup>-1</sup>; Temperature 550-650°C.

The table 3 reports the n-hexane conversion at initial time-on-stream. The samples H-USY-0 and H-USY-1 exhibit similar n-hexane conversions between the two cases. However, H-USY-2, and more significantly the sample H-Y, seem to lead to lower n-hexane conversion in the case where 2-butanol is present in the inlet flow. In order to understand this behaviour for only two of the samples, we should look at the 2-butanol transformation. The thermal and catalytic cracking of 2-butanol lead to the formation of butene and water. This water could be the reason to the lower activity, by either promoting some structural changes of the samples H-USY-2 and H-Y, or contributing to competitive adsorption on acid sites. On the latter possibility, some answer can be found in the work of Dondur et al. [12]. From the comparative adsorption of water and n-hexane on HY, they explain that in the case of a possible competitive co-adsorption the n-hexane is adsorbed preferentially. Regarding the potential changes of the catalysts during the experiments, the investigation of the N<sub>2</sub> physisorption and XRD pattern of the spent catalysts may give some answers. In Figure 12-a, we can see that the spent samples adsorb a lower amount of nitrogen than the fresh samples. This behaviour is observed for the four investigated samples. Regarding the XRD patterns (Figure 12-b), all samples exhibit a loss of crystallinity and seem to be affected in the same proportion by the cracking process. The XRD patterns at small angles show similar results (Appendix IV).

**Table 3.** Comparison of the initial conversion of n-hexane over H-USY-0, H-USY-1, H-USY-2 and H-Y with and without butan-2-ol within the reactant mixture.

Temperature (°C)	N-hexane conversion (%)							
	H-USY-0		H-USY-1		H-USY-2		H-Y	
	With Butan-2-ol ?							
	Yes	No	Yes	No	Yes	No	Yes	No
550	12.9	14.4	15.6	12.5	9.0	6.1	3.8	7.6
575	22.0	21.0	24.2	20.7	9.7	11.0	6.3	8.0
600	32.0	35.3	33.6	33.1	12.2	19.7	6.7	12.3
650	58.7	60.3	59.0	61.5	30.0	35.3	17.2	27.7

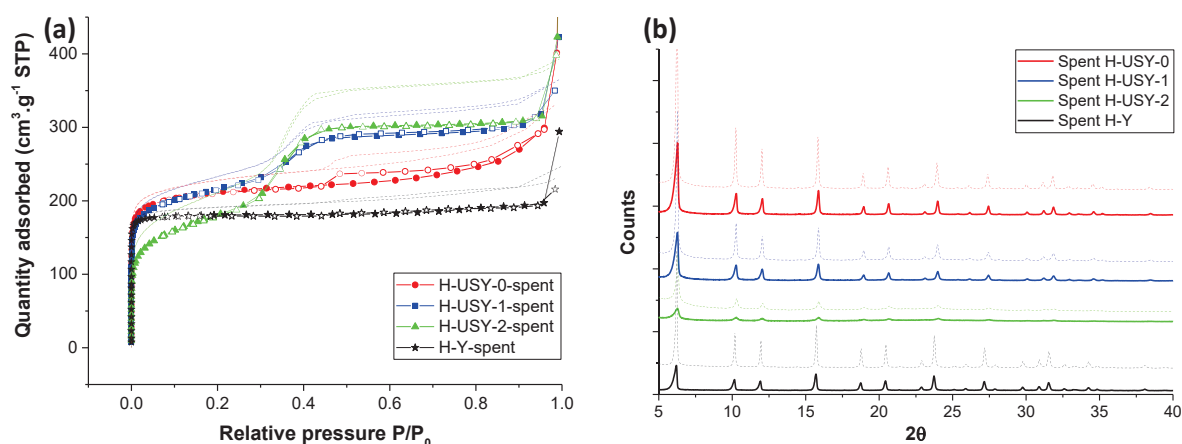


**Figure 12.** (a)  $N_2$  adsorption-desorption isotherms at 77K and (b) XRD patterns for the spent (straight lines) and fresh samples (dotted lines). Spent materials are obtained after catalytic cracking of n-hexane and 2-butanol, followed by the regeneration step under an air flow.

### 3.3 Selectivity

As for the tests carried out with pure n-hexane, the same  $C_1$  to  $C_6$  hydrocarbons are calibrated on the GC setup used for the experiments. Extra calibration has only been done for 2-butanol. In the case of experiments performed with 2-butanol, only one unidentified significant peak was observed. This compound that appeared on the PoraPLOT Q column was supposed to be  $H_2O$ , because of the concordance with the increase of the butene signal. However, this compound has not been calibrated because of its relative instability during the experiments. Similarly to the pure n-hexane cracking, the comparison of the selectivity obtained for each catalyst is made by considering the identified reaction products. The calculation is made according to the same equation (18). The addition of 2-butanol into the inlet gas mixture should increase the  $C_4^-$  selectivity since experiments carried out with pure 2-butanol mainly produce butene.

Figure 13 displays the selectivity of the main reaction products as a function of the n-hexane conversion. The H-USY-0 and H-USY-1 materials exhibit the same product selectivity. However, differences between these two materials and H-USY-2 and H-Y are observed. Higher  $H_2$ ,  $C_1$ ,  $C_2^-$  and  $C_4^-$  selectivity values are obtained for the H-USY-2 and H-Y samples than H-USY-0 and H-USY-1. As for the pure n-hexane cracking, the O/P ratios for H-USY-1 and H-Y differ from the H-USY-0 and H-USY-1 ones. The pore diameter (H-Y) and the EFAL contribution (H-Y and H-USY-2) are still two aspects that might favour the dehydrogenation pathway and so the olefinicity of the reaction products.

In the literature most of the co-processing studies involve a phenolic compound with the paraffin. Graça et al. [13], [14] studied both the effect of the phenol and guaiacol on the catalytic cracking of

n-heptane on HY zeolite. The phenol adsorption on the Brønsted and Lewis acid sites are claimed to be responsible to a further deactivation of the zeolite. Such a deactivation, or lower activity in our case, is only observed with H-USY-2 and H-Y during our study dealing with 2-butanol/n-hexane. To et al. [9] focused on the catalytic cracking of m-cresol/n-hexane mixture and the effect of the m-cresol on the reaction pathways. Considering that some synergistic acid sites were present on fresh catalyst, the co-feeding showed a faster deactivation of these sites, until only the activity of the normal BAS was remaining. The deactivation of these latter was less severe than the synergetic sites. Regarding the product selectivity, the co-feeding of m-cresol decreased the O/P ratio. A different degree of deactivation in monomolecular protolytic cracking and protolytic dehydrogenation paths was suggested. Comparing the O/P ratio obtained at each temperature, we also find a decrease when 2-butanol is co-feeding. As for To et al. case, this could come from a drop of the protolytic dehydrogenation pathway, since the hydrogen selectivity was also lower when 2-butanol was co-feeding.

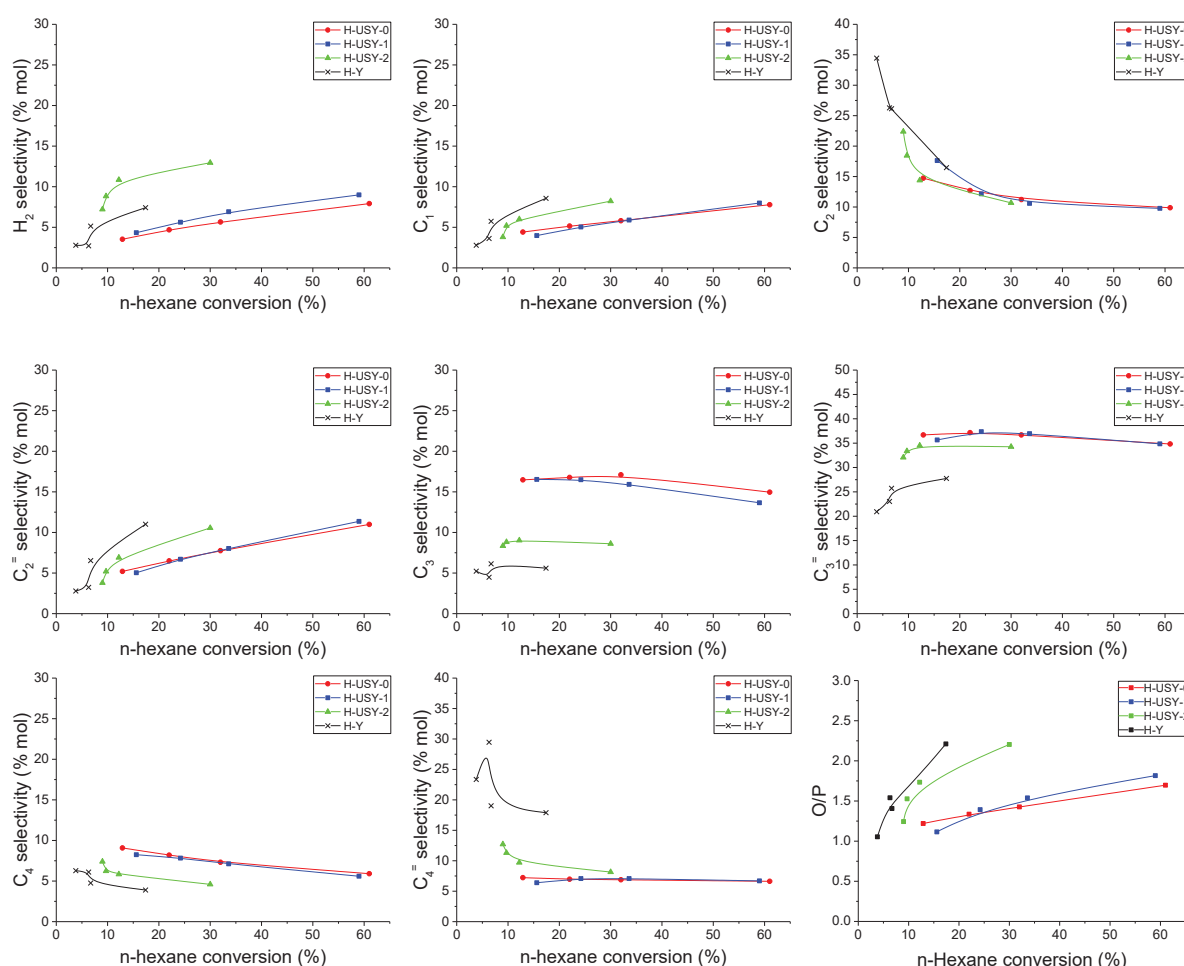


**Figure 13.** Selectivity of H<sub>2</sub>, C<sub>1</sub>, C<sub>2</sub>, C<sub>2</sub><sup>-</sup>, C<sub>3</sub>, C<sub>3</sub><sup>-</sup>, C<sub>4</sub>, C<sub>4</sub><sup>-</sup> and O/P ratio for C<sub>2</sub>+C<sub>3</sub>+C<sub>4</sub>+C<sub>5</sub> products as a function of the n-hexane conversion for the catalytic cracking of n-hexane and butan-2-ol on H-USY-0, H-USY-1, H-USY-2 and H-Y.

### 4. Conclusion

The aim of this chapter is to investigate the composition and performances of the acid sites of the four chosen materials. IR study of pyridine adsorption allowed the quantification of each acid sites. The observations made from this characterization method were confirmed with a n-hexane cracking test. The two dedicated test benches have been completely built and developed during this PhD research to serve our purpose.

Clear changes of the acid site distribution, with a loss of the number of Bronsted acid site and an increase of the number of Lewis acid site, have been observed for the hierarchical samples. The strength of these acid sites was alike for all USY samples, but slightly differed for the microporous H-Y. The cracking of n-hexane revealed a high activity for the hierarchical samples. Looking at the selectivity, two distinct groups of samples appeared: H-USY-0 and H-USY-1 on one side, and H-Y and H-USY-2 on the other. A higher proportion of olefins were obtained with the latter. Conversion on H-Y and H-USY-2 were also affected by addition of 2-butanol within the reactant, whereas it was not the case for the two others. These samples had in common a high proportion of Lewis acid sites, which was believed to affect the cracking network.

#### Highlights

- Deactivation of the catalysts during n-hexane cracking test happened at temperature above 600°C
- The turnover frequency of n-hexane cracking followed the relation:  $H-Y < H-USY-0 < H-USY-1 \sim H-USY-2$
- Higher  $H_2$  selectivity and O/P ratio were observed for reactions happening on H-Y and H-USY-2 samples
- The addition of 2-butanol within the reactant flow implied:
  - The formation of water and butene
  - The decrease of the n-hexane conversion on H-Y and H-USY-2 samples

## References for Chapter IV

- [1] J. A. Lercher and A. Jentys, "Chapter 13 - Infrared and raman spectroscopy for characterizing zeolites," in *Introduction to Zeolite Science and Practice*, vol. 168, 2007, pp. 435–476.
- [2] S. Bordiga, C. Lamberti, F. Bonino, A. Travert, and F. Thibault-Starzyk, "Probing zeolites by vibrational spectroscopies," *Chem. Soc. Rev.*, vol. 44, no. 20, pp. 7262–7341, 2015, doi: 10.1039/c5cs00396b.
- [3] S. Jolly, J. Saussey, and J. C. Lavalley, "FT-IR study of hydrocarbon conversion on dealuminated HY zeolites in working conditions," *J. Mol. Catal.*, vol. 86, no. 1–3, pp. 401–421, 1994, doi: 10.1016/0304-5102(93)E0156-B.
- [4] P. V. Shertukde, G. Marcelin, G. A. Sill, and W. Keith Hall, "Study of the mechanism of the cracking of small alkane molecules on HY Zeolites," *J. Catal.*, vol. 136, no. 2, pp. 446–462, 1992, doi: 10.1016/0021-9517(92)90075-S.
- [5] R. R. Pinto, P. Borges, M. A. N. D. A. Lemos, F. Lemos, and F. R. Ribeiro, "Kinetic modelling of the catalytic cracking of n-hexane and n-heptane over a zeolite catalyst," *Appl. Catal. A Gen.*, vol. 272, no. 1–2, pp. 23–28, 2004, doi: 10.1016/j.apcata.2004.02.004.
- [6] A. F. H. Wielers, M. Vaarkamp, and M. F. M. Post, "Relation between properties and performance of zeolites in paraffin cracking," *J. Catal.*, vol. 127, no. 1, pp. 51–66, 1991, doi: 10.1016/0021-9517(91)90208-L.
- [7] Y. V. Kissin, "Chemical mechanism of hydrocarbon cracking over solid acidic catalysts," *J. Catal.*, vol. 163, no. 1, pp. 50–62, 1996, doi: 10.1006/jcat.1996.0304.
- [8] S. Jolly, J. Saussey, M. M. Bettahar, J. C. Lavalley, and E. Benazzi, "Reaction mechanisms and kinetics in the n-hexane cracking over zeolites," *Appl. Catal. A Gen.*, vol. 156, no. 1, pp. 71–96, 1997, doi: 10.1016/S0926-860X(96)00407-3.
- [9] A. T. To and D. E. Resasco, "Hydride transfer between a phenolic surface pool and reactant paraffins in the catalytic cracking of m-cresol/hexanes mixtures over an HY zeolite," *J. Catal.*, vol. 329, pp. 57–68, 2015, doi: 10.1016/j.jcat.2015.04.025.
- [10] A. Corma, V. González-Alfaro, and A. V. Orchillés, "The role of pore topology on the behaviour of FCC zeolite additives," *Appl. Catal. A Gen.*, vol. 187, no. 2, pp. 245–254, 1999, doi: 10.1016/S0926-860X(99)00226-4.
- [11] T. F. Narbeshuber, A. Brait, K. Seshan, and J. A. Lercher, "Dehydrogenation of light alkanes

- over zeolites,” *J. Catal.*, vol. 172, no. 1, pp. 127–136, 1997, doi: 10.1006/jcat.1997.1860.
- [12] V. Dondur, V. Rakić, L. Damjanović, and A. Auroux, “Comparative study of the active sites in zeolites by different probe molecules,” *J. Serbian Chem. Soc.*, vol. 70, no. 3, pp. 457–474, 2005, doi: 10.2298/JSC0503457D.
- [13] I. Graça *et al.*, “Effect of phenol adsorption on HY zeolite for n-heptane cracking: Comparison with methylcyclohexane,” *Appl. Catal. A Gen.*, vol. 385, no. 1–2, pp. 178–189, 2010, doi: 10.1016/j.apcata.2010.07.011.
- [14] I. Graça, J. M. Lopes, M. F. Ribeiro, F. Ramôa Ribeiro, H. S. Cerqueira, and M. B. B. de Almeida, “Catalytic cracking in the presence of guaiacol,” *Appl. Catal. B Environ.*, vol. 101, no. 3–4, pp. 613–621, 2011, doi: 10.1016/j.apcatb.2010.11.002.

# Chapter V: Co-processing of VGO and PDO over hierarchical Y zeolites in MAT unit

---

## 1. Introduction

The co-processing of bio-oils with vacuum gas oil (VGO) by a fluid catalytic cracking (FCC) unit is a promising alternative to face the increasing demand for biofuels. Petrobras has already co-processed some bio-oil with VGO in a demonstration-scale unit, which prove the feasibility of this route for introducing renewable carbon in fuel [1]. Even if they did not observe any deteriorated product yields, with up to 20% of bio-oil as a feedstock, it has previously been observed that large lignin oligomers that are usually present within the bio-oils increase the coke formation and lower other product formation rates [2].

At the same time, the hierarchization of the zeolite has known a great interest [3]–[5]. A comparison between mesoporous and conventional ZSM-5 zeolites for the cracking of VGO has for the first time been published by Park et al. in 2009 [6]. Enhanced reactivity accompanied by a higher yield for valuable gasoline and a lower yield for undesired coke formation were reported. Mesopore-modified mordenite materials also proved their enhanced accessibility toward large biomass-derived molecules in the case of catalytic pyrolysis, resulting in a decrease of the oxygen content in the organic fraction [7].

Garcia-Martinez et al. [8] have investigated the activity of hierarchical Y zeolites for the catalytic cracking of VGO in an automated fluidized bed. They showed the capacity of mesoporous USY increase the bottom conversion and improve product selectivity as compared to conventional commercial USY based catalyst. To study the effect of bio-oil feedstock in similar conditions, a series of Y zeolites, presented in previous chapters, has been tested in a micro activity test (MAT) unit available at IRCELYON. The results obtained with hierarchical materials are compared to the parent USY, as well as a microporous H-Y zeolite. The processing of both pure VGO and a blending of VGO/bio-oil aim to improve the understanding of the chemistry behind these cracking reactions, such as the effect of the accessibility of the acid sites or the influence of their types and strength.



**Reminder:**

Catalysts	Si/Al XRD (ICP)	$S_{\text{BET}}$ [m <sup>2</sup> .g <sup>-1</sup> ]	$V_{\text{micro}}$ [cm <sup>3</sup> .g <sup>-1</sup> ]	$V_{\text{total}}$ [cm <sup>3</sup> .g <sup>-1</sup> ]	BAS [mmol.g <sup>-1</sup> ]	LAS [mmol.g <sup>-1</sup> ]
H-USY-0	13.6 (14.8)	869	0.30	0.45	0.28	0.10
H-USY-1	18.6 (14.4)	827	0.28	0.50	0.23	0.16
H-USY-2	29.0 (14.1)	709	0.23	0.55	0.13	0.18

## 2. Feedstock characterisation

### 2.1 Vacuum Gas Oil

The VGO feedstock has been provided by REPSOL as part of a European project. The elemental composition and properties of this feedstock is displayed in Table 1. The main characteristics are its low sulphur and nitrogen content. The distillation of the feedstock according to ASTM-D-1160 reveals an initial boiling point of 287°C for the lightest compound of the mixture. At 545°C, 81.5% of the initial volume has been recovered.

**Table 1.** Properties of VGO feedstock used in this study

Properties		Elemental composition [wt.%]	
Density [kg.m <sup>-3</sup> ]	0.925	C	87.8
ASTM-D-1160	[°C]	H	11.9
IBP	287	N	<0.1
5% vol	403	O	0.2
50% vol	479	S	<0.1
80% vol	524	H/C [mol. ratio]	1.6
FBP	545	O/C [mol. ratio]	<0.01
Recovery [% vol]	81.5		

To complete the SIM-DIS, which determines the recovered volume of the liquid products versus the boiling point, GCxGC-FID analysis of the VGO has been carried out (Figure 1). This complimentary analysis provides information on the chemical composition of the fractions. For this analysis, 0.214g

of VGO has been solubilized into 0.219g of THF solution containing 1.1 wt.% of hexadecane. The main observable compounds are paraffins having between 20 and 32 carbon atoms. Another group of products, corresponding to tri- (phenanthrene, anthracene) and tetra-cyclic aromatics (tetracene, pyrene) is accounting for 20% of the observable products. However, since 4-ring polycyclic aromatics hydrocarbons have often a boiling point in the range 300-450°C [9], it is very likely that bulkier compounds than the ones observed on GCxGC plot are present in the VGO mixture.

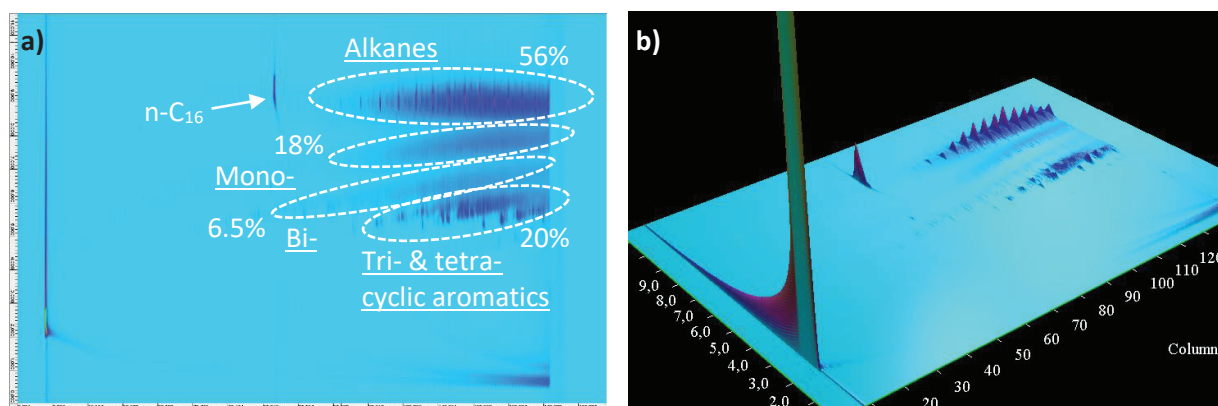


**Figure 1.** (a) GCxGC-FID plot and (b) 3D view of VGO in THF, with hexadecane as internal standard.

### 2.2 Partially deoxygenated oil (PDO)

The hydrodeoxygenation step, which is often suggested for the upgrading of bio-oils prior to feeding them into FCC unit, requires a large amount of hydrogen at elevated pressure. This is holding back the development of bio-oil processing in FCC unit due to the extra cost. Gueudré et al. [10] have investigated the co-processing of partially deoxygenated oil with VGO. They looked for an optimum combining: a low hydrogen consumption for bio-oil upgrading, a sufficient degree of deoxygenation of the pyrolysis oil to be co-processed and good product yields. From their study, they found that co-refining of mildly hydrotreated bio-oil lead to an optimum naphtha quality, coupled with similar coke formation as pure VGO cracking, when the hydrogen consumption for the pyrolysis oil upgrading was between 150 and 202 NL.kg<sup>-1</sup><sub>PL</sub>.

Hence, the choice has been taken to perform the following co-processing experiments with similar partially deoxygenated bio-oil. This PDO has been provided by BTG as part of the European project. Its elemental composition is displayed in Table 2. Comparing to the usual FCC feedstock that is the VGO, we note the high oxygen content. The amount of water is low for a bio-oil (0.4 wt. %) because of the vacuum distillation step performed by the partner during the upgrading.

The GCxGC-FID analyses of a sample containing 0.073g of PDO into 0.067g of THF containing 1.1 wt.% of hexadecane, mainly reveals the presence of paraffins, alcohols, aromatics and methoxyphenols (Figure 2).

**Table 2.** Elemental analysis of the PDO feedstock used this study.

Elemental composition [wt. %]	
C	63.1
H	8.5
N	0.13
O	28.2
S	<0.1
H/C [mol. Ratio]	1.6
O/C [mol. Ratio]	0.3
Water content <sup>a</sup> [wt. %]	0.4

<sup>a</sup> From Karl-Fisher titration.

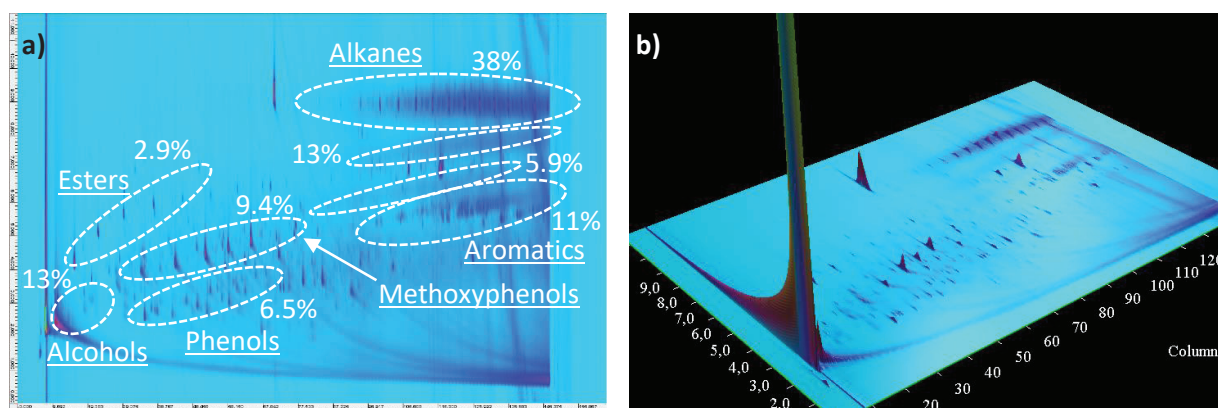


**Figure 2.** (a) GCxGC-FID plot and (b) 3D view of PDO in THF, with hexadecane as internal standard

### 3. Catalytic cracking in MAT unit

#### 3.1 Generalities

The evaluation of the catalyst performances is done by carrying out experiences at different catalyst-to-oil (Cat/Oil) ratio. For each catalyst, 1 g of dry sample powder, previously sieved between 150 and

300  $\mu\text{m}$ , is loaded into the MAT reactor. The range of the investigated Cat/Oil ratio is 0.3 to 1.7. During the experiment, the heaviest products are condensed into a cool bath, whereas the remaining products in the gas phase are stored in a burette. A complete scheme and description of the unit is available in Chapter 2, Part 2. The GC analysis of the volatile fraction gives us the proportion of hydrogen, carbon monoxide and dioxide, dry gas (including methane, ethane and ethylene), liquefied petroleum gas (LPG – including all  $\text{C}_3$  and  $\text{C}_4$ ) within the collected gases. The condensable products are analysed via simulated distillation, allowing to determine the proportion of naphtha (referring to  $\text{C}_5$  products and compounds having a boiling point up to  $221^\circ\text{C}$ ), light cycle oil (LCO –  $221\text{--}360^\circ\text{C}$ ) and decanted oil (DO – over  $360^\circ\text{C}$ ). The yield of each group of products is calculated as follows:

$$Y_i = \frac{m_i}{m_{\text{feed}}} \times 100 \quad (30)$$

Where:

$Y_i$  is the yield of the group of products  $i$  (%)

$m_i$  is the mass of the group of products  $i$  (g)

$m_{\text{feed}}$  is the mass of feedstock injected into the reactor (g)

Since the feedstocks are composed of molecules belonging to LCO and DO groups, the conversion is calculated as following:

$$\text{Conversion (\%)} = 100 - Y_{\text{LCO}} - Y_{\text{DO}} \quad (31)$$

## 3.2 Catalytic cracking of pure VGO

### 3.2.1 Conversion

As a first step, the catalytic performances of the materials are investigated via the catalytic cracking of pure VGO. In Figure 3a, the conversion obtained at  $560^\circ\text{C}$  for H-USY-0, H-USY-1, H-USY-2 and H-Y is displayed as a function of the Cat/Oil. As expected, when the Cat/Oil ratio increases, higher conversions are obtained. Up to 81.7% of conversion is reached for the H-USY-1 material at Cat/Oil = 1.7. Similarly to the catalytic results obtained from the n-hexane cracking, the higher conversions are obtained with the H-USY-0 and H-USY-1 materials. The microporous H-Y and hierarchical H-USY-2 samples exhibit similar conversions at high Cat/Oil.

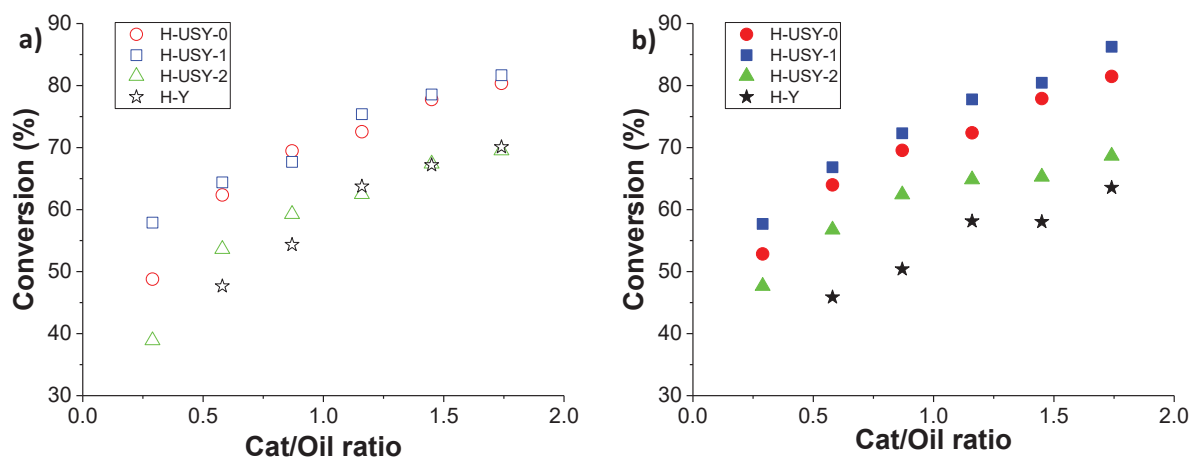


**Figure 3.** Conversion as a function of the catalyst-to-oil ratio for the catalytic cracking of (a) pure VGO and (b) 90% VGO and 10% PDO blending at 560°C.

### 3.2.2 Product yields

The various product yields and the olefin-to-paraffin ratio (O/P), calculated from the gas products having two to four carbon atoms, are displayed in Figure 4 as functions of the conversion. The yields for dry gas, LCO and DO are similar for the four catalysts tested. A three times higher hydrogen yield is obtained with H-Y than with H-USY-0, H-USY-1 and H-USY-2. This H-Y sample also leads to lower LPG and higher naphtha yields than the three other materials. Regarding the O/P ratio, the catalytic cracking over H-Y leads to the lowest olefinicity. Such behaviour can seem counter-intuitive since material producing more saturating compounds should also produce less hydrogen. However, the O/P ratio presented here takes into account the molecules having between two and four carbon atoms. Moreover, H-Y may get a higher hydrogen yield than other catalysts because of a different reaction network for the cracking of heavy compounds composing the VGO. Carbonium ions, formed due to proton transfer from zeolite BAS to the paraffins, can be converted into hydrogen plus carbenium ions. This pathway might be enhanced in the case of H-Y sample at the expense of the protolytic cracking forming a paraffin plus a carbenium ion (see Chapter 1, Part 2.7.1). Looking at the coke yield, another reason can be raised since the H-Y sample exhibits the highest coke formation. The coke often corresponds to polyaromatics formed by condensation and rearrangement steps [11]. These reactions consume light olefins to build larger compounds, which may be the reason to the lower O/P ratio of H-Y sample. The higher coke yield observed for the microporous H-Y may also be enhanced because of steric blockage within micropores.

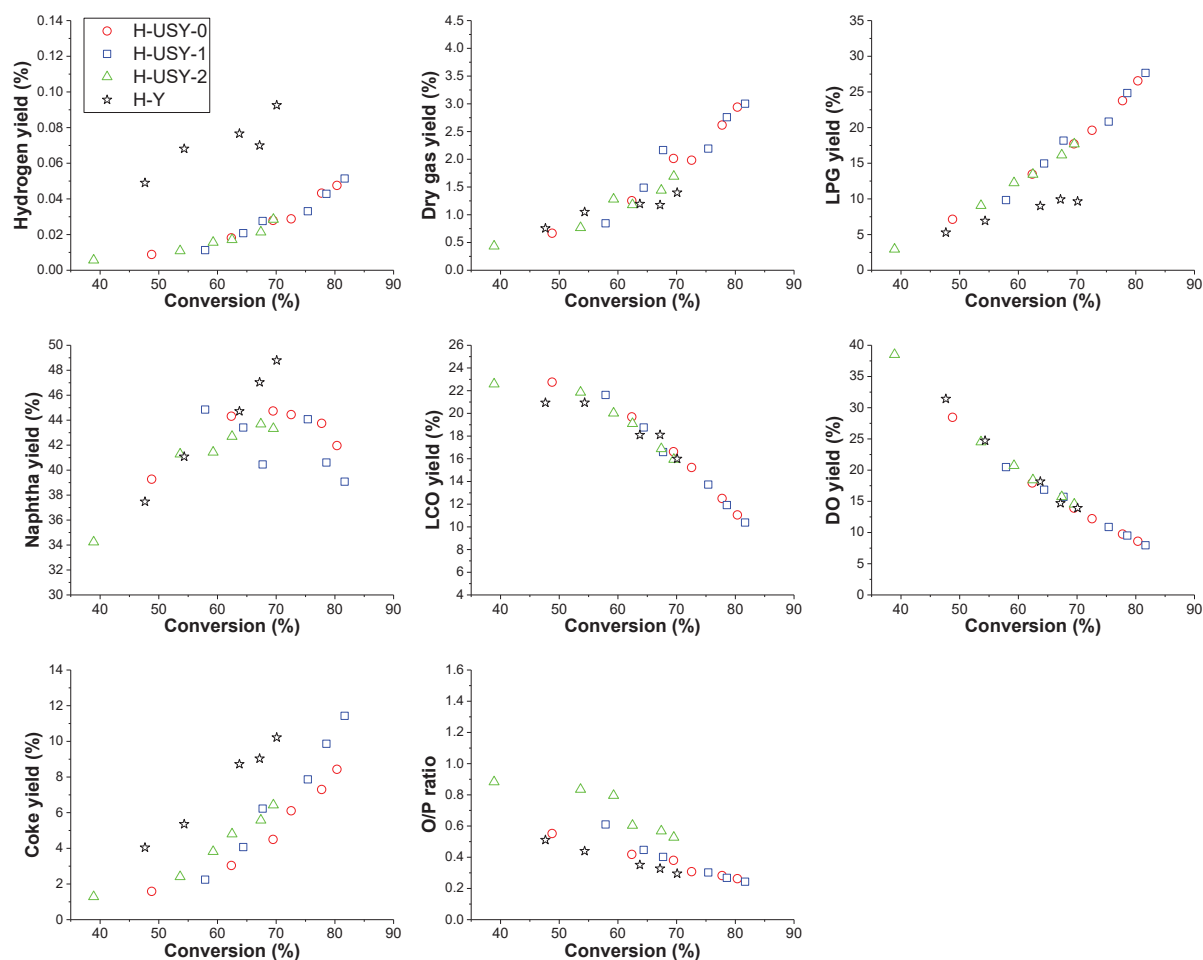


**Figure 4.** Products yield and olefin-to-paraffin (O/P) ratio as a function of the conversion for the catalytic cracking of pure VGO in MAT unit at 560°C.

Regarding the three other samples, it seems that H-USY-2 produces slightly more coke than H-USY-1, which produces more coke than H-USY-0. This is in the opposite order of the mesoporous volume. However, the post-synthetic treatments performed for hierarchization of H-USY-1 and H-USY-2 was in pair with catalytic sites modifications. H-USY-2 contains lower BAS and higher LAS than H-USY-1 and H-USY-0. Presence of LAS is known for enhancing the hydrogen transfer, which is associated to the formation of aromatics and coke [12], [13]. This can be a reason for the observed differences for coke yields between H-USY-0, H-USY-1, H-USY-2.

### 3.3 Co-processing of VGO and PDO

#### 3.3.1 Conversion

Similarly to pure VGO cracking, the effect of the bio-oil on its co-processing with the VGO is investigated. The choice has been taken to include 10 wt.% of PDO as feedstock. The conversion of

this blending, over H-USY-0, H-USY-1, H-USY-2 and H-Y at 560°C, as a function of the Cat/Oil ratio is displayed in Figure 3b. As for the cracking of pure VGO, the highest conversions are obtained for H-USY-0 and H-USY-1. The microporous H-Y sample exhibits the lowest conversion among the four materials tested. This conversion is slightly lower than the pure VGO processing, which confirms the difficulty to substitute VGO by bio-oil feedstock. However, except for the lowest cat/oil ratio, the three other materials exhibit similar conversions for the catalytic cracking of both VGO/PDO blending and pure VGO.

### 3.3.2 Product yields

Figure 5 displays the various product yields and O/P ratio obtained when 10% of PDO is included in the feedstock. The hydrogen yield obtained with H-Y is still higher than the ones with H-USY-0, H-USY-1 and H-USY-2. However, this amount is lower than the case of pure VGO processing, which may signify that some hydrogen atoms are reacting with the oxygen coming from the bio-oil. Regarding the O/P ratio, as previously observed, H-Y sample produces fewer olefins and/or more paraffins than the other materials. The same reasons as pure VGO processing may be suggested as the coke yield for H-Y sample is still higher than for other materials.

Among the three other samples, a clear difference appears for coke yield. The H-USY-2 sample leads to a higher coke yield than H-USY-1, which leads a higher one than H-USY-0. The above-mentioned effect of LAS concentration on aromatic and coke enhancement via hydrogen transfer is still present in this case. Moreover, as suggested by Fogassy et al. [14], the more polar oxygenated molecules can adsorb more strongly on the active acid sites than the hydrocarbons, which also lead to coke formation.

The O/P ratios of H-USY-0, H-USY-1 and H-USY-2 show that at low conversion – below 60% – H-USY-2 produces a higher amount of olefins than H-USY-1, which produces more olefins than H-USY-0. A decrease of these ratios is observed when the conversion increases. The drop of O/P ratio is the most significantly observed for H-USY-2, which matches with the high increase in coke formation and the possible cyclization, aromatization of light olefins.

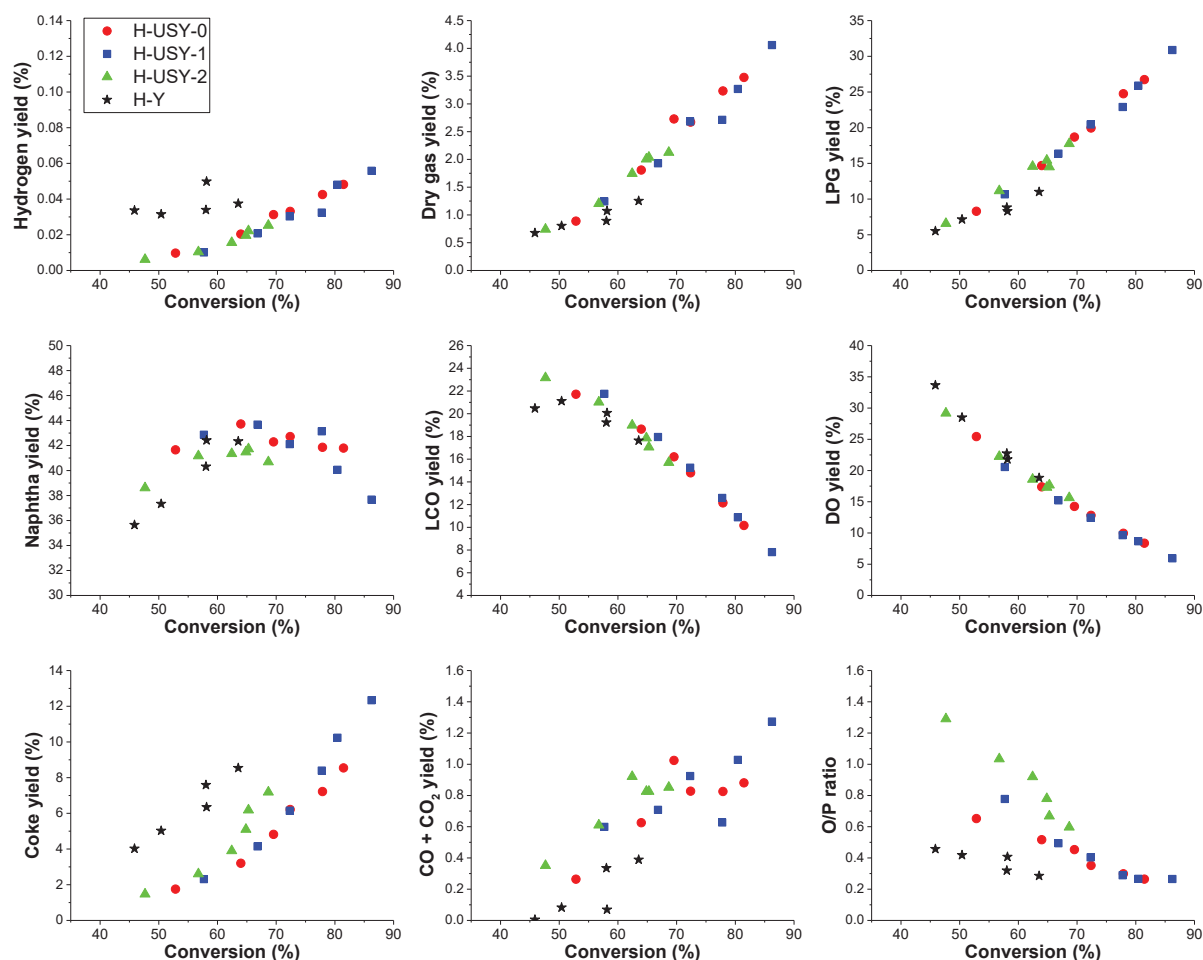


**Figure 5.** Products yields and olefin-to-paraffin (O/P) ratio as a function of the conversion for the catalytic cracking of a mixture composed of 90% VGO and 10% PDO in MAT unit at 560°C.

### 3.3.3 Comparison at constant coke production

In an industrial FCC unit, since it operates in a heat balance model, the FCC process takes place at constant coke yield. It means that the coke production must be constant to keep other parameters, like the riser temperature, the feed preheating temperature, the total feed and steam rates, constant. Hence, when a new catalyst showing a lower coke tendency is used, the Cat/Oil ratio need be increased to keep constant the coke production. It would lead to a higher conversion.

To stick at this FCC process condition, Table 3 displays the yields obtained with each catalyst when the coke yield is at 5%. When the coke yield is considered at 5%, the conversion follows the order H-Y (50.3%) < H-USY-2 (64.1%) < H-USY-1 (68.7%) < H-USY-0 (70.0%). Hence, the catalyst allowing the best conversion among the four tested samples would be H-USY-0. In this case, the main product fraction is the naphtha (42.9%), followed by the LPG (18.7%). As constant coke production, the



hierarchical H-USY-1 and H-USY-2 materials exhibit slightly lower conversion than H-USY-0. A much lower conversion is observed for the H-Y sample.

**Table 3.** Results from the co-processing of VGO and PDO interpolated at constant coke.

<div>Catalyst</div> <div>Yields [%]</div>	H-USY-0	H-USY-1	H-USY-2	H-Y
Hydrogen	0.03	0.02	0.02	0.04
CO + CO <sub>2</sub>	0.86	0.69	0.83	0.06
Dry Gas (C <sub>1</sub> -C <sub>2</sub> )	2.5	2.1	1.9	0.8
LPG (C <sub>3</sub> -C <sub>4</sub> )	18.7	17.4	14.9	6.6
Olefins/Paraffins	0.42	0.45	0.79	0.43
Naphtha (C <sub>5</sub> -221°C)	42.9	43.5	41.5	37.9
LCO (221-360°C)	16.0	17.0	18.0	20.9
DO (360°C +)	14.0	14.3	17.9	28.8
Coke	5.0	5.0	5.0	5.0
Conversion	70.0	68.7	64.1	50.3

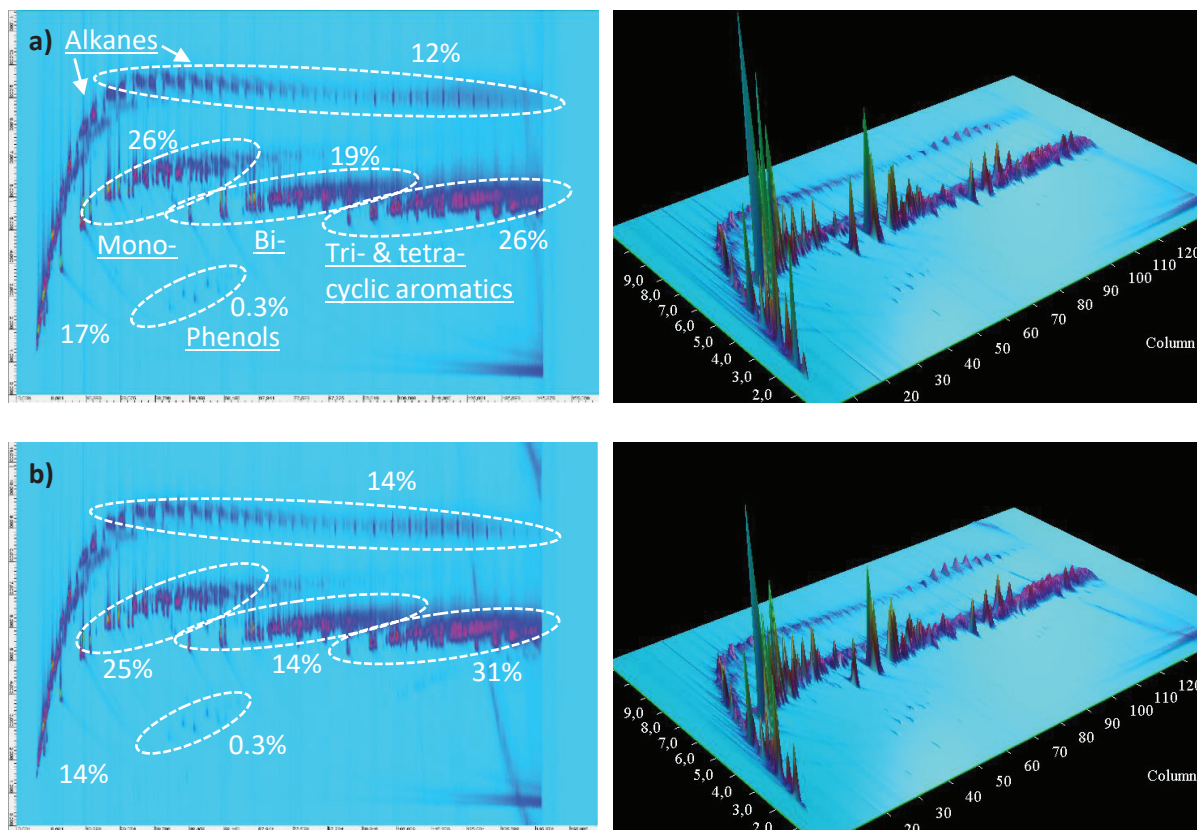
### 3.3.4 GC x GC

GCxGC analyses are carried out for four of the liquid fractions obtained after the co-processing (Figure 6). These fractions correspond to Cat/Oil ratio leading to similar conversions (52.9% to 58%). The products can be compared to the one initially present in VGO and PDO feedstock (Figure 1 and 2).

The four liquid product fractions obtained from the co-processing on H-USY-0, H-USY-1, H-USY-2 and H-Y exhibit a small fraction of phenol compounds. According to the area of the corresponding peaks, the phenols correspond to 0.3, 0.3, 0.1 and 0.1 mol.% of the observable cracking products obtained from H-USY-0, H-USY-1, H-USY-2 and H-Y respectively. None of the other oxygenated compounds that were observed for PDO sample is identified.

Regarding the initial C<sub>20</sub> to C<sub>32</sub> paraffins initially observed for the VGO and PDO feedstocks, their proportions significantly decrease for reactions on H-USY-0, H-USY-1 and H-USY-2. Instead, lighter paraffins appear. They are observable at shorter retention time on x-axis. For H-Y sample, the increase of light paraffins at the expense of the heavier ones is less notable. This agrees with the LPG yield observed for H-Y catalyst, which is lower than for the other catalysts.

Polycyclic aromatics compounds are also visible in the cracking product samples. However, they are more present on GCxGC plot of these samples than for the initial feedstocks. One reason is the cracking of molecules initially too large for being observed, into lighter ones. Another explanation could be the formation of aromatics from olefins cyclisation into naphthenes, followed by dehydrogenation [15]. The polycyclic aromatics proportion is significantly lower for H-Y than for H-USY-0, H-USY-1 and H-USY-2. These observations confirm the difficulties of H-Y to crack large compounds, comparatively to the three USY. Considering the high coke yield for H-Y, the lower aromatic proportion in reaction products from this catalyst could also be explained by higher tendency for condensation reactions of aromatics to form coke deposits.



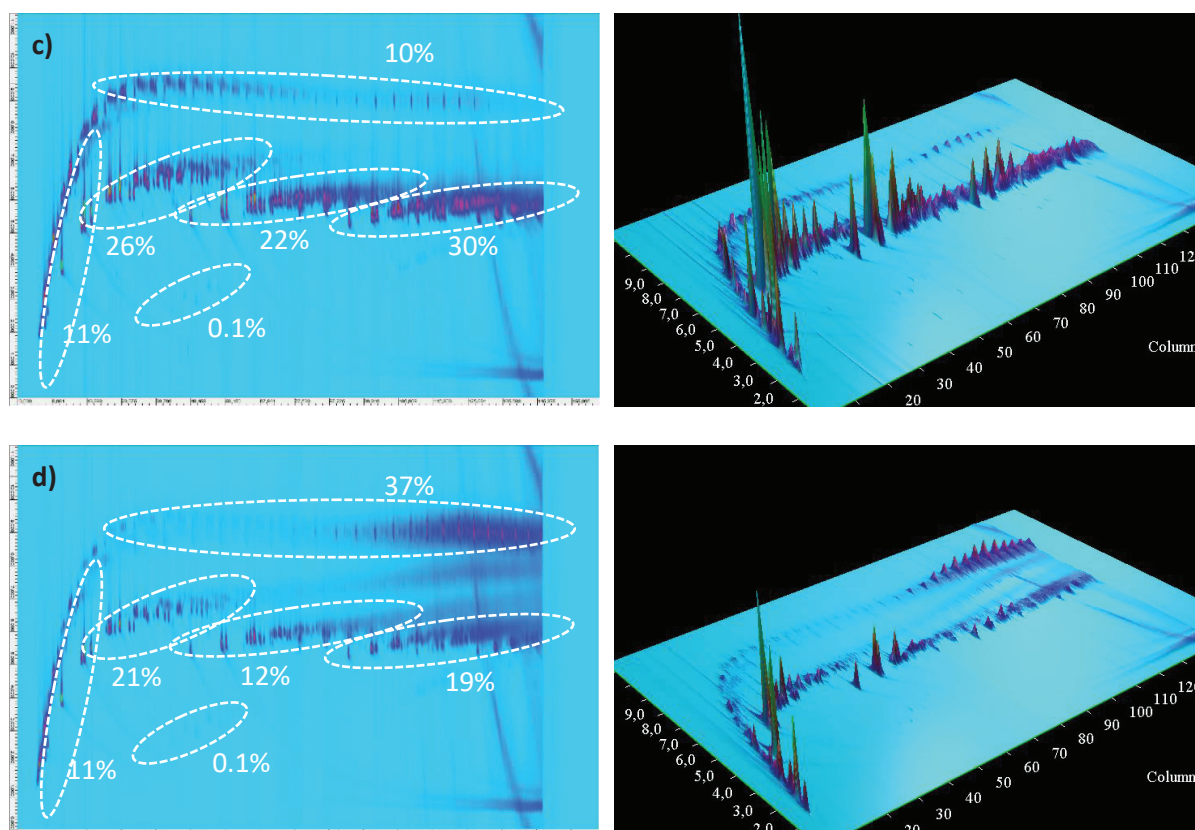


**Figure 6.** GCxGC plot (left) and 3D view (right) of the liquid products obtained from the catalytic cracking of 90% VGO and 10% PDO over (a) H-USY-0, (b) H-USY-1, (c) H-USY-2 and (d) H-Y.

### 3.3.5 $^{31}\text{P}$ NMR

A good complement to the GCxGC for analysing the residual oxygenated compounds is the  $^{31}\text{P}$  NMR. As depicted in Chapter II, Part 2.2.3, the reaction between TMDP (2-chloro-4,4,5,5-tetramethyl-1,3,2-dioxaphospholane) and hydroxyl functional groups (phenolic, aliphatic or carboxylic) leads to the formation of products observable by  $^{31}\text{P}$  NMR. Hence, the presence of hydroxyl groups within the liquid products obtained from the catalytic cracking of 90% of VGO and 10% of PDO can be investigated via this reaction. The used of an internal standard (cyclohexanol) allows a quantification of the hydroxyl functional groups that react with TMDP.

The liquid fractions analysed by  $^{31}\text{P}$  NMR are chosen from MAT experiments that have led to similar conversions: 52.9%, 57.7%, 56.7% and 58% for H-USY-0, H-USY-1, H-USY-2 and H-Y, respectively. The  $^{31}\text{P}$  NMR spectra are displayed in Figure 7. The reaction between the cyclohexanol, used as internal standard, and the TMDP leads to the formation of a phosphitylated compound detected at -145ppm. The peaks in the range 133.6-136.6ppm, 137.3-144.7ppm and 145.5-150.0ppm correspond to the carboxylic, phenolic and aliphatic hydroxyl groups, respectively. The quantifications performed for the four samples are listed in Table 4, in addition to the results obtained for the PDO feedstock

before processing. The cracking reactions are performed with 10% of PDO, which should be kept in mind when comparing these results.

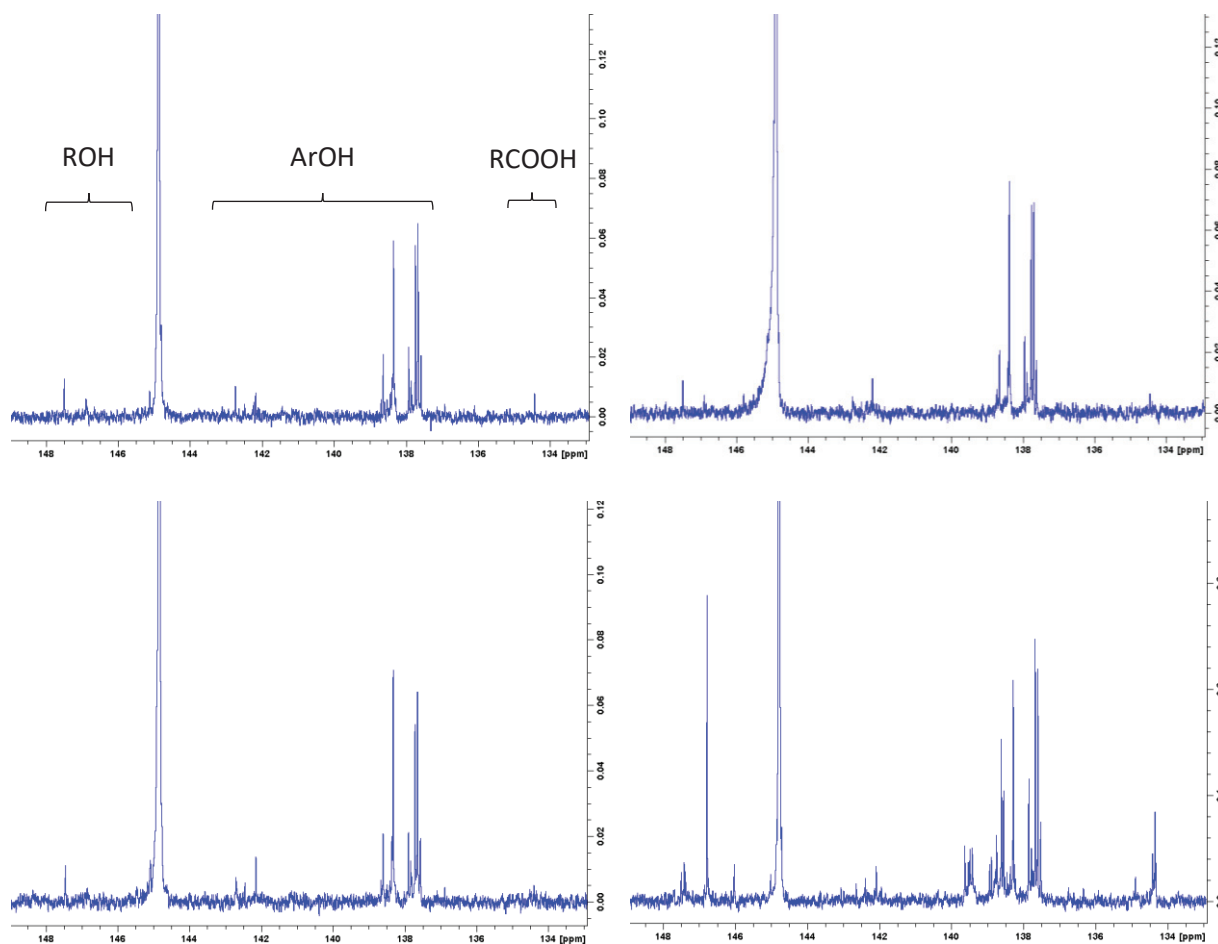


**Figure 7.**  $^{31}\text{P}$  NMR spectra after phosphitylation of the liquid product fraction obtained from the co-processing of VGO and PDO over (a) H-USY-0, (b) H-USY-1, (c) H-USY-2 and (d) H-Y with TMDP.

The liquid product fractions obtained with H-USY-0, H-USY-1 and H-USY-2, exhibit similar hydroxyl concentrations, which are mainly phenolic hydroxyl. This concentration of phenolic OH is  $0.03 \text{ mmol.g}^{-1}$  for the three samples. This agrees with GCxGC results, where only phenols are identified after catalytic cracking. The carboxylic and aliphatic OH groups observed in PDO feedstock seem to be completely converted during catalytic cracking. This leads to the formation of water, CO and  $\text{CO}_2$  observed by other technics. For H-Y sample, the residual concentration of phenolic OH is ten times higher than with other catalysts. The concentration of  $0.35 \text{ mmol.g}^{-1}$  corresponds approximately to 10% of the value found for PDO feedstock. It suggests that phenolic OH group are not converted when the reaction is performed over H-Y. This is not concordant with the low phenol proportion observed in GCxGC. Similarly, no alcohols are observed on GCxGC after catalytic reaction, whereas

some aliphatic OH are reacting with TMDP. An explanation can be the reaction between some compounds that are not visible in GCxGC, due to their heavy molecular weight, and TMDP.

**Table 4.** Concentration of carboxyl (RCOOH), aliphatic (ROH) and phenolic (ArOH) within the PDO feedstock and the liquid fractions of products obtained from the co-processing of 90% VGO and 10% PDO over H-USY-0, H-USY-1, H-USY-2 and H-Y.

	PDO	H-USY-0	H-USY-1	H-USY-2	H-Y
Conversion [%] (Cat/oil ratio)	-	52.9 (0.3)	57.7 (0.3)	56.7 (0.6)	58.0 (1.4)
Concentration [mmol.g <sup>-1</sup> ]					
RCOOH	0.49	0.00	0.00	0.00	0.03
ROH	5.77	0.00	0.00	0.00	0.08
ArOH	3.43	0.03	0.03	0.03	0.35
Total	9.20	0.03	0.06	0.03	0.46

### 3.4 Comparison of the pure VGO and VGO/PDO processing

Comparable conversions are obtained for the pure VGO and VGO/PDO processing over the USY series of materials. However, on a purely microporous material as H-Y sample, the addition of the PDO feedstock decreases the conversion (Figure 3). Regarding the product selectivity, the addition of PDO decreases the H<sub>2</sub> yield in the case of reactions over H-Y. It increases the O/P ratio for H-USY-0, H-USY-1 and H-USY-2 samples (Figures 4 and 5). Due to some disparate dot plots, sharper analysis between the two cases are difficult to make.

### 3.5 Comparison with commercial FCC catalyst

To compare the co-processing of VGO and PDO carried out with either pure zeolite or commercial FCC catalyst, it is possible to compare of our results with the one obtained by Gueudré [16] (see Chapter I, Figure 8). On the same MAT unit, Gueudré et al. [10] performed a screening of the co-processing of VGO and various bio-oil feedstock. The Cat/Oil ratios of experiments with FCC catalyst are higher than the one with pure zeolite because of the lower content of zeolite in FCC catalyst. The FCC catalyst exhibits similar coke production as the series of USY materials, starting from a coke yield of 1.5 wt.% at 30% conversion up to 6 wt.% at 75% conversion. Regarding the naphtha proportion, the commercial FCC catalyst showed lower yield than the four samples investigated in this thesis. In both cases the naphtha yield seems to reach an optimum around 65% conversion.

#### 4. Effect of the catalyst acidity and porosity on the catalytic cracking

Garcia-Martinez et al. [8] have investigated the catalytic cracking of VGO with mesoporous USY (see Chapter I, Figure 19). They have found improvements for the bottom conversion and better product selectivity – more gasoline and less coke. Looking at our results for the catalytic cracking of VGO feedstock in Figure 4, the hierarchical H-USY-1 and H-USY-2 zeolites do not show higher naphtha selectivity than the parent H-USY-0 material at iso-conversion. Moreover, the coke yield produced by H-USY-1 and H-USY-2 samples seems similar or slightly higher than for H-USY-0, depending of the conversion.

Martinez et al. [17] compared stabilized hierarchical USY zeolite with conventional commercial USY for the catalytic cracking of VGO. Higher diesel and lower gas selectivity were attributed to shorter diffusion pathway in the microporous domains induced by the secondary mesoporosity. Garcia et al. [18] have found that for the catalytic cracking of bio-oils with desilicated mesoporous Y zeolites, the higher the mesoporosity, the higher the coke yields.

Effect of the mesoporosity is often used to explain the differences in product selectivity. However, a modification of the porous structure of a zeolite is frequently accompanied by a modification of the acidity. As seen in Chapter III, Part 1, the H-USY-0, H-USY-1, H-USY-2 and H-Y zeolites are differentiated by their porosity and their amount of Brønsted and Lewis acid sites. The hierarchical H-USY-1 and H-USY-2 zeolites were synthesized from the parent H-USY-0 zeolite by surfactant-templated crystal rearrangement to avoid the loss of silica. As shown by the zeolite characterization this increased the framework Si/Al ratio. Thus, the creation of mesoporosity also involves a change in the nature and location of the acid sites. Note that the parent H-USY-0 zeolite has been stabilized by steam treatment and thus already contained mesopores. On the other hand, the H-Y zeolite is fully microporous and very distinct from the three others. Although the porosity parameter and the acidity are correlated, we will try here to evaluate the effect of each parameter on the catalyst performance. An investigation of the correlations between the quantity of each type of acid sites and the porosity of the zeolites follows.

First, we will look at the correlation between the porosity and the different acid sites. In figure 8, the graphs are representing the number of acid sites as a function of the mesoporous volume. An increase of the mesoporous volume is accompanied by a decrease of the number of Brønsted acid sites (Figure 8a). Because of the high Lewis acid sites concentration of H-Y material, an absence of correlation between this number of acid site and the mesoporous volume can be observed (Figure 8b). However, a literature overview conducted by Mitchell et al. [19], on the amount of Brønsted and Lewis acid sites as a function of the mesoporous or external surface area, exhibits a reduced amount



of Brønsted acid sites and an increased amount of Lewis acid sites when increasing mesoporous surface area. They specified that these tendencies were not limited to a single preparative strategy, zeolite framework type or composition.

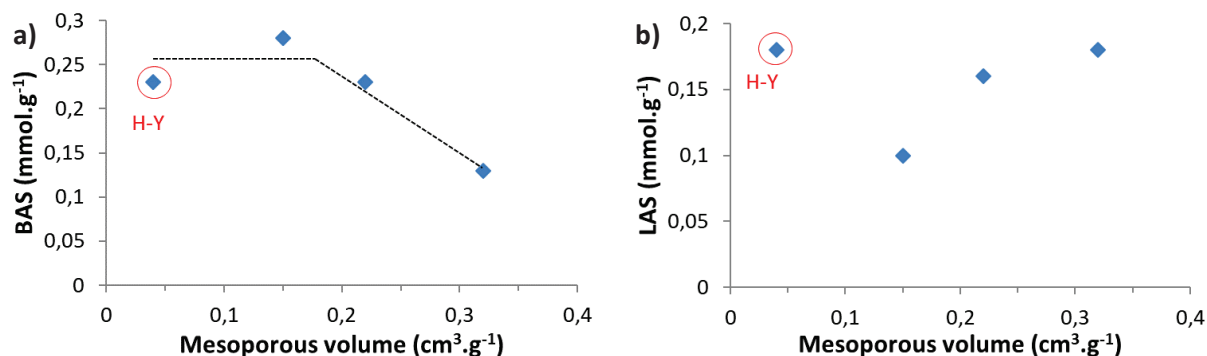


**Figure 8.** Evolution of the number of (a) Brønsted and (b) Lewis acid sites as a function of the mesoporous volume of the zeolites. Data are obtained from H-USY-0, H-USY-1, H-USY-2 and H-Y samples. Dot lines are visual representations of the trends.

Acidity and porosity of the zeolites are often linked parameters, which makes it difficult to attribute any effect to one or the other. Improved catalytic conversion and selectivity for hierarchical catalysts and mesoporous Y zeolites have frequently been reported [17], [18], [20], [21]. However, decoupling the acidity and the porosity effects is not often investigated. Milina et al. [22] have decoupled the porosity and composition effects of ZSM-5 zeolite for the alkylation of toluene, but a similar study for the catalytic cracking has not been found. In order to attribute enhanced performances to a modification of the catalyst porosity or/and acidity, correlations between these parameters and the results from VGO/PDO co-processing in MAT unit are sought after.

Firstly, we start by examining the catalyst activity as a function of the porosity. Mesoporosity has been introduced in the zeolites to enhance the transport of large molecules inside the zeolite. To compare the activity of the four samples the conversion has been normalized with respect to the number of acid sites (BAS). The increase of the mesoporous volume is clearly accompanied by an increase of the catalyst activity (Figure 9a). This tendency suggests that the activity of catalysts having too low mesoporous volume is limited by diffusion limitation. However, as it has been seen in Figure 8a, an increase of the mesoporous volume is also accompanied by a decrease of the number of Brønsted acid sites. This means that the conversion obtained with a catalyst might not be improved with the increase of the mesoporous volume. In fact, the conversion starts decreasing

above a certain amount of mesopore. Figure 9b suggests an optimum conversion for catalyst having a mesoporous volume around  $0.2 \text{ cm}^3 \cdot \text{g}^{-1}$ .

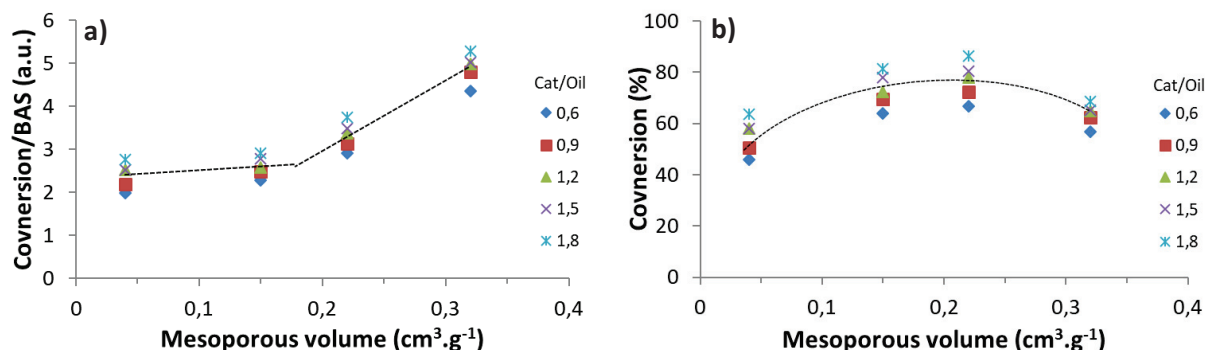


**Figure 9.** (a) Conversion per number of Brønsted acid site and (b) conversion as a function of the mesoporous volume of the catalyst. Conversions are obtained from the co-processing of 90% VGO and 10% PDO in MAT unit. Dot lines are visual representations of the trends.

Regarding the product selectivity, Figure 5 shows that the selectivity of a large range of cracking products is not affected by the catalyst changes. However, differences in coke yield and olefin-to-paraffin ratio are observed. For this reason, coke yield and olefin-to-paraffin ratio as a function of the porosity and acidity of the catalyst are displayed in Figure 10. No influence of the acidity is observed on the coke yield. Nevertheless, a correlation between the coke yield and the mesoporous volume seems to be observed (Figure 10a). First, the increase of the mesoporous volume allows a decrease of the coke yield. Then, a steady coke yield is reached. This exhibits the existence of a volume of mesopores above which the coke formation does not decrease.

A decrease of the O/P ratio is expected with an increasing number of active sites due to the closer proximity between the acid sites that allow a better hydrogen transfer (reaction order of 2) [23]. Apparently, the presence of the micropores decreases the distance of the acid sites even further thus reducing the O/P ratio for the same number of acid sites (Figure 10d). A correlation with the mesoporous volume is also observed in Figure 10b. An increase of the mesoporous volume boosts the proportion of olefins (Figure 2d). It agrees with the fact that increasing of the distance between the acid sites decreases the hydrogen transfer.



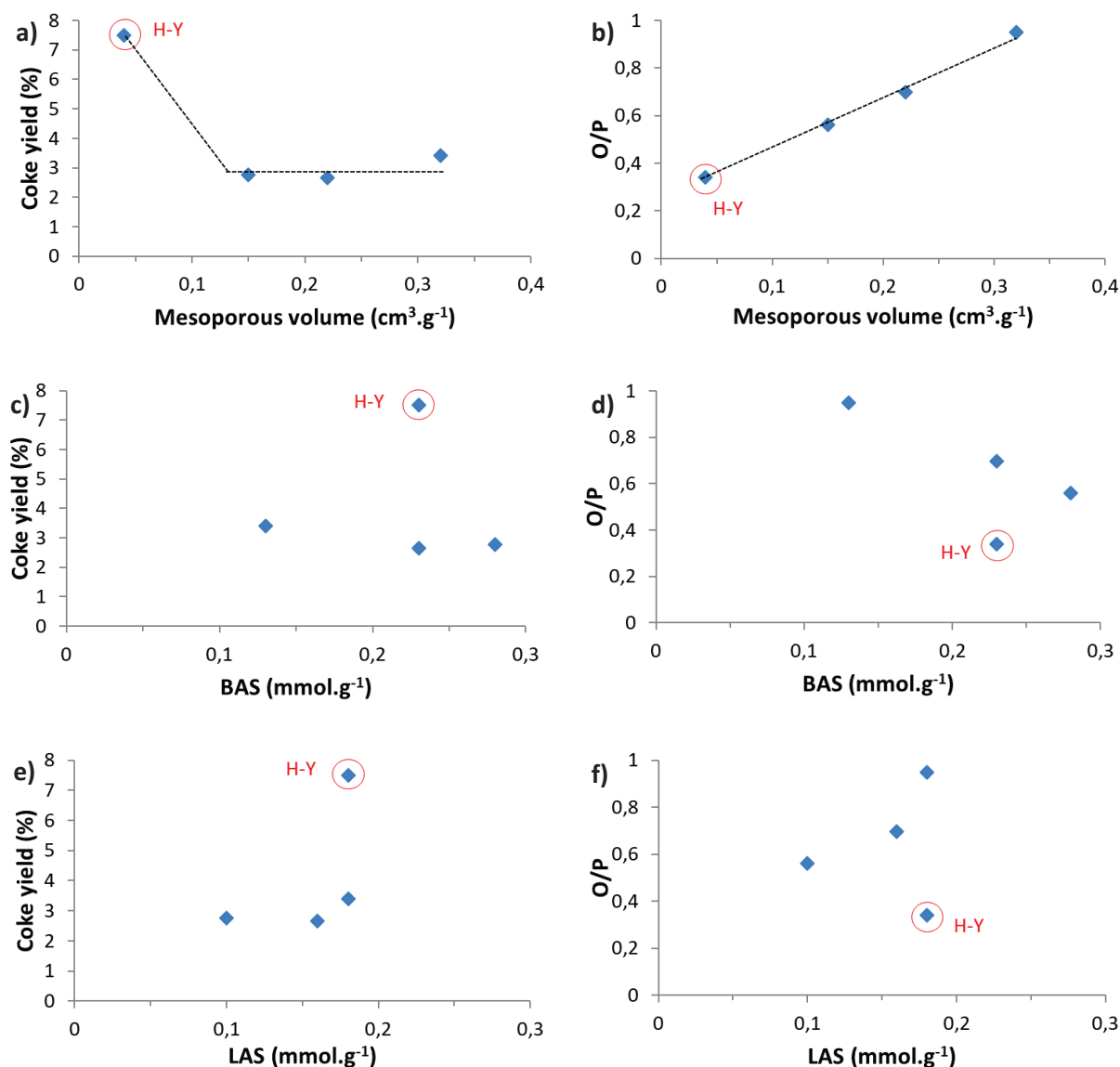


**Figure 10.** Coke yield and olefin-to-paraffin (O/P) ratio, obtained from the co-processing of 90% VGO and 10% PDO in MAT unit, as a function of the mesoporous volume (a and b), number of Brønsted acid sites (c and d) and number of Lewis acid sites (e and f) of the catalyst. Data are obtained at 60% conversion on H-USY-0, H-USY-1, H-USY-2 and H-Y catalysts. Dot lines are visual representations of the trends.

## 5. Conclusion

Hierarchical zeolites are known to improve catalytic activity of reactions taking place under diffusion limitation. For the co-processing of VGO and bio-oil presented in this chapter, the addition of mesopores increased the activity of the catalyst. However, the conversion of the hierarchical H-USY-1 zeolite is similar to the conversion of the non-organized mesoporous H-USY-0 sample. The conversion of the highly modified H-USY-2 sample was lower than other mesoporous samples, but higher than

the microporous H-Y zeolite. This is due to a modification of the acid site concentration during the sample preparation.

Variations in the cracking reaction network, occurring in the various catalysts, can be observed due to differences of olefinicity within the C<sub>2</sub>-C<sub>4</sub> gas range. The lower density of acid sites for catalysts containing high mesoporous volume and low amount of acid sites seems to decrease the hydrogen transfer. Other specificities within the three USY samples, exhibiting a combination of micro- and mesopores, are very difficult to distinguish due to similar product selectivity at iso-conversion.

The research of correlations between the pore volume, the amount of acid sites, the catalyst activity, the coke yield and the olefin-to-paraffin ratio showed the benefit of increasing the mesoporous volume for improving conversion of feedstock containing large molecules. The research also suggests the existence of an optimum value of the mesoporous volume, for which the coke production do not decrease anymore, and the conversion of the feedstock is optimal.

### Highlights

- Pure vacuum gas oil and vacuum gas oil/partially deoxygenated oil mixture were used as feedstock for micro activity test.
- The addition of 10% of PDO did not have a significant effect on the conversion or product selectivity.
- The activity of hierarchical H-USY-1 and H-USY-2 samples increased by comparison with mesoporous H-USY-0. However, due to a loss of acid sites in H-USY-2 sample, its conversion was not improved.
- The conversion with the microporous H-Y zeolite was lower than with other samples.
- Hierarchical USY did not decrease coke formation by comparison to the parent USY sample.
- The density of acid sites affected the olefin-to-paraffin ratio.

## References for Chapter V

- [1] A. D. R. Pinho, M. B. B. De Almeida, F. L. Mendes, V. L. Ximenes, and L. C. Casavechia, “Co-processing raw bio-oil and gasoil in an FCC Unit,” *Fuel Process. Technol.*, 2015, doi: 10.1016/j.fuproc.2014.11.008.
- [2] G. Fogassy, N. Thegarid, Y. Schuurman, and C. Mirodatos, “From biomass to bio-gasoline by FCC co-processing: Effect of feed composition and catalyst structure on product quality,” *Energy Environ. Sci.*, vol. 4, no. 12, pp. 5068–5076, 2011, doi: 10.1039/c1ee02012a.
- [3] D. Verboekend, “New Hierarchical Zeolite Catalysts by Post-Synthetic Design,” no. 20730, p. 221, 2012, doi: 10.3929/ethz-a-007595445.
- [4] E. T. C. Vogt and B. M. Weckhuysen, “Fluid catalytic cracking: recent developments on the grand old lady of zeolite catalysis,” *Chem. Soc. Rev. Chem. Soc. Rev.*, vol. 7342, no. 44, pp. 7342–7370, 2015, doi: 10.1039/c5cs00376h.
- [5] W. Schwieger *et al.*, “Hierarchy concepts: classification and preparation strategies for zeolite containing materials with hierarchical porosity,” *Chem. Soc. Rev.*, vol. 45, no. 12, pp. 3305–3566, 2016, doi: 10.1039/C5CS00599J.
- [6] D. H. Park *et al.*, “Selective petroleum refining over a zeolite catalyst with small intracrystal mesopores,” *Angew. Chemie - Int. Ed.*, vol. 48, no. 41, pp. 7645–7648, 2009, doi: 10.1002/anie.200901551.
- [7] S. Stefanidis *et al.*, “Mesopore-modified mordenites as catalysts for catalytic pyrolysis of biomass and cracking of vacuum gasoil processes,” *Green Chem*, vol. 15, 2013, doi: 10.1039/c3gc40161h.
- [8] J. Garcia-Martinez, M. Johnson, J. Valla, K. Li, and J. Y. Ying, “Mesostructured zeolite Y—high hydrothermal stability and superior FCC catalytic performance,” *Catal. Sci. Technol. Catal. Sci. Technol*, vol. 2, no. 2, pp. 987–994, 2012, doi: 10.1039/c2cy00309k.
- [9] C. Achten and J. T. Andersson, “Overview of Polycyclic Aromatic Compounds (PAC),” *Polycycl. Aromat. Compd.*, vol. 35, no. 2–4, pp. 177–186, 2015, doi: 10.1080/10406638.2014.994071.
- [10] L. Gueudré *et al.*, “Optimizing the bio-gasoline quantity and quality in fluid catalytic cracking co-refining,” 2017, doi: 10.1016/j.fuel.2016.12.021.
- [11] M. Guisnet and P. Magnoux, “Organic chemistry of coke formation,” vol. 212, pp. 83–96, 2001.

- [12] J. Abbot and F. N. Guerzoni, "Roles of Brønsted and Lewis sites during cracking of n-octane on H-mordenite," *Appl. Catal. A, Gen.*, vol. 85, no. 2, pp. 173–188, 1992, doi: 10.1016/0926-860X(92)80150-B.
- [13] K. Rajagopalan and A. W. Peters, "Effect of exchange cations and silica to alumina ratio of faujasite on coke selectivity during fluid catalytic cracking," *J. Catal.*, vol. 106, no. 2, pp. 410–416, 1987, doi: 10.1016/0021-9517(87)90253-3.
- [14] G. Fogassy, N. Thegarid, Y. Schuurman, and C. Mirodatos, "From biomass to bio-gasoline by FCC co-processing: effect of feed composition and catalyst structure on product quality," *Energy Environ. Sci.*, vol. 4, no. 12, pp. 5068–5076, 2011, doi: 10.1039/c1ee02012a.
- [15] T. P. Fonseca, J. Fernandes, and C. I. C. Pinheiro, "Modeling the kinetics of light cuts catalytic cracking Development of a predictive tool."
- [16] L. Gueudré, "Internal report CNRS."
- [17] C. Martínez, D. Verboekend, J. Pérez-Ramírez, and A. Corma, "Stabilized hierarchical USY zeolite catalysts for simultaneous increase in diesel and LPG olefinicity during catalytic cracking," *Catal. Sci. Technol.*, vol. 3, no. 4, p. 972, 2013, doi: 10.1039/c2cy20688a.
- [18] J. R. García, M. Bertero, M. Falco, and U. Sedran, "Catalytic cracking of bio-oils improved by the formation of mesopores by means of  $\gamma$  zeolite desilication," *Appl. Catal. A Gen.*, 2015, doi: 10.1016/j.apcata.2014.11.005.
- [19] S. Mitchell *et al.*, "Aluminum Redistribution during the Preparation of Hierarchical Zeolites by Desilication," *Chem. - A Eur. J.*, vol. 21, no. 40, pp. 14156–14164, 2015, doi: 10.1002/chem.201500992.
- [20] W. Li, J. Zheng, Y. Luo, and Z. Da, "Effect of hierarchical porosity and phosphorus modification on the catalytic properties of zeolite Y," *Appl. Surf. Sci.*, vol. 382, pp. 302–308, 2016, doi: 10.1016/j.apsusc.2016.04.146.
- [21] J. R. García, M. Falco, and U. Sedran, "Intracrystalline mesoporosity over Y zeolites. Processing of VGO and resid-VGO mixtures in FCC," *Catal. Today*, vol. 296, no. December 2016, pp. 247–253, 2017, doi: 10.1016/j.cattod.2017.04.010.
- [22] M. Milina, S. Mitchell, Z. D. Trinidad, D. Verboekend, and J. Pérez-Ramírez, "Decoupling porosity and compositional effects on desilicated ZSM-5 zeolites for optimal alkylation performance," *Catal. Sci. Technol.*, vol. 2, no. 4, pp. 759–766, 2012, doi: 10.1039/c2cy00456a.

- [23] W. Vermeiren and J. P. Gilson, “Impact of zeolites on the petroleum and petrochemical industry,” *Top. Catal.*, vol. 52, no. 9, pp. 1131–1161, 2009, doi: 10.1007/s11244-009-9271-8.

# Conclusion and Perspectives

---

This PhD research presents the preparation, characterization and testing of hierarchical materials in the frame of promoting the bio-sourced feedstock processing within conventional refinery. This new feedstock contains large oxygenated molecules derived from lignocellulosic biomass. These molecules have been reported to increase the coke formation. Great expectations have been put on hierarchical catalysts because of their ability to enhance mass transport, which is one of the limitations for the processing of large molecules.

Four zeolites have been studied along this work. One purely microporous H-Y zeolite, corresponding to the CBV400 from Zeolyst. One ultra-stable Y zeolite, named H-USY-0, having some mesopores due to the steaming treatment performed by Zeolyst for its stabilization. From this H-USY-0 zeolite, two other samples named H-USY-1 and H-USY-2 have been prepared by surfactant-templated crystal rearrangement. The preparation of these two zeolites created a well-organized mesoporous network. Hence, H-USY-2 had a higher mesoporous volume than H-USY-1. In its turn, H-USY-1 has a higher mesoporous volume than H-USY-0. During this treatment, the bulk Si/Al ratio of the materials stayed constant, but part of the alumina atoms was removed from the framework. This contributed to a change of acidity in the hierarchical zeolite samples: Bronsted acid sites were lost and Lewis acid sites were formed, as confirmed by the IR study of pyridine adsorption. Note that H-Y sample did not show higher acidity than USY samples due to residual sodium.

The mass transport improvement within H-USY-1 and H-USY-2 samples has been observed in the research of the mesitylene diffusion. An increase of around 50% between the diffusion coefficients of the hierarchical H-USY-1 and H-USY-2 samples and H-USY-0 was measured. The diffusion measurement in H-Y sample presented some issues, preventing accurate diffusion coefficient calculations.

The catalytic cracking of n-hexane, used as a model reaction, confirmed the loss of active sites for H-USY-2, which had been previously observed by the IR study of pyridine adsorption. The conversions with H-USY-0 and H-USY-1 zeolites were higher than H-USY-2 zeolite. The high turnover frequencies of the USY materials, compared to the H-Y sample, confirmed the beneficial effect of mesopores for improving catalyst activity.

Then, the four samples were used for the co-processing of a mixture made from 90% crude oil and 10% partially deoxygenated bio-oil. The hierarchical H-USY-1 and H-USY-2 zeolites, containing high mesoporous volume, exhibit higher catalytic activities than H-USY-0 and H-Y materials. This

difference emphasises the diffusional limitation that the co-processing of VGO and PDO entails. However, for the same mass of catalyst, the highest conversions were obtained with H-USY-0 and H-USY-1 samples. The loss of acid sites of H-USY-2 sample led to lower conversions than H-USY-0 and H-USY-1. Moreover, the formation of coke stopped decreasing when the mesoporous volume of the catalysts reaches a certain point. Through these observations, the presence of mesopores within the catalyst used for the cracking of large molecules seems essential. Nevertheless, a moderate amount of mesopores appears to be enough to reach improved mass transfer, high catalytic conversion and low coke formation during catalytic cracking of bulky components.

The tests presented here were performed with pure zeolite. These catalysts differ from the real FCC catalysts, where a matrix and rare earth elements are also involved in the diffusion, activity and stability of the catalyst. Further review considering the preparation of catalysts including the embedding of the zeolites within a matrix and the presence of rare earth could be of interest. The testing of a larger range of materials, in particular hierarchical zeolites with different mesopore diameters and materials without extra framework aluminium, would be interesting for deeper analysis. Since the differences between the processing of pure VGO and the co-processing of 90% VGO and 10% bio-oil did not differ in a significant way, it would be interesting to increase the proportion of bio-sourced oil within the inlet feedstock. Finally, a characterisation of the coke deposit induced by the catalytic cracking reactions would be an additional asset for a better understanding of the hierarchical materials in FCC process.

## Appendix I

---

### Appendix I – Determination of the apparent surface area

Brunauer, Emmett and Teller reported a multilayer adsorption theory, based on the following hypotheses:

- All adsorption sites on bare solid surface have same adsorption energy ( $E_1$ ).
- There is no lateral interaction between adsorbed molecules
- The adsorption energies in the second and all higher layers ( $E_2, \dots, E_i$ ) are equal to condensation energy of adsorptive ( $E_L$ ).

Considering a model where the adsorption sites remain constant at adsorption equilibrium, the following equation, called BET plot equation, has been found:

$$\frac{p}{V_a(p_0 - p)} = \frac{1}{V_m c} + \frac{c - 1}{V_m c} \left( \frac{p}{p_0} \right)$$

Where:  $V_a$  is the total gas volume adsorbed at standard state ( $T=273.15$  K and  $P=101.3$  kPa)

$V_m$  is the gas volume at the monolayer coverage

$c$  is a positive constant

$p$  is the absolute pressure

$p_0$  is the saturation pressure of the adsorptive at measurement temperature

From this equation, it is evident that the plot ( $p/V_a(p_0-p)$ ) as a function of ( $p/p_0$ ) should give a straight line, and that the intercept and slope are ( $1/V_m c$ ) and  $(c-1)/V_m c$ , respectively.

For example, the BET plot of the H-USY-0 sample is displayed in Figure 1. In this case, the straight line obtained at low relative pressure lead to a gas volume at monolayer coverage of  $199.6 \text{ cm}^3(\text{STP}).\text{g}^{-1}$ .

The specific surface area ( $a_s$ ) of the sample is calculated according to the equation:

$$a_s = \frac{V_m}{22414} \times L \times \sigma$$

Where:  $L$  is the Avogadro constant, which is  $6.022\text{E}+23 \text{ mol}^{-1}$

$\sigma$  is the cross-sectional area of the nitrogen, which is  $0.162 \text{ nm}^2$ .

In the present example, the corresponding specific surface area is  $869 \text{ m}^2.\text{g}^{-1}$ .



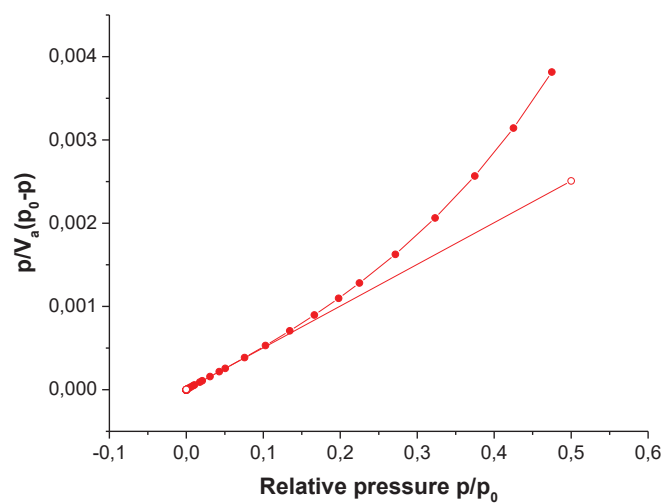


**Figure 1.** BET plot of from N<sub>2</sub> adsorption-desorption isotherm of H-USY-0 sample and the linear line obtained from relative pressure below 0.10.

## Appendix II

### Appendix II – Determination of the microporous volume

The microporous volume is determined from the plot of adsorbed nitrogen volume versus the relative pressure. When the slope of the adsorption branch becomes lower than  $1000 \text{ cm}^3 \cdot \text{g}^{-1}$ , all micropores are considered to be filled.

Taking as example the H-USY-0 sample, the Table 1 displays the relative pressure  $p/p_0$ , the gas volume adsorbed at pressure  $p$  and the slope of the adsorption plot. The slope of each  $V_{\text{ads}}$  value, in the line  $i$  of the Table 1, is calculated as:

$$\text{Slope } [i] = \frac{V_{\text{ads}}[i + 1] - V_{\text{ads}}[i - 1]}{\frac{p}{p_0}[i + 1] - \frac{p}{p_0}[i - 1]}$$

**Table 1.** Volume of gaseous nitrogen adsorbed during the adsorption of  $\text{N}_2$  at 77K on H-USY-0, at different relative pressure  $p/p_0$  and the corresponding slope of the adsorption plot.

$p/p_0$	$V_{\text{ads}} [\text{cm}^3 \cdot \text{g}^{-1}]$	Slope
0,002	167,22	8809,2
0,00297	174,18	5242,4
0,00461	180,91	3505,4
0,00582	184,16	2263,6
0,00756	187,58	1665,2
0,0099	190,96	1095,0
<b>0,01581</b>	<b>196,62</b>	<b>782,0</b>
0,02161	200,12	494,8
0,03105	204,16	360,2
0,04291	207,79	269,7
0,05537	210,72	215,2
0,06754	213,09	173,8

In the present case, the slope of the adsorption branch becomes lower than  $1000 \text{ cm}^3 \cdot \text{g}^{-1}$  when  $V_{\text{ads}}=196.62 \text{ cm}^3 \cdot \text{g}^{-1}$ . According to equation 6 and 7 of Chapter II, the microporous volume of this sample is:

$$V_{\text{micropores}} = 196.62 \times \frac{28}{22414 \times 0.808} = 0.30$$

According to this example, the microporous volume of H-USY-0 is  $0.30 \text{ cm}^3 \cdot \text{g}^{-1}$ .

## Appendix III

---

### Appendix III – HR-TEM image of H-USY-2

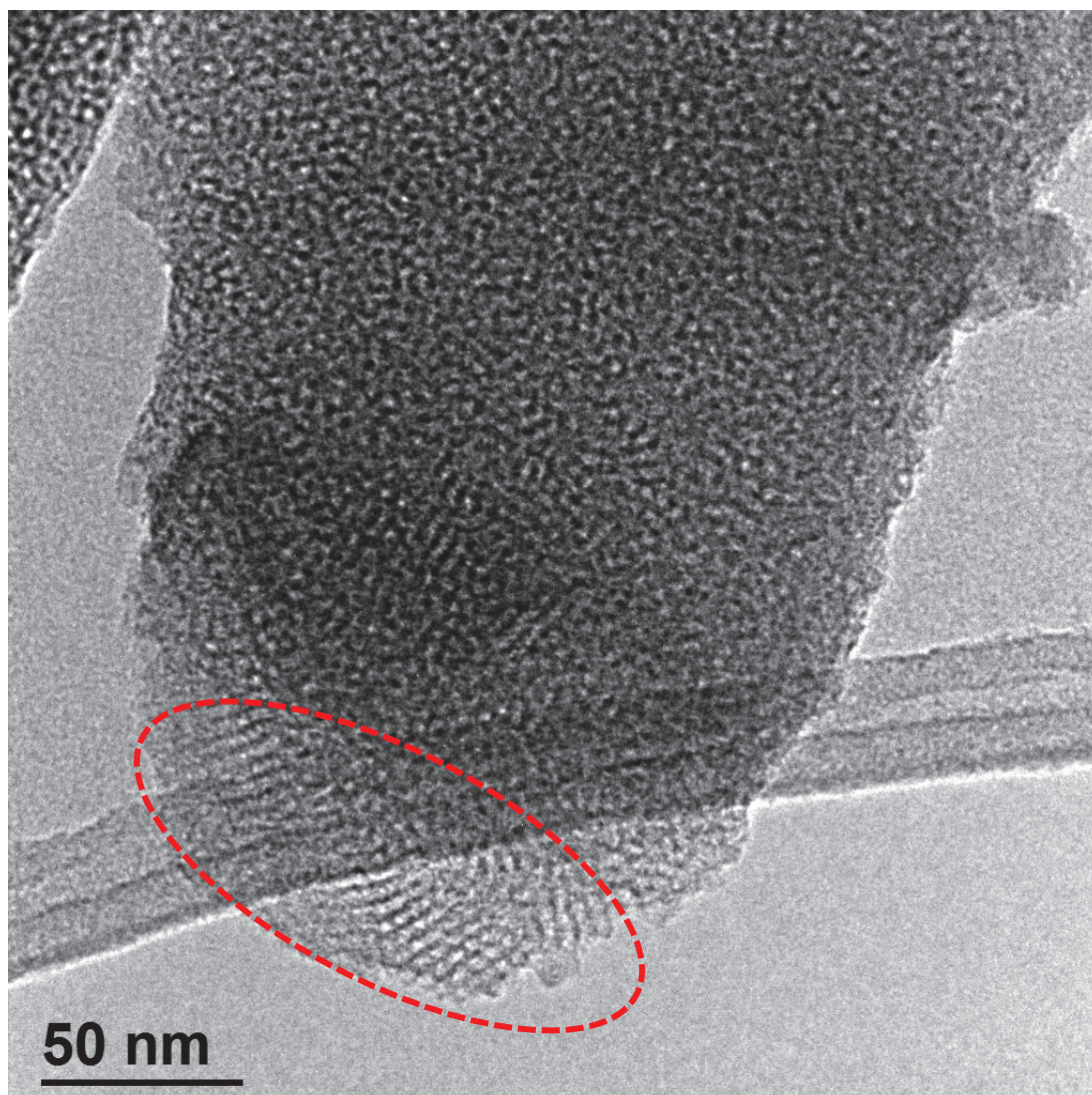


**Figure 2.** Identification of the well-organized mesoporous network of H-USY-2 sample.

## Appendix IV

### Appendix IV – Small angle of spend catalyst after cracking of n-hexane and 2-butanol

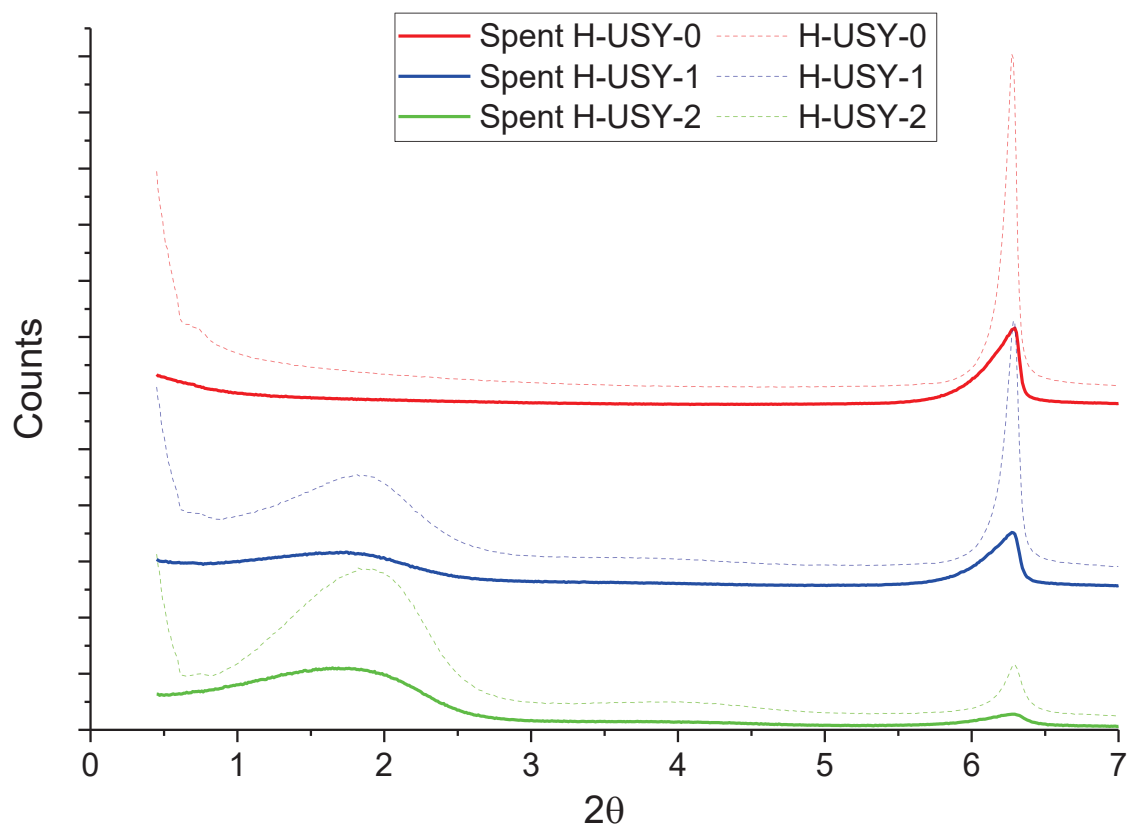


**Figure 3.** Small angles XRD spectrum for the spent (straight lines) and fresh samples (dotted lines). Spent materials are obtained after catalytic cracking of n-hexane and 2-butanol, followed by the regeneration step under an air flow.



## Appendix V

### Appendix V – SEM images of the USY materials

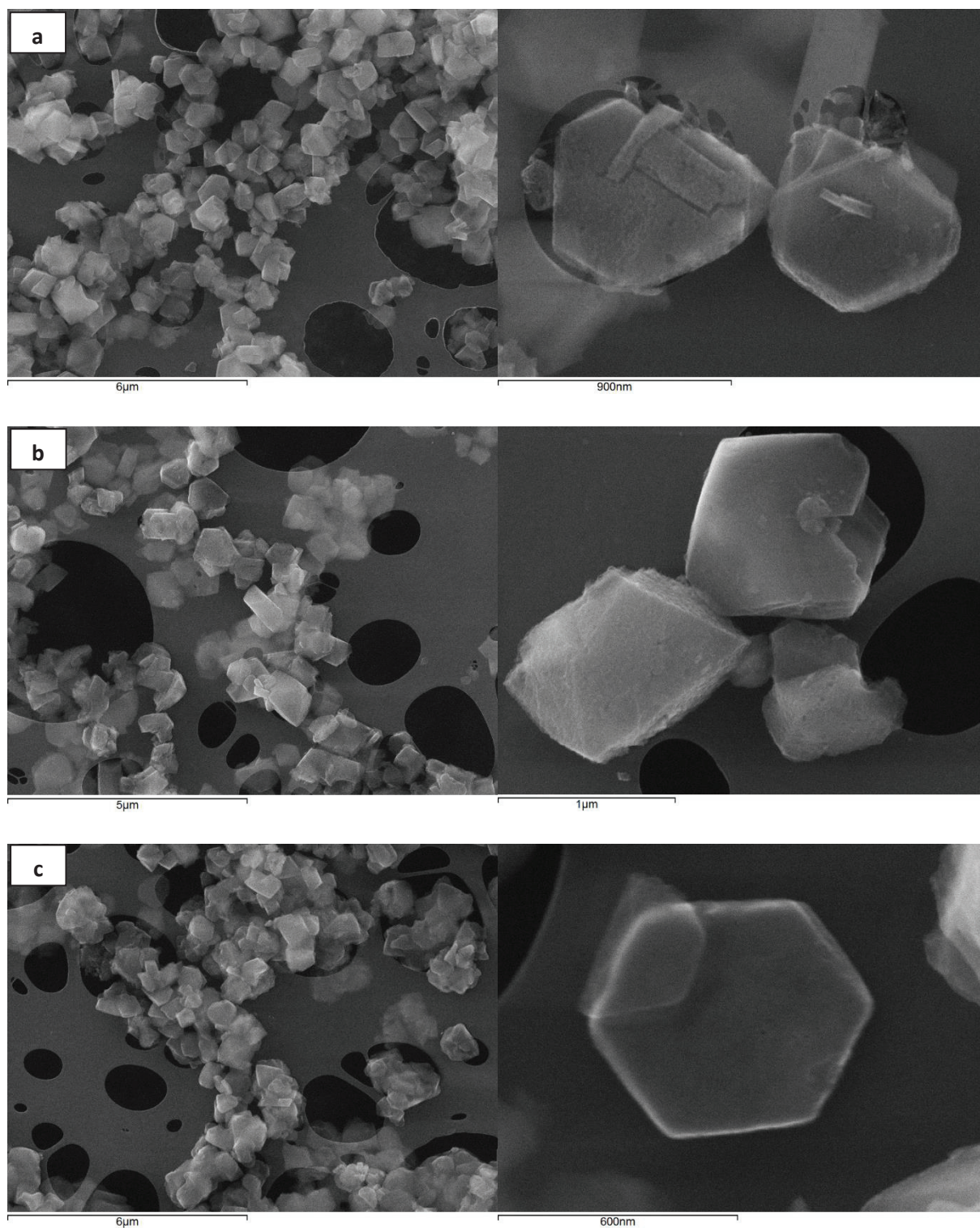


**Figure 4.** SEM pictures of (a) H-USY-0, (b) H-USY-1 and (c) H-USY-2.

## Appendix VI

---

### Appendix VI – Estimation of the diffusion coefficient in MAT unit

- Estimation of the diffusion coefficient

In order to compare the mass transport in MAT unit with the ZLC experiment performed with mesitylene, an attempt of calculation has been explored. Considering the cracking reaction as a first order reaction where  $A \rightarrow \text{Products}$ , the reaction rate  $r_A$  is:

$$r_A = k \times C_A = k \times C_A^0 (1 - x_A) \quad (32)$$

Where:  $k$  is the reaction constant, in  $\text{m}^3 \cdot \text{kg}^{-1} \cdot \text{s}^{-1}$

$C_A$  is the concentration of reactant, in  $\text{mol} \cdot \text{m}^{-3}$

$C_A^0$  is the initial concentration of reactant, in  $\text{mol} \cdot \text{m}^{-3}$

$x_A$  is the conversion rate of reactant A.

Considering that the reaction takes place in a batch reactor during the MAT tests, the reaction rate  $r_A$  follows the equation:

$$r_A = -\frac{1}{W} \times \frac{dn_A}{dt} = -\frac{V}{W} \times \frac{dC_A}{dt} \quad (33)$$

Where:  $W$  is the weight of catalyst, in kg.

$n_A$  is the amount of reactant injected inside the reactor, in mol.

$V$  is the volume of the reactor, in  $\text{m}^3$ .

By coupling the equation (32) and (33), one finds:

$$\begin{aligned} \frac{dC_A}{C_A} &= -\frac{W}{V} \times k \times dt \\ \ln C_A - \ln C_A^0 &= \ln(1 - x_A) = -\frac{W}{V} \times k \times t_{Batch} \end{aligned} \quad (34)$$

Where:  $t_{Batch}$  is the residence time of the reactant inside the reactor, in s. As a first approximation, this residence time is considered the same as the MAT injection time.

To characterize the diffusion limitations within porous materials, Thiele and Zeldovich defined an effectiveness factor  $\eta$  [10]:

$$\eta = \frac{\text{Rate of reaction with pore diffusion resistance}}{\text{Rate of reaction with surface conditions}} \quad (35)$$

Thus, at equivalent Cat/Oil ratio, the conversion for the hierarchical and microporous zeolites can be defined as:

$$x_{A,Meso} = 1 - e^{-kt} \quad (36)$$

$$x_{A,Micro} = 1 - e^{-kt\eta} \quad (37)$$

And

$$\eta = \frac{[\ln(1 - x_A)]_{Micro}}{[\ln(1 - x_A)]_{Meso}} \quad (38)$$

Looking for example at the catalytic cracking of the blending VGO/PDO performed in MAT unit (Chapter V, Part 3), the conversions  $x_A$  associated to a Cat/Oil ratio of 0.6 are equal to 0.46 and 0.64 for H-Y and H-USY-0 respectively. At these conversions, the naphtha concentration is still increasing with the conversion, indicating that the first cracking reaction is still predominant on secondary reactions.

Thus, the effectiveness factor is:

$$\eta = \frac{\ln(1 - 0.46)}{\ln(1 - 0.64)} = 0.60$$

Considering the catalyst particles as spheres, the effectiveness factor follows the equation [11]:

$$\eta = \frac{3}{\phi} \times \frac{\phi \coth \phi - 1}{\phi} \quad (39)$$

With:

$$\phi = R \sqrt{\frac{k \times \rho}{D_{Feedstock}}} \quad (40)$$

Where:  $\phi$  is the Thiele modulus.

$R$  is the radius of the catalyst particles, in m.

$\rho$  is the catalyst density, in  $\text{kg.m}^{-3}$ .

$D_{Feedstock}$  is the effective diffusivity of the feedstock, in  $\text{m}^2.\text{s}^{-1}$ .

According to the plot  $\eta=f(\phi)$  corresponding to the equation (39) (Figure 1), the Thiele modulus  $\phi$  corresponding to an effectiveness factor of 0.60 is 3.6.

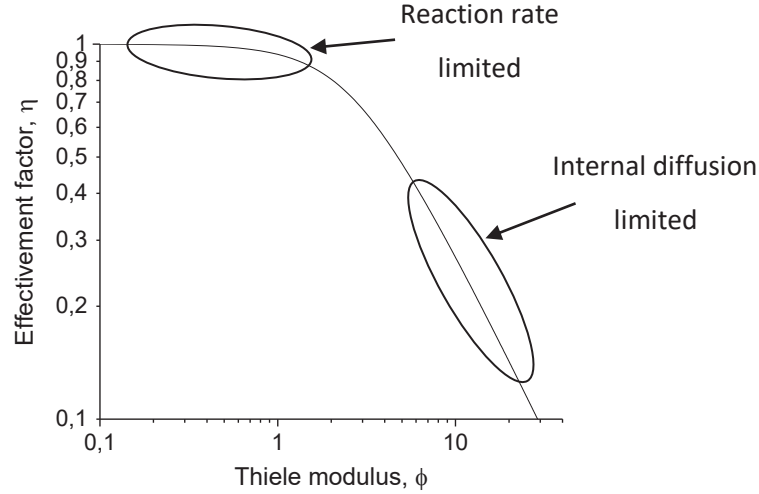


**Figure 5.** Effectiveness factor plot for first order kinetic on spherical catalyst particles.

The effective diffusion of the feedstock processed in MAT unit is obtained by combining equation (34) and (40):

$$D_{Feedstock} = \frac{R^2 \times \left( \frac{-V}{W} \times \frac{[\ln(1 - x_A)]_{meso}}{t_{Batch}} \right) \times \rho_{Cat}}{\phi^2} \quad (41)$$

For the material H-USY-0, the radius of the zeolite particles is found to be 0.3μm according to scanning electron microscopy (Appendix V). The MAT reactor is considered as a cylinder of 1.5cm of diameter and 30cm length, containing 1g of sample. The 30seconds-length of feedstock injection is considered as the residence time  $t_{Batch}$ . The catalyst density is estimated from XDR measurement where the unit cell parameter is found to be 24.35Å. The Fichtner-Schmittler empirical equation (Chap. II Part 1.2) leads to 13.2 aluminium atoms per unit cell. Considering the total number of silica and aluminium atoms is 192 in faujasite zeolite, 178.8 atoms of silica are expected per unit cell. At these 192 atoms are associated 384 atoms of oxygen, whereas the  $Na^+$  and  $H^+$  effect on the total weight of the sample are ignored because of the low sodium concentration and the low molar mass of hydrogen. The catalyst density estimated via these considerations is 1340 kg.m<sup>-3</sup>.

The calculation of the effective diffusion of the MAT feedstock  $D_{Feedstock}$  according to equation 41 leads to  $D_{Feedstock}=1.7E-14 \text{ m}^2.s^{-1}$ .

The accuracy of this value is subject to the residence time, which could be superior to 30s due to specific sequence of steps during MAT experiments.



Similarly, considering conversions of 0.67 and 0.57 for H-USY-1 and H-USY-2 at Cat/Oil=0.6, the effective diffusion  $D_{\text{Feedstock}}$  is equal to  $1.4\text{E-}14 \text{ m}^2.\text{s}^{-1}$  and  $2.9\text{E-}14 \text{ m}^2.\text{s}^{-1}$ , respectively.

- Comparison with the diffusion of mesitylene

For the ZLC experiments carried out with mesitylene, a  $D/R^2$  coefficient of  $0.50\text{E-}04 \text{ s}^{-1}$  was found with Na-USY-0 at  $60^\circ\text{C}$  (Chapter III, Part 3.2.3). Assuming that similar diffusion would be obtained with the proton form of the zeolite, and considering a similar crystal radius of  $0.3\mu\text{m}$ , the effective diffusion  $D_{\text{eff}}$  is found equal to  $4.5\text{E-}18 \text{ m}^2.\text{s}^{-1}$ .

The activation energy for mesitylene in Na-USY-0 catalyst was found equal to  $17 \text{ kJ.mol}^{-1}$ . Hence, the diffusion coefficient of mesitylene at  $560^\circ\text{C}$ , which is the temperature that MAT experiments are carried out, is obtained according to the following equation:

$$D_{\text{eff},T_1} = D_{\text{eff},T_2} \times \exp \left[ \frac{E_a}{R} \left( \frac{T_1 - T_2}{T_1 T_2} \right) \right] \quad (42)$$

Where:  $D_{\text{eff},T_1}$  and  $D_{\text{eff},T_2}$  are the effective diffusion at temperature  $T_1$  and  $T_2$ , respectively.

$R$  is the gas constant, which is taken equal to  $8.314 \text{ J.mol}^{-1}.\text{K}^{-1}$ .

According to equation 42, the effective diffusion of mesitylene  $D_{\text{eff}, 560^\circ\text{C}}$  in Na-USY-0 at  $560^\circ\text{C}$  is equal to  $1.7\text{E-}16 \text{ m}^2.\text{s}^{-1}$ . This value is hundred times lower than the one obtained for the FCC feedstock. Since FCC feedstock is composed of larger molecules than mesitylene, we should have found  $D_{\text{Feedstock}} < D_{\text{eff}, 560^\circ\text{C}}$ . However, both calculations of  $D_{\text{Feedstock}}$  in MAT unit and extrapolation of  $D_{\text{eff}}$  from ZLC are subjected to several assumptions, which may explain the results.